STUDYING AND CONTROLLING ORDER WITHIN NANOPARTICLE MONOLAYERS FABRICATED THROUGH ELECTROPHORETIC DEPOSITION

By

ALEXANDER J. KREJCI

Dissertation under the direction of Professor James H. Dickerson

Submitted to the Faculty of the

Graduate School of Vanderbilt University

in partial fulfillment of the requirements

for the degree of

DOCTOR OF PHILOSOPHY

in

Physics

August, 2013

Nashville, Tennessee

Approved:

James H. Dickerson

Shane Hutson

Janet Macdonald

Norman Tolk

Kalman Varga

Dedicated to

My parents, Kelly and Jerry Krejci, for their unconditional love and unwavering support

My brothers, Jason, Daniel, Taylor, Andrew, and David, for making me tough

My sister, Heather, for keeping me alive

My baby nieces, Rylin, Ashlyn, and Sawyer, for remembering the uncle they rarely see

And to all my friends who have been there for me.

ACKNOWLEDGEMENTS

The biggest thanks goes to my advisor, Professor James Dickerson, for helping me develop as a scientist and as a person and always having interest in my success.

Thanks to my committee members, Normal Tolk, Kalman Varga, Shane Hutson, and especially Janet Macdonald for their guidance and support during the toughest of times.

Thanks to my group members: Isabel Gonzalo Juan, without whom working in the lab and life in Nashville would have not been nearly as fun nor would I have learned nearly as much. Thanks also to Suseela Somarajan, Saad Hasan, Sameer Mahajan, Weidong He, John Rigueur, Howard Titzel, and Max Osmulski. And especially thanks to my mentees, Jyotirmoy Mandal and Colin Thomas, who trusted my guidance in the lab and also helped me to improve my work and quality of life.

Thanks to all of the Vanderbilt Institute of Nanoscale Science and Engineering staff, specifically Tony Hmelo, Dmitry Koktysh, and Ben Schmidt for teaching me how to use so many scientific tools and fixing those tools when I broke them. Thanks to James McBride for help with TEM imaging.

Thanks to the Kirill Bolotin group: AKM Newaz, Dhiraj Prasai, and very much to Hiram Conley for always being willing to discuss any problems I may have had.

Thanks to Susan Sutton of Tennessee State University for help with AFM measurements.

Thanks to Jonathan Jarvis for giving me impromptu LabVIEW lessons.

Thanks to Ju-Hyun Park and Ryan Stillwell of the National High Magnetic Field Lab for help acquiring magnetic measurements.

Thanks to Adriana Mendoza-Garcia and Shouheng Sun for sending cobalt ferrite nanoparticles that were essential to improving my dissertation and as well as for promptly answering any questions and sending any data I requested.

Thanks to Tetsuo Uchikoshi of the National Institute of Materials Science (NIMS) in Tsukuba, Japan, for allowing me to visit the institute and work in his laboratory. Without this, my dissertation would have struggled to progress. And thanks to Mrinalini Mishra and Chika Matsunaga for their assistance during my visit.

Thanks to the staff at the Center for Functional Nanomaterials at Brookhaven National Lab. Special thanks goes to Chris Ruggiero for excitement, hard work, and good ideas that went into building the EPD cell used that was essential in many of the experiments. And another special thanks to Kevin Yager for taking an interest in my research and in my career and helping to acquire x-ray scattering data that is essential to my dissertation. Additionally, thanks to Fernando Camino, Aaron Stein, Ming Lu, and Dmytro Nykypanchuk for their useful trainings and assistance solving technical challenges during this work.

Finally, thanks to Elizabeth Goiri Little for her detailed editing of this dissertation.

TABLE OF CONTENTS

LIST OF FIGURES

LIST OF TABLES

ABBREVIATIONS

NP – nanoparticle
PL – photoluminescent
NPM – nanoparticle monolayer
EPD - electrophoretic deposition
TOPO – trioctylphosphine oxide
AOT – dioctyl sodium sulfosuccinate
TEM – transmission electron microscopy
XRD – x-ray diffraction
VSM – vibrating sample magnetometry
CCD – charge-coupled device
VINSE – Vanderbilt Institute of Nanoscale Science and Engineering
CFN – Center for Functional Nanomaterials
FWHM – full width at half maximum
Vis – visible
NIR – near infrared
FC – field cooled
ZFC – zero field cooled
DLS – dynamic light scattering
LDV – laser Doppler velocimetry
SEM – scanning electron microscopy
AFM – atomic force microscopy
GISAXS – grazing-incidence, small-angle x-ray scattering
GIWAXS – grazing-incidence, wide-angle x-ray scattering
NSLS – National Synchrotron Light Source
vdWI – van der Waals interactions
IP – in plane
OP – out of plane
MFM – magnetic force microscopy

CHAPTER I

INTRODUCTION

Nanoscience is often defined as the study of materials with at least one dimension from 1 to 100 nanometers. More importantly, however, nanoscience studies materials on the size scale at which quantum mechanical effects can be tuned by varying the characteristics of a nanoparticle (NP), such as size, shape, chemistry, and more. These quantum effects give rise to a wide range of unique properties that make nanomaterials suitable for many applications, some of which are not possible without nanoscale science. With these new properties, nanomaterials offer potential solutions in a wide variety of fields from medicines and biomaterials to electronics and energy production [1-3].

Just as ensembles of ordered atoms (a crystal) exhibit collective properties which give rise to phenomena that do not exist for a single atom, the same is true of NP ensembles; ordered arrays of NPs (supercrystals) exhibit properties that are not observed in individual NPs. These collective properties open the door for even more applications for nanomaterials [4]. A few examples that demonstrate this fact will be discussed.

In the first example, photoluminescent (PL) optical properties of three CdSe NP systems were studied: one ordered array of NPs, one unordered array, and one system of isolated NPs. In these three systems, the ordered array showed a significantly sharper PL peak compared to the unordered array and the individual NPs [5]. In a second example, the electrical properties for three systems of Ag NPs were studied: one hexagonally packed 2D array of Ag NPs, one cubically packed 2D array, and one individual NP. I-V

curves of each system were measured and produced dramatically different behaviors simply due to the change in arrangement of NPs [6]. In a final example, arrays of Ag NPs were created and then sintered. By sintering ordered arrays, it was possible to create large monocrystals of silver; monocrystals could not be created using unordered arrays [7]. These are just three examples that elucidate the control over a wide range of properties that can be achieved by tuning the order within NP ensembles.

Given the potential of films composed of ordered NP arrays, many researchers have been investigating how to create and control such arrays using a variety of techniques. For example, ligand-mediated assembly is being studied using a variety of ligands. DNA ligands, in particular, offer a powerful way to control NP assemblies [8]. Evaporative self-assembly has been used to create large supercrystals of one, two, and even more types/sizes of NPs [9-12]. Assisted assembly incorporating electric and/or magnetic fields has shown promise in creating ordered NP arrays [13-15]. Spin-casting and Langmuir Blodgett films can be used to create very thin NP films [16, 17]. Templated substrates in combination with spin coating have been used to order block-copolymers; this could be adapted for NP arrays as well [18].

Some of these techniques can be applied for forming ordered arrays of NPs in two-dimensions, creating nanoparticle monolayers (NPMs), the focus of this work. NPMs are attractive for many applications in devices such as magnetic storage, solar cells, and biosensors [1-4]. One particularly attractive feature of NPMs is the high surface area to volume ratio of the films. For example, through collaboration, we are investigating PL properties of two monolayers, composed of two different types of NPs, stacked on top of one another. By stacking the monolayers, it is possible to increase interactions between

the different NPs while limiting the amount of total NPs used. NPMs are important, additionally, in that they allow one to study the growth of films in a highly controlled way that may offer insight into the growth of thicker films.

Although challenging, there now are a variety of techniques for the fabrication of NPMs [11, 12, 16, 17]. This dissertation introduces a new process by which one can fabricate monolayers, electrophoretic deposition (EPD) [13, 14, 19, 20]. Literature exists on using EPD to fabricate NPMs, but this literature is very limited [21, 22]. One such study deposited films of Au NPs on carbon films and another Pt NPs on carbon films. To the best of our knowledge, only NPMs of metallic NPs on carbon have been fabricated. Of the EPD studies in which NPMs have been fabricated, the technique has not been investigated in depth or has not been generalized for deposition of many types of materials.

If NPM formation via EPD could be generalized, the NPMs could be industrially attractive as EPD has many industrially advantageous properties. For instance, EPD is highly versatile in multiple ways: many types of particles can be deposited, the size of the electrodes can be varied over many orders of magnitude, and a large variety of solvents can be used to suspend NPs. For example, our group has deposited materials of different shapes including tubes, sheets, and spheres; different materials such as polymers, metals, semiconductors, and magnetic materials; and on a variety of substrates including steel, silicon, silicon dioxide, indium tin oxide, and gold [23-27]. In addition, EPD is very simple to perform, forms smooth films, and forms films quite rapidly [23, 24, 28-32]. By fabricating NPMs of many types of NPs, the technique used herein has proven to be generalizable and thus could be industrially attractive.

Other approaches to NPM formation include Langmuir-Blodgett, evaporative self-assembly, and spin casting. Of these three, evaporative assembly has made tremendous progress in making highly controlled NPMs [9, 10, 33, 34]. However, none of these techniques offer the scalability and rapidity of EPD, making EPD stand out as an industrially attractive alternative.

As fabrication of NPMs via EPD has not been well studied, our work began by studying the fundamental processes occurring during NPM formation and our attempts to understand why ordering occurs in the NPMs. For example, as the films discussed herein are composed of magnetic NPs (iron oxide and cobalt ferrite); perhaps magnetic interactions between NPs generated order in the NPMs. By understanding why ordering occurs in the NPMs, it will be possible to then begin to tune the ordering in the films and thus to tune the properties of the NP arrays.

To begin, details behind the general theory behind the EPD process as well as the general theory behind magnetism at the nanoscale will be introduced. These chapters will set the stage for understanding the behavior of the NPs as they are depositing and arranging on the substrate. Then, the properties of selected NPs and the suspensions used to make NPMs will be shown. Next, features of monolayer formation via EPD will be discussed, followed by an introduction on how order can be measured in these NPs. Then, the mechanisms that generated order, first, in the iron oxide NPMs and, second, in the cobalt ferrite NPMs will be studied. Order between the two systems is significantly different and likely arises due to different mechanisms.

CHAPTER II

ELECTROPHORETIC DEPOSITION

Electrophoretic deposition (EPD) is a process used to deposit colloidal particles, suspended in liquid, onto a surface by inducing particle motion via electric fields. In the EPD process, particles electrophorese toward a substrate from which an electric field originates, whereupon the particles irreversibly deposit (Figure II.1). In comparison to other liquid-phase, colloid-based, thin-film-fabrication techniques, EPD offers many attractive features making it suitable for industrial applications. Such attractive features of EPD include scalability, rapidity, simplicity, ability to conformably coat surfaces, ability to form smooth films, and versatility of particles and solvents [21, 23, 24, 28-32, 35-38].

The work discussed within this dissertation incorporated *nonpolar solvents* into the process of EPD. A few topics will be discussed in this chapter. First, how NPs are suspended in nonpolar solvents will be reviewed. Next, the origin of charges in nonpolar solvents will be introduced. Finally, the effects of introducing an electric field to a NP suspension will be explained. The use of nonpolar solvents in EPD offers many attractive features, yet is not as well studied or as commonly used in industrial applications as EPD performed in polar solvents. For this reason, the use of nonpolar and polar solvents during EPD will be compared.

2.1 How NPs are suspended

In order to make smooth films using EPD, it is essential that the single NPs that will make up the film are suspended as individual particles within a solvent, i.e. the NPs do not aggregate or agglomerate in the suspension. Such colloidal stability is often

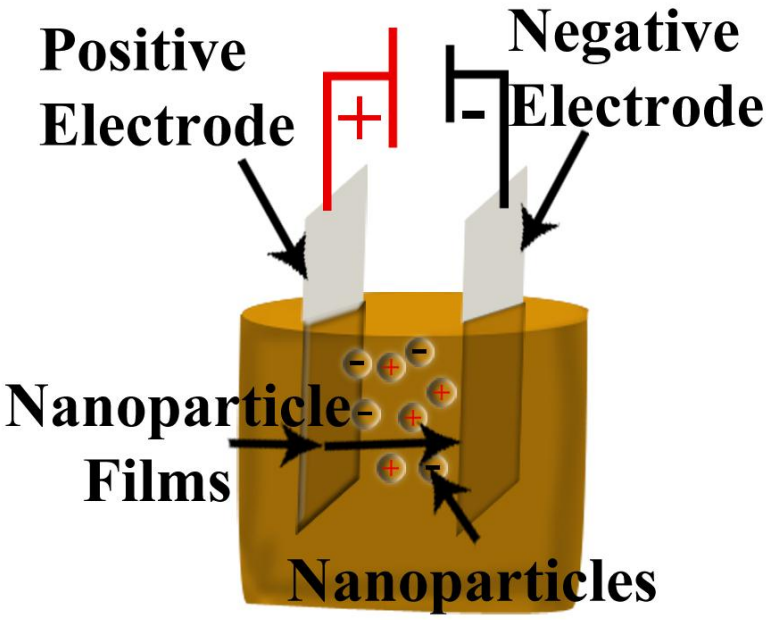

Figure II.1: A schematic of an electrophoretic deposition setup is displayed. Two substrates (electrodes) are inserted in the beaker. An electric field is created within the suspension by the application of a potential across the two electrodes. Charged particles migrate toward the electrodes where they deposit, creating thin films.

explained using DLVO theory, named after the four scientists that initiated the theory: Derjaguin, Landau, Verwey, and Overbeek [39, 40]. DLVO theory explains colloidal stability by calculating the electrostatic and London-van der Waals interactions that occur between two particles (Figure II.2). In DLVO theory, electrostatic interactions are

repulsive as the sign of the charge of each particle within the colloidal dispersion is assumed to be the same. Van der Waals interactions are attractive as the interaction occurs between two, like particles. If repulsion between two particles is stronger than attraction, the suspension is considered stable. Charged species are introduced to a suspension by the addition of dissociable compounds such as salts, acids, and bases.

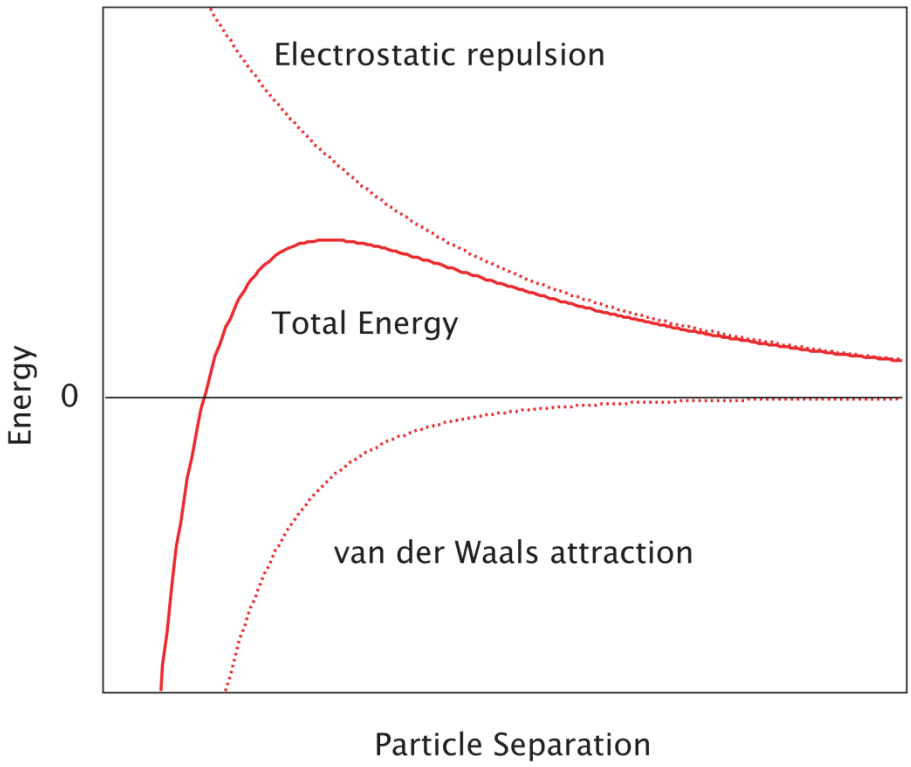

Figure II.2: The graph represents DLVO theory. Electrostatic repulsions and van der Waals attraction compete with each other. When repulsive forces are stronger than attractive forces, the suspensions is stable.

When working in polar solvents, these compounds easily dissociate, and all the particles in the suspension will obtain either a net positive or a negative charge (with a cloud of counterions that partially shields this charge). Thus, electrostatic repulsion between particles acts to stabilize the suspension.

While electrostatic repulsion may stabilize particles in *polar* solvents, such a mechanism of stabilizing colloidal dispersions often fails in *nonpolar* solvents. Dissociable compounds do not dissociate as readily in nonpolar solvents as they do in polar solvents; thus, inducing charge on all the particles suspended in nonpolar solvents is difficult. Assuming that electrostatic repulsion and van der Waals interactions are truly the only forces present, van der Waals attraction will cause particles in nonpolar solvents to stick together and eventually to fall out of suspension when Brownian motion can no longer overcome the downward pull of gravity.

To overcome this challenge, colloidal stability in nonpolar solvents is engineered into the suspension by introducing steric interactions between particles. Steric interactions are typically strongly repulsive interactions that arise when overlap of electron orbitals threatens to violate the Pauli Exclusion Principle. More basically, steric interactions occur when two objects attempt to occupy the same space. Though strong, steric interactions are typically very short in range.

Engineering of steric interactions is accomplished by coating the NPs with a surfactant. A surfactant is typically a chain-like, organic molecule that has amphiphilic geometry, one side of the molecule is hydrophilic and the other side is hydrophobic. Some common surfactants employed in NP suspensions are oleylamine, trioctylphosphine oxide (TOPO), oleic acid, and dioctyl sodium sulfosuccinate (AOT) [9, 19, 33, 41-46]. When a surfactant coats a particle in a nonpolar solvent, the molecule will typically orient with the hydrophilic head near the particle and the hydrophobic tail sticking out in the suspension. When many surfactant molecules arrange around a particle in this manner, a reverse micelle structure is created. For synthesized NPs, the reverse

micelle can form during or after the synthesis. When two particles that are coated in a reverse micelle approach one another, they repel due to steric interactions from the overlap of the surfactants. In this manner, van der Waals interactions are limited by preventing the particles from approaching one another too closely.

Additionally, by varying the length of the surfactant, it is possible to control the separation distance between the NPs, and thus control the interaction strength between particles. When a surfactant is used that is too short to stabilize the particles, attractive interactions between particles, such as van der Waals or magnetic dipole interactions, may still cause agglomeration.

2.2 Origin of charge

Dissociable compounds do not readily dissociate in nonpolar solvents. This means charge is typically not abundant in nonpolar-solvent-based suspensions. Yet, some charge must still exist for electrophoresis of the particles to occur. The origin of such charge is not completely understood, but some studies have begun to uncover how charged species can be stabilized in nonpolar solvents [41, 42, 47]. In these studies, surfactants were shown to play an important role in charge stabilization using a similar concept to that which explained steric stabilization of colloidal particles. The surfactant forms a reverse micelle around an ion preventing neutralization by oppositely charged ions. Inducing charge on particles in nonpolar solvents could occur by multiple mechanisms. Possibly, an ion may adhere to the surface of the particle; the ion can be stabilized be the same reverse micelle that stabilizes the particle itself. Alternatively, one of the surfactant molecules that form the reverse micelle may be charged.

With these ideas, theories on how charging occurs on iron oxide NPs (the type of NPs discussed in this dissertation) can be posed. The iron oxide NPs were suspended in

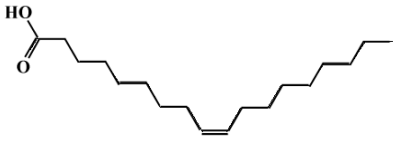

Figure II.3: Oleic acid molecule

hexane or other nonpolar solvents using oleic acid as a surfactant. Oleic acid ($C_{18}H_{34}O_2$, Figure II.3) is a long chain molecule with one double bond in the middle and a carboxyl group (COOH) on one end. The end with the carboxyl group is the hydrophilic end that will face toward the NP. Being an acid, the hydrogen atom on the carboxyl group can dissociate from the molecule, leaving the molecule negatively charged. The free H^+ ions can then adsorb on the surface of NPs and become stabilized by reverse micelles of oleic acid around the NPs. Indeed, addition of oleic acid in a nonpolar solvent based suspension of iron oxide NPs leads to positive mobility of the NPs, indicating the presence of positively charged NPs [10, 48]. Before addition of oleic acid, particles with both positive and negative mobilities were observed, indicating both positively and negatively charged NPs (Figure II.4). The positive charge likely occurs by the former previously discussed mechanism. The negative charge, however, possibly occurs when a dissociated oleic acid molecule is incorporated into the reverse micelle coating that stabilizes the NP [49]. Another possibility is that negative ions left over from synthesis cause the negative charge. When the NPs are synthesized, negative ions, typically chloride, are introduced into the mixture. Possibly, these chloride ions remain in the

suspension, adhering to the NPs where they are stabilized by a reverse micelle; thus, the NPs acquire a net negative charge.

2.3 The effects of electric fields and potentials on suspensions

Thus far, a discussion on how particles can be stabilized and charge can be induced on particles in both polar and nonpolar solvents has been provided. Next, how suspensions behave in the presence of an electric field will be examined. As in the previous discussion, it will be shown that polar and nonpolar suspensions behave quite

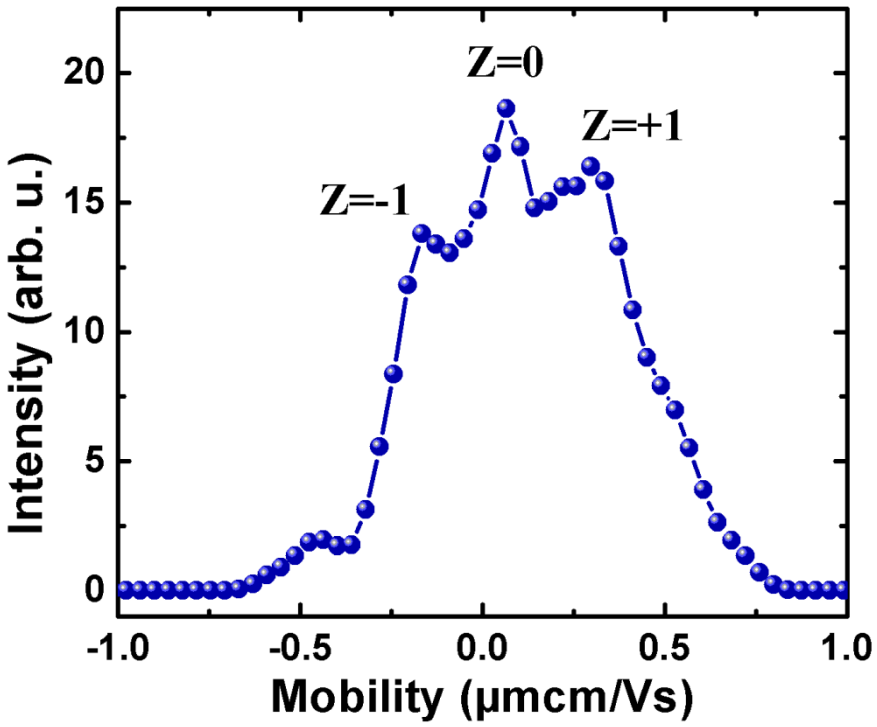

Figure II.4: Mobility graph demonstrating NPs with both surface charges. The peaks labeled Z=-1, Z=0, and Z=+1 correspond to NPs with -1, 0, and +1 elementary charge unit.

differently. In fact, nonpolar suspensions are in many ways simpler than polar suspensions. This simplicity will be important throughout this dissertation in determining how particles behave during the EPD process.

This section is divided into two parts. In the first part, some important differences between polar and nonpolar solvents under an electric field will be highlighted. The second part will introduce the concept of the double layer and will examine how polar and nonpolar solvents may produce double layers with very different properties.

2.3.1 Polar versus Nonpolar Solvents

Polar solvents are commonly used to suspend particles for use with EPD. Polar solvents can be advantageous compared to nonpolar solvents because they can be inexpensive, environmentally friendly, and safe. Nonpolar solvents are often more expensive and toxic; however, nonpolar solvents can offer many advantages over polar solvents when performing EPD.

2.3.1.1 Electrolysis

A major advantage of using nonpolar solvents for EPD is that the solvent does not undergo electrolysis, a phenomenon that strongly interferes with EPD in polar solvents [50, 51]. When applying an electric potential in water, a voltage of ~1.5V will cause the water molecules to electrolyze, resulting in the evolution of H_2 and O_2 gas at the surfaces of the electrodes. The gas creates bubbles, and where there are bubbles, particles cannot deposit. Thus, smooth films cannot be obtained when bubbles form on the surface of the electrode. Nonpolar solvents, however, can experience much larger potentials without breaking down; we have demonstrated that hexane is stable up to 1000V. The range of electric potentials that can be used in hexane, however, is not unlimited. Hexane will

eventually break down at ~10 kV [52]. The absence of electrolysis means a wide range of voltages can be employed in the fabrication of films via EPD.

2.3.1.2 Electrohydrodynamic Flows

Another difference between polar and nonpolar solvents is that nonpolar solvents do not experience electrohydrodynamic flows at macroscopic scales. When a polar molecule is in the presence of a temporally or spatially varying electric field, a phenomenon called dielectrophoresis can occur. Dielectrophoresis is caused by the electric field gradient pulling with a different force on the polarized parts of a molecule. This force, when applied on all the molecules within a fluid, can create a flow within the fluid. Such fluid flows can be advantageous for controlling the morphology of a film; however, the fluid flow can also complicate the kinetics of a particle making it difficult to study interactions between particles as they deposit [53-55],

2.3.1.3 Current Flow through Electrodes

Finally, a comparison between the sources of current measured during EPD for polar and nonpolar solvents will be provided. The current that flows through the suspension and into the electrodes occurs from many sources including: discharge of the deposited NPs, electrolysis, and electrochemical reactions at the electrode surface. In polar solvents, all of these sources can significantly contribute to the observed current. This makes the current *versus* time profile acquired during the deposition processes difficult to interpret; however, in nonpolar solvents, the current may be more easily tractable. No electrolysis occurs, eliminating this source of current. Also, electrochemical side reactions at the electrode are typically less numerous in nonpolar solvents than in

polar solvents. This means the discharge of the NPs as they deposit is a major contributor to the observed current.

The simplified current data obtained when using nonpolar solvents may allow one to accomplish two objectives that have been difficult to do in polar solvents. First, we believe that it will be easier to study the nature of the NP discharge in nonpolar solvents than it will be in polar solvents, an open topic of interest in the EPD community. Second, if the current profile can be divided into the individual processes that create the current, it would be possible to correlate the current profile to the film density. With such a correlation, film density could be precisely controlled and easily studied.

Polar solvents and nonpolar solvents behave much differently. These differences, however, do not result in an innate advantage of one type of solvent over the other. Both types of solvents can be used advantageously. Though, in general the nonpolar solvent behavior appears to be less complex. This reduced complexity is used to study fundamental interactions between NPs during EPD.

2.3.2 Double Layer

The term *double layer* refers to the layers of charge that surround a surface that is exposed to a fluid. Double layer theory models how ions arrange around this surface (Figure II.5). During EPD, there are two important types of surfaces to understand, the surface of a particle and the surface of an electrode. Double layers will occur on both of these types of surfaces. As the name implies, the double layer is composed of two layers:

(1) Stern Layer – This is the layer of ions adsorbed on a surface in a fluid. Since the ions are adsorbed, this layer of charges will travel with the object during electrophoresis.

(2) Diffuse Layer – This is the layer of charges that resides beyond the Stern Layer. The diffuse layer forms because of electrostatic interaction of the free ions in the suspension with the electric field emanating from the surface. The diffuse layer acts to electrically screen the field emanating from the surface. It is less associated with the particle, thus the morphology and composition will change when the surface moves.

Electric fields emanating from a surface may be generated in two ways. First, ion adsorption on the surface may create a net surface charge (Stern layer), generating an electric field around the surface. In this way, the Stern Layer and diffuse layer have *opposite net charge* to each other. In EPD, the suspended particles emanate electric fields because of a net charge produced by ion adsorption. Second, an electric field can be generated by the external application of an electric potential, as occurs between the electrodes in EPD. In this instance, the Stern layer and diffuse layer have the *same net charge* and both shield the electric field emanating from the surface.

As one travels along electric field lines emanating from a charged surface (either an electrode or a charged particle), according to the electrostatic definition of the potential as the negative line integral of the electric field, the potential must vary. The discussion applies equally to both electrode and particle surfaces; however, where a distinction between the two surfaces is important, the type of surface will be specified.

The Stern layer, being adsorbed on the surface of the electrode, causes a rapid decay (growth in the case of a particle) in potential over a very short distance; however, the diffuse layer causes a much slower decay of the potential (Figure II.5). The decay of potential due to the diffuse layer can be predicted by modeling the charge distribution

within the diffuse layer. Thermal energy and energy from the ions coupling to the electric field emanating from the surface creates a Boltzmann distribution of ions around the surface. From basic electrostatics, the charge distribution is also related to the potential by the Poisson equation. Combining these two equations, a mathematical model of the diffuse layer can be expressed as the Poisson-Boltzmann equation,

$$\epsilon \frac{d^2\psi}{dx^2} = -\sum_{i=1}^{N} z_i e n_{i\infty} \exp(-\frac{z_i e \psi}{k_B T}) \qquad \text{(Equation II.1)}$$

where ε denotes the dielectric permittivity of the suspension, ψ is the electric potential, x is the distance from the surface, i is an index for each charged species, N is the number of different charged species, $n_{i\infty}$ is the concentration of charged species i far from the electrode, and z is the valence charge of each charged species. In the case of a symmetric electrolyte (two charged species with $z_1 = -z_2$) and a planar surface, an analytical solution for ψ can be obtained using the Guoy-Chapman theory (Figure II.5) [56].

In addition to the Stern Layer and diffuse layer, there are two other interesting points along the potential curve, the slipping plane and the double layer size. The slipping plane is usually encountered first when moving away from the surface. When a surface (electrode or particle) translates relative to the fluid in which it is immersed, a thin layer of fluid will translate with the particle. The interface that separates the fluid that translates with the surface and the fluid that does not is called the slipping plane. For a particle undergoing electrophoresis, it is the potential at the slipping plane, called the ζ-potential (zeta potential), that is of interest [56]. In polar solvents, where colloidal dipsersions are electrostatically stabilized, the stability of the suspension is often described using the ζ-potential. A ζ-potential with magnitude of <30 mV is typically

poorly stabilized and >40 mV is typically well stabilized. For nonpolar solvents, the ζ-potential can be useful for describing the potential of a particle that will couple with an externally applied field. The ζ-potential in nonpolar solvents does not typically describe colloidal stability because the dispersions are usually sterically stabilized rather than electrostatically stabilized.

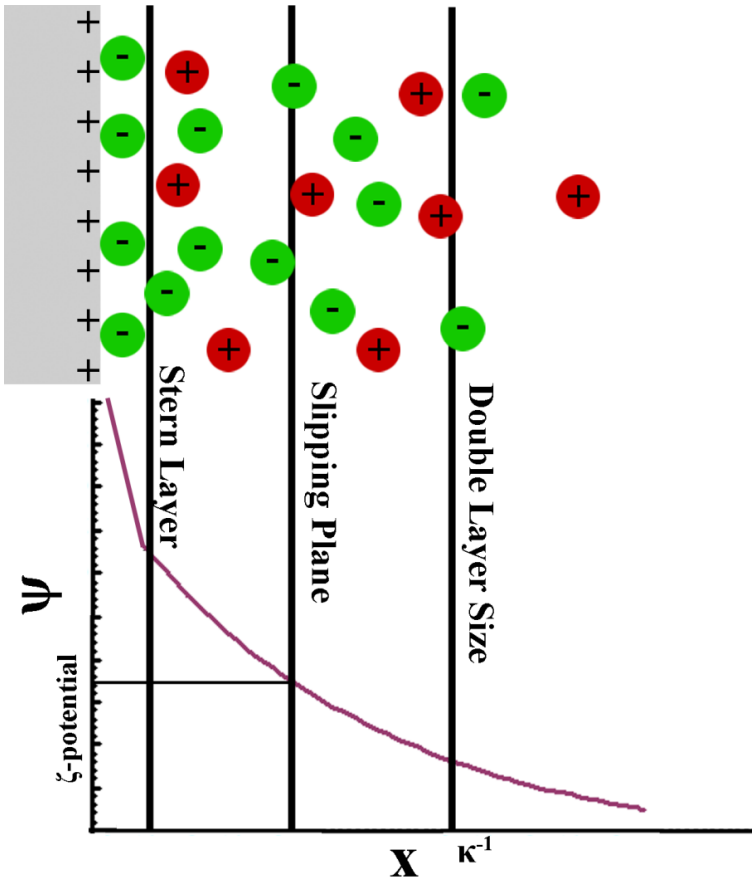

Figure II.5: The top half of the figure shows a positively charged electrode (gray). Negative charges adhere to the surface of the electrode, forming the Stern layer. The other ions around the electrode form the diffuse layer, shielding the field generated by the substrate. Fluid between the slipping plane and the surface will travel with the surface when it moves relative to the surrounding fluid. The double layer size is an indication of how quickly the potential decays as a function of distance from the surface. Suspended NPs will have similar double layer structures, however the Stern layer and diffuse layer will have opposite net charge.

The second interesting point along the potential curve is the double layer size (or thickness). Thickness is important to understand because the it affects the motion of a surface (in EPD, the surface is that of a suspended particle) in a solvent. The thickness (size) of the double layer is characterized by the Debye length (κ^{-1}) where,

$$\kappa^2 = \frac{e^2}{\epsilon k_B T} \sum_{i=1}^{N} z_i^2 n_{i\infty} \qquad \text{(Equation II.2)}$$

The double layer thickness depends on the dielectric constant of solvent as well as on the concentration and charge of ionic species present [56]. The relative dielectric constant of water, a polar solvent, is ~80 at room temperature, while that of hexane, a nonpolar solvent, is ~1.9. However, the concentration of charged species in polar solvents is typically higher than that in nonpolar solvents. So, despite the large dielectric constant of nonpolar solvents, the low concentration of charges present in nonpolar solvents will typically lead to larger double layer thicknesses than those observed in polar solvents. A thick double layer, often observed in nonpolar solvents, indicates a slow decay in the potential around the surface, and a thin double layer indicates a rapid decay in potential.

In addition to understanding the potential decay around a surface, the double layer thickness is important in the calculation of the zeta potential of a particle from electrophoretic mobility measurements. The electrophoretic mobility is defined as

$$\mu_E \equiv \frac{v}{E} = f(\kappa a)\frac{\epsilon\zeta}{\eta} \; where \; f(\kappa a) = {}^2/_3 \; for \; a \; sphere \; if \; \kappa a \ll 1 \qquad \text{(Equation II.3)}$$

where v is the particle velocity, E is the electric field strength, a is the particle radius, η is the suspension viscosity, ζ is the zeta potential, and $f(\kappa a)$ is a constant that depends on the double layer thickness and the particle radius. The mobility can be determined by measuring the velocity of a particle under a known applied field. Theoretically, the

observed mobility can be modeled by three forces: the coupling of the particle charge with the applied electric field, drag force, and the electrophoretic retardation force. The retardation force arises from counterions within the double layer moving in the opposite direction of the particle, changing the apparent local viscosity of the fluid around the particle. It is this force that makes the double layer thickness important when calculating the zeta potential. In the case of $\kappa a \gg 1$, indicating that the double layer tightly surrounds the particle, $f(\kappa a) = 1$ for a spherical particle. This is called the Helmholtz-Smoluchowski approximation, which occurs if there is a high concentration of ions present in the suspension. In the limit of $\kappa a \ll 1$, the double layer is very large, and $f(\kappa a) = 2/3$ for a spherical particle. This scenario is common in nonpolar solvents and is called the Hückel approximation. These values both describe limiting cases; real values of $f(\kappa a)$ will be between 2/3 and 1 for spherical particles.

This chapter will end by noting an interesting phenomenon observed in iron oxide NP suspension. In the dissertation of Dustin Kavich from Vanderbilt University, the charge state of individual colloidal NPs was calculated from the measured electrophoretic mobility of the NPs [48]. The calculation was performed using the equation

$$\mu_E = \frac{Ze}{6\pi\eta a} \qquad \text{(Equation II.4)}$$

This equation comes from Stokes' law for drag force on a sphere and the force on the charged particle from the electric field. From this calculation, Z, representing the charge state on the particle, was found to be ~1. In such a situation, a single counterion would have the same charge as the particle. Given this fact, the use of a statistical distribution (Poisson-Boltzmann distribution) is not appropriate for describing a diffuse layer composed of a very small number of ions. Thus, on the nanoscale where particle charges

can be as low as one elementary charge unit, the double layer should be modeled using a discrete model. The Hückel approximation of the mobility however, is likely to still be valid as little retardation force will occur from the discrete diffuse layer. The question of the discrete double layer may be an interesting direction for future research.

CHAPTER III

NANOMAGNETISM

Magnetism at the nanoscale gives rise to unique phenomena not observed in larger magnetic materials. Two such phenomena that will be introduced are the creation of single domain ferromagnetic particles and the phenomenon of superparamagnetism.

If a ferromagnetic particle becomes small enough, it will contain only one magnetic domain. This is called a single domain magnet and is characterized by the particle having uniform magnetism throughout the entire volume (ignoring surface effects). When this occurs, the particle is a single magnetic domain and can be treated as one single superspin. The assembly of such single-domain NPs allows one to study new fundamental science as well as create materials for applications such as magnetic storage [34, 57-60].

Another nanoscale phenomena, called superparamagnetism, arises when a ferromagnetic NP shrinks below a critical size at a specified temperature. In this phenomena, a single domain NP becomes unstable because of the thermal energy present, resulting in the moment of the NP randomly flipping directions.

The following sections will begin by delving into fundamental concepts behind the origin of magnetism and magnetic ordering. Next, magnetism of nanoparticles will be discussed by introducing single domain magnets and superparamagnetism. Finally, the application of these concepts to magnetite and cobalt ferrite crystals, both of which are used in this dissertation, will be explored.

3.1 Origin of magnetism

Magnetism originates from a charged particle that displays angular momentum. In quantum mechanics, angular momentum exists in two forms, orbital angular momentum and spin angular momentum. The orbital angular momentum can be modeled classically (a point-like electron orbiting an atomic nucleus) to obtain an equation for the magnetic moment:

$$\overrightarrow{\mu_L} = -g_L \frac{e}{2m} \vec{L}, \qquad \text{(Equation III.1)}$$

where e is the electron charge, m is the electron mass, $\vec{L}$ is the orbital angular momentum of the electron, and g_L is the electron orbital g-factor. g_L is not part of the classical model, but because $g_L = 1$, the classical model produces an equivalent result to the quantum mechanical model.

The spin angular momentum of an electron occurs from an intrinsic, quantum mechanical property of the electron. The spin quantum number is always ½ for the electron. In the case of spin, a classical model of a spinning electron does not predict the correct magnetic moment exhibited by an electron. The magnetic moment due to spin is

$$\overrightarrow{\mu_s} = -g_s \frac{e}{2m} \vec{S}, \qquad \text{(Equation III.2)}$$

where $\vec{S}$ is the spin of the electron and g_s is the electron spin g-factor. Deviation from the classical model is observed because the factor $g_s \approx 2$, whereas a classical model would predict $g_s = 1$.

Combining the spin momentum and the orbital momentum, one can express the net magnetic moment of an electron as

$$\overrightarrow{\mu_J} = -g_J \frac{e}{2m}\vec{J} = {-2\pi g_J \mu_B \vec{J}}/{h}, \qquad \text{(Equation III.3)}$$

where $\vec{J} = \vec{L} + \vec{S}$ is the total angular momentum, μ_B is the Bohr magneton, ħ is the reduced Planck constant, and g_J is the Landé g-factor.

3.2 Magnetism in dielectrics

The discussion thus far has focused on magnetism arising from single electrons. Naturally, the discussion will now transition to multiple electron systems. To begin, magnetism in single atoms will be discussed. Then, systems with little to no magnetic order (paramagnetism) will be introduced, followed by magnetically ordered systems (ferro-, antiferro-, and ferri-magnetism). Finally diamagnetism, which occurs in all materials, will be introduced. It is typically the spin momentum that most significantly contributes to the magnetic moment of dielectrics, thus, the focus of the discussion is on electron spins. Superparamagnetism, which occurs from nanoscale effects of ferromagnetic materials, will be discussed in a later section.

As the section title states, the following discussion will be on magnetism within dielectric materials, where the electrons are localized. In systems with delocalized (or itinerant) electrons such as metals the discussion below does not apply. Magnetic ordering can exist in such systems; however, the mechanisms and models describing the magnetic behavior will likely be different.

3.2.1 Magnetism in Atoms

Magnetism in atoms can be explained using Hund's Rule. Hund's rule is used to predict the quantum states of each electron of a multi-electron system in the ground state. The rule states that for a given electron configuration, energy is minimized when

multiplicity is maximized. The multiplicity is equal to $2S + 1$, where S is the total spin angular momentum in the system, thus, maximum multiplicity occurs at the highest value of S. As shown in Section 3.1, a nonzero S will give the atom a net magnetic moment.

3.2.2 Magnetic Ordering Between Atoms

3.2.2.1 Paramagnetism

Paramagnetism, in the purest sense, occurs when a system of unpaired electrons do not interact with one another. If such a system is at a temperature of absolute zero, any applied magnetic field ($\vec{H}$) would completely align all the moments within the sample resulting in a net magnetization ($\vec{M}$) equal to the sum of all the electron magnetic moments (saturation). At any other temperature, however, the alignment of the electron spins follows a Boltzmann distribution. The $|\vec{M}|$ versus $|\vec{H}|$ curve (hysteresis curve) arising from such statistical distribution are described by the Langevin function (classical) or the Brillouin function (quantum mechanical). In the case of small applied fields or high temperatures, Curie's Law can be used to describe the system. Two real systems that behave similar to an ideal paramagnetic include lithium and a dispersion of magnetic ions or atoms within a diamagnetic matrix [61, 62].

3.2.2.2 Ferromagnetism

Ferromagnetism occurs when unpaired electron spins within a material spontaneously align parallel to one another. A ferromagnetic material will exhibit hysteretic behavior, which can be utilized for magnetic storage. When a ferromagnetic material is heated to its Curie temperature, thermal energies will suppress the ordering displayed by the electron spins. At this point, the material behaves paramagnetically.

The alignment of electron spins in ferromagnets is due to a quantum mechanical interaction called the exchange interaction, which arises due to the indistinguishability of electrons. Exchange interactions between two electrons are from the effects on the wave functions resulting from an exchange of the spatial coordinates of the electrons. The exchange interaction is often modeled using a Heisenberg Hamiltonian for two interacting spins,

$$\left|\vec{H}\right| = -\sum_{i<j} J_{ij}\vec{S_i}\cdot\vec{S_j}, \qquad \text{(Equation III.4)}$$

where J_{ij} is the exchange integral, $\vec{S}$ is the spin momentum vector for two electrons [63]. A positive exchange integral indicates parallel alignment between interacting spins, and so the material is ferromagnetic. In the case of a negative exchange integral, antiparallel alignment may occur between spins, causing antiferromagnetic behavior.

3.2.2.3 Antiferromagnetism

Antiferromagnetic materials are materials with antiparallel alignment between spins and are described by a negative exchange integral. The net moment of such a material is zero because the antiparallel spins cancel each other (ignoring uncompensated spins at the material edge). Antiferromagnetic ordering is lost when a material is heated past its Néel temperature. As an example, the iron oxide FeO (wüstite) exhibits antiferromagnetic behavior at room temperature [64].

3.2.2.4 Ferrimagnetism

In materials that display ferrimagnetism, unpaired, localized spins in the material align antiparallel to one another. However, ferrimagnetism differs from antiferromagnetism because the net spin moment is not completely cancelled. This

occurs, for example, in magnetite (Fe_3O_4) and cobalt ferrite ($CoFe_2O_4$) because the spins from two of the metal atoms within the unit cell align parallel to each other but antiparallel to the spin from third metal. Thus, a net magnetic moment can be measured for the material. Magnetism is these materials is described in more detail in Section 3.4.

3.2.2.5 Diamagnetism

Finally, diamagnetism, which is the property of a material that causes the material to acquire a moment that opposes an external magnetic field, is introduced. Diamagnetism is not due to spin ordering as the other magnetic behaviors discussed, but instead diamagnetism describes a response to an applied magnetic field. All materials display some level of diamagnetic behavior, even a system composed of only hydrogen ions [65]. However, a material is only called diamagnetic if diamagnetism is the only contribution to the magnetism in the material. The diamagnetic behavior is often misattributed to Lenz law but is in fact a quantum mechanical effect based on the Larmor precession of an electron within an applied magnetic field. The behavior can be described with the Langevin model of diamagnetism. Interestingly, it is the diamagnetism of superconducting materials that gives rise to magnetic levitation [66].

3.3 Single domain magnets

In a ferromagnetic material, a magnetic domain is a region within a magnetic material where all electron moments are aligned; thus, it can be characterized by uniform magnetization. Within a large, ferromagnetic, single-crystalline material under a zero applied field, magnetic domains will exist. The magnetic moments of different domains will point in semi-random directions (with some preference for particular crystal axes). If this large ferromagnetic material is shrunk, the number of domains will decrease. At

small enough sizes, the magnet will become single domain. Magnetic domains require energy to form, and the formation of single domain magnets can be described using energetics. A thorough introduction to the formation of single domain particles was published by Charles Kittel in 1949 [67]. In the following, the theory behind origin of single domain magnets will be discussed as well as ferromagnetic behavior of single-domain magnets. Finally, superparamagnetic behavior, which occurs when single domain ferromagnets become sufficiently small that the magnetization can randomly flip within the material under the influence of temperature, will be introduced.

3.3.1 Magnetic Energies in Ferromagnetic Materials

The region that divides two magnetic domains is called the domain wall. Within the domain wall, the electric spins change direction to cause a smooth transition in the magnetic moment direction between the domains. The formation of a domain wall is energetically expensive; however, the multidomain structure decreases other forms of energy within a magnet. Four forms of energy are important in the study of domain formation.

(1) Exchange energy: As discussed previously, exchange interactions between electrons give rise to magnetic order. In the Heisenberg Hamiltonian, energy is minimized when spins are parallel in a ferromagnetic material. In a domain wall, the spins must tilt relative to one another to reorient the moment of the two neighboring domains. Because the spins are not parallel, there is an increase of energy due to exchange interactions associated with the domain wall.

(2) Magnetocrystalline Anisotropy Energy: Within a crystal, the magnetic moment prefers to align in a particular direction relative to the crystal lattice. The preferred

crystalline direction is called the easy axis. This preference is believed to arise by an indirect coupling of the electron spins with the crystal lattice of the material. The indirect coupling is accomplished via spin-orbit coupling and orbit-crystal field coupling. Within the domain wall, spins are oriented in many directions. Some of these spins will likely point in energetically disfavorabledirections relative to the crystal lattice resulting in anisotropy energy. This energy is mathematically modeled using a Taylor series. For a uniaxial crystal, the energy is

$$E = K_1 V \sin\theta^2 + K_2 V \sin\theta^4 + \cdots, \qquad \text{(Equation III.5)}$$

where E is the energy, K_i are the anisotropy constants, and θ is the direction of the moment relative to the easy axis. Typically, anisotropy constants up to K_2 are sufficient to describe the anisotropy energy. The concept of anisotropy energy will be employed again to help explain superparamagnetic behavior.

(3) Magnetoelastic energy: This is the energy due to interactions of the magnetization of the material with the mechanical strain of the crystal. The crystal structure of a material may alter in the presence of a magnetic field because the shift in structure decreases the anisotropy energy associated with the direction of the moment within the material. Altering the crystal structure then increases strain energy in the crystal; this is called magnetoelastic energy.

(4) Magnetostatic self-energy: As seen in the introduction of exchange energies, interactions between spins within a material can occur. In addition to exchange interactions, dipole interactions between spins are important. Self-energy can be thought of as the amount of energy required to assemble all the electron spins in a material due to dipole interactions. Self-energy can be minimized by forming

domains of closure, where no external magnetic field emanates from the material. Magnetostatic self-energy also leads to a phenomenon called shape anisotropy that is useful for stabilizing the magnetic moment of nanoscale ferromagnets.

As a ferromagnetic particle decreases in size, eventually the energy required to form the domain wall will outweigh the self-energy of the material. The size at which this occurs is typically ~10-50 nm. The competition of energies leads to the existence of single domain magnets.

3.3.2 Ferromagnetism in Single Domain Particles – Stoner-Wohlfarth Model

The Stoner-Wohlfarth model is an energetic model that predicts ferromagnetic behavior of a single domain magnet in the presence of an externally applied magnetic field [68]. Two energies are accounted for, magnetocrystalline anisotropy energy as well as Zeeman energy. Zeeman energy is the energy from the coupling of the particles magnetic moment to that of an external field, and is mathematically expressed by

$$E = \mu_0 \int_V \vec{M} \cdot \vec{H} dV, \qquad \text{(Equation III.6)}$$

where μ_0 is the magnetic permeability of free space, and V is the volume of the particle.

The net energy is then expressed as

$$E = KV\,sin(\varphi - \alpha)^2 - \mu_0 M_s V \left|\vec{H}\right| cos\,\varphi, \qquad \text{(Equation III.7)}$$

where φ is the angle between the magnetization of the particle and the applied field, α is the angle between the easy axis of the particle and the applied field, and M_s is the saturation magnetization of the particle (Figure III.1). The first term is the magnetocrystalline anisotropy energy and the second term is the Zeeman energy.

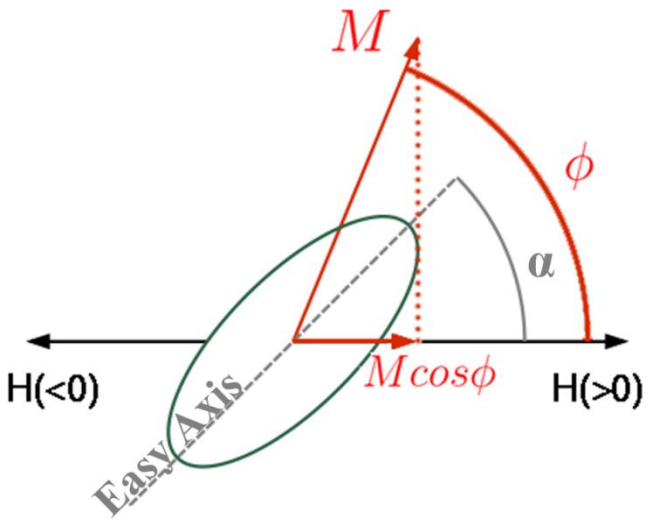

Figure III.1: Schematic of the Stoner-Wohlfarth model for a ferromagnetic, single-domain particle within an applied field. The magnetization of the particle will rotate due to the magnetic field. The competition of anisotropy energy and Zeeman energy produce ferromagnetic behavior.

3.3.3 Superparamagnetism

Superparamagnetic behavior is observed in small ferromagnetic, single domain particles and is explained by the random flipping of the magnetic moment of a particle to different easy crystalline axes. The flipping of the moment occurs when the magnetocrystalline anisotropy energy becomes comparable or less than the present thermal energy. The time scale over which the flipping occurs is characterized by the empirical Néel-Arrhenius equation

$$\tau = \tau_0 exp(^{KV}/_{k_B T}), \qquad \text{(Equation III.8)}$$

where τ is the average length of time that it takes for a random flipping to occur, τ_0 is called the attempt time and is specific to the material (typical values 10^{-9} s), KV is the

anisotropy energy, k_B is the Boltzmann constant, and T is the temperature [69]. It is important to note that the only difference between ferromagnetic and superparamagnetic particles is the time scale at which flipping of the magnetic moment occurs.

Superparamagnetic particles are often characterized by a blocking temperature, T_B. A particle is considered blocked when the temperature is low enough that the moment does not spontaneously flip during the time it takes to measure the moment. Mathematically, this is expressed as $\tau = \tau_m$, indicating that the average flipping time is equivalent to the measurement time. τ_m is a property of the measurement itself, with values on the order of 1 s. The blocking temperature, then, is a property of both the material and the measurement. The blocking temperature can be expressed as

$$T_B = {KV}\Big/{k_B ln(\frac{\tau_m}{\tau_0})}. \qquad \text{(Equation III.9)}$$

The blocking temperature is often found using zero-field cooled and field cooled magnetization measurements, which are collected *versus* temperature.

3.4 Magnetism in Magnetite and Cobalt Ferrite

To conclude this chapter, the nature of magnetism in magnetite (Fe_3O_4) and cobalt ferrite ($CoFe_2O_4$), both of which are the focus of this dissertation, will be discussed. The crystal structure of cobalt ferrite is nearly identical to the magnetite structure, but a cobalt atom replaces an iron atom. At room temperature, both crystals have *inverse* spinel crystal structures with very similar lattice constants (~8.39 Å) (Figure III.2) [70]. Such similar chemical compositions and crystal structures cause the two materials to behave similarly. Writing the chemical formula of magnetite as $(Fe^{3+})_A(Fe^{3+}Fe^{2+})_BO_4$, helps in understanding the crystal structure. The iron atoms in

magnetite occupy tetrahedrally coordinated sites (A) and octahedrally coordinated sites (B). In the case of a spinel crystal, all the 3^+ valence metals would be octahedrally coordinated. The *inverse* spinel crystals differs from the spinel because half of the 3^+

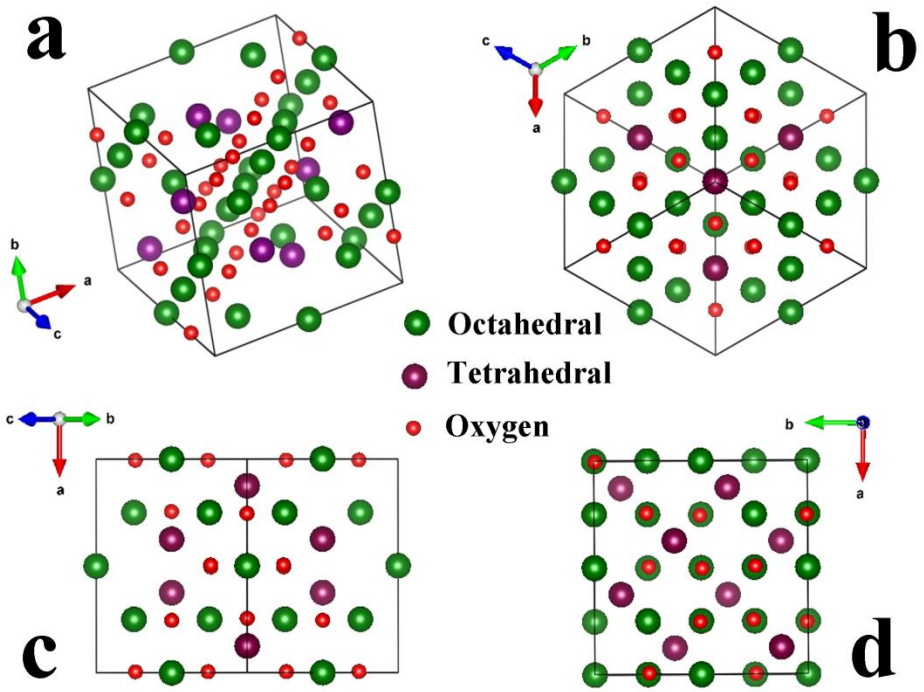

Figure III.2: Inverse spinel crystal structure. (a) shows a perspective view. (b) shows a view down the [111] axis, the easy axis of magnetite, (c) shows a view down the [110] direction, and (d) shows a view down the [100] axis, the hard axis of magnetite and the easy axis of cobalt ferrite. Green spheres represent octahedrally coordinated metals, purple are tetrahedrally coordinated metals, and red are oxygen atoms. The lattice constant of magnetite and cobalt ferrite are 8.39 Å.

valence metals are tetrahedrally coordinated and all the 2^+ valence metals are octahedrally coordinated.

The inverse spinel structure expresses cubic symmetry. The magnetic easy axis of magnetite is the <111> direction of the crystal, which has an 8-fold degeneracy [71]. The

hard axis of magnetite, which is the most energetically disfavorable direction for the magnetic moment to point, is in the <100> direction, meaning this is the most energetically disfavorable direction for the moments to point [72]. Knowing how the magnetic moment direction relates to the crystal lattice could allow one to infer the role of magnetic interactions by studying crystal axis alignment.

A net magnetic moment in magnetite occurs because the spins of all the octahedrally coordinated iron atoms are aligned parallel to one another and *antiparallel to the tetrahedrally cooridinated iron*. Thus, the magnetic moment of the five unpaired spins in Fe^{3+} ([Ar]$3d^5$) valence irons cancel each other, leaving the magnetic moment of the Fe^{2+} ([Ar]$3d^6$) uncompensated. Fe^{2+} has four unpaired spins, resulting in a $4\mu_B$ net magnetic moment (Figure III.3). Experimentally, the moment of Fe_3O_4, per chemical formula unit, has been measured to be $4.33\mu_B$, revealing some orbital contribution to the magnetic moment [73].

Cobalt ferrite behaves chemically very similar to magnetite. However, magnetically, the properties of magnetite are altered by replacing the Fe^{2+} with Co^{2+} ([Ar]$3d^7$). First, the number of unpaired spins has decreased to three, leading to a magnetic moment of $3\mu_B$ per cobalt atom (Figure III.3). Also, the magnetic easy axis changes to the <100> direction of the crystal and the hard axis to the <111> direction of the crystal when cobalt replaces the iron atoms [74-76]. Additionally, the magnetic

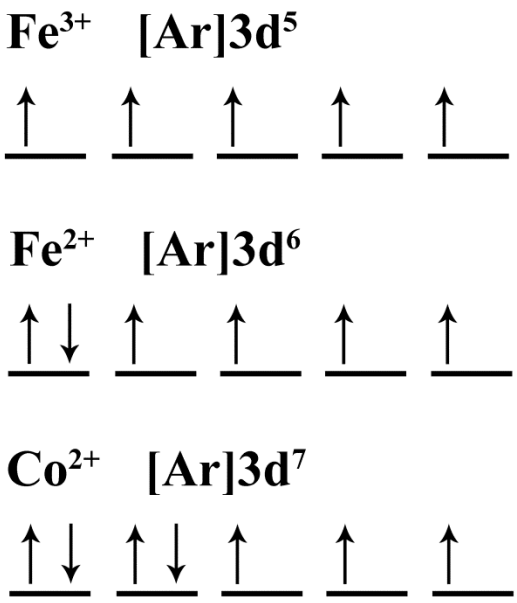

Figure III.3: Electron configuration of the 3d shell of Fe^{3+}, Fe^{2+}, and Co^{2+} according to Hund's rule, showing net magnetic moments due to electron spin to be $5\mu_B$, $4\mu_B$, and $3\mu_B$, respectively. The magnetic moment of the Fe^{3+} atoms cancel out in the magnetite and cobalt ferrite inverse spinel crystal.

anisotropy increases, allowing for smaller particles to remain ferromagnetic at room temperature [77]. Experimentally, the moment of $CoFe_2O_4$, per chemical formula unit, has been measured to be $3.2 - 3.9\ \mu_B$ [78, 79].

CHAPTER IV

NANOPARTICLE AND SUSPENSION PREPARATION AND CHARACTERIZATION

In order to understand the films that are fabricated by EPD, it is first important to measure properties of the constituents of the films (the NPs) as well as the suspension from which the films are fabricated. In regards to the NPs, some of the most important characteristics of the NPs are:

(1) NP Size Distribution and Shape – Changing the size and shape of a NP will affect the many properties of the NP such as magnetic, photoluminescent, and conductive properties; thus, a controlled size distribution and shape is essential if the NPs are to have uniform behavior. Additionally, a well-controlled size distribution and NP shape is required for obtaining well-ordered arrays of NPs.

(2) Chemical Composition and Crystal Structure – The chemical and crystalline nature of the NPs are important in understanding virtually all properties of the material. Many properties of the crystal may affect the EPD, such as the existence a magnetic or electric dipole moment.

(3) Magnetic Properties– The magnetic moment as well as the magnetic ordering within a NP will be important to understand the morphology of the film as well as other physical properties of the film.

In regards to the suspension, some of the most important characteristics to measure are:

(1) Particle Size Distribution – If one is to create smooth films, it is important that NPs are well dispersed in the suspension: no aggregation or agglomeration occurs. The quality of dispersion can be inferred by measuring the size of the particles and comparing such a measurement to the NP size distribution measured out of suspension.

(2) Mobility – The electrophoretic mobility indicates how the NPs respond to an electric field and give an indication of the charge state of the NPs in the suspension. If the NPs have zero mobility (they are not charged), they will not electrophorese under constant electric fields, thus EPD will not occur. Using the mobility and other properties of the suspension, one can calculate the zeta potential.

Understanding these characteristics about the NPs and the suspensions will facilitate the fabrication and allow meaningful interpretation of the NPMs. In the following sections, tools for characterizing NPs will be introduced and then the use of these tools on iron oxide and cobalt ferrite NPs and suspensions will be demonstrated. By the end of this chapter, all the knowledge necessary to fabricate NPMs will be in place.

4. 1 Techniques for NP Characterization

Four techniques were used to acquire information on the NPs used in this work. Transmission Electron Microscopy (TEM) is a very powerful tool that was used to characterize the NP size distribution, shape, and crystallinity. Powder X-Ray Diffraction (XRD) was mainly utilized to determine NP crystal structure, but could also be used to determine NP size using the Scherrer analysis [80]. Absorption spectroscopy was used to verify crystal structure by comparing observed optical properties to known optical

properties. Finally, vibrating sample magnetometry (VSM) was used to measure magnetic properties of the materials. Example data for each technique is shown in Figure IV.1.

4.1.1 Transmission Electron Microscopy

TEM is a very powerful technique with many capabilities. The ability of TEM to obtain high-resolution, real-space images of NPs will be used. From TEM data one can determine the NP size distribution, shape, if NPs are single crystalline, as well as other NP properties. Another commonly used TEM technique for NP characterization, electron diffraction imaging, can be used to obtain crystallographic information about the NPs, however electron diffraction is not used herein.

In TEM, an electron beam is transmitted through a very thin sample, and the effect of electron interaction with the sample is imaged. The electron beam in a TEM can be created using either field-emission or thermionic emission guns; field emission guns generally provide better imaging results. The beam is focused and filtered using a series of electrostatic and/or magnetic lenses and apertures before forming into a spot on the sample. The beam will interact with the sample, and the part of the beam that transmits through the sample will be used to form an image on a detector (e.g. phosphor screen, charge-coupled device (CCD) camera) with the help of more electrostatic and/or magnetic lenses and apertures. If the image plane of the beam aligns with the location of the detector, a real-space image of the sample is formed. The beam interaction with the sample causes intensity and phase variations within the electron beam that are used to create contrast in TEM images. When imaging at low magnifications, electron absorption within the sample changes the spatial intensity of the beam, creating contrast within the

image. At high magnifications, wave interactions within the beam must be accounted for. The beam interaction with the sample changes the phase of the electron waves. The electron wave interferes with itself, and the complex modulus of the incoming beam is detected. Contrast from this interference is called phase contrast and allows imaging of atomic planes within the sample.

Two TEMs,a Phillips CM20 at Vanderbilt Institute of Nanoscale Science and Engineering (VINSE) and a JEOL JEM2100F at the Center for Functional Nanomaterials (CFN) at Brookhaven National Lab, both operating at 200 keV, were used to collect images of the NPs. Samples were prepared by dispersing the NPs in hexane, and evaporating a small droplet of the NP suspension onto either a copper grid with an amorphous carbon film or a gold grid with a graphene sheet as a support layer [81].

4.1.2 Powder X-ray Diffraction

XRD was used to obtain information about the crystal structure of the NPs. Powder XRD measurements are acquired by impinging an x-ray beam upon a powder of NPs and measuring the elastically scattered beam that reflected off the sample. Ideally, measurements are acquired from a sample of randomly oriented nanocrystals, meaning that every crystal orientation is equally represented. The x-ray beam impinges on the sample causing x-rays to scatter off the NPs. Because of the random crystal orientation, the scattering forms smooth diffraction rings that can be detected using a plate detector. The scattering angle at which the diffraction ring is located corresponds with a reciprocal lattice vector within the nanocrystals. Often data is collected or represented in one dimension as the diffraction intensity as a function of scattering angle (2θ). The intensity of the peaks depends on from which Bragg planes the diffraction occurs as well as the

electron density within the crystal structure. Heavy atoms within the crystal, as they support more electrons, scatter x-rays more strongly than light atoms. The combination of diffraction ring scattering angle and intensity can be used to characterize and to identify samples. An additional property of the diffraction peaks related to NP characterization is the full width at half maximum (FWHM). Using Scherrer analysis, this FWHM can be used to calculate a crystallite size in the NP powder [82]. Scherrer analysis is not implemented herein but introduced because of its common usage.

XRD measurements were obtained using either a Scintag X_1 Powder X-ray Diffractometer using a Cu Kα source (λ=1.5406 Å). The samples were prepared by drying a suspension of NPs dispersed in hexane onto a zero background Si (511) substrate. This zero background substrate was used as it produces no reflections within the angles collected during the XRD measurements.

4.1.3 Visible & Near Infrared Absorption Spectroscopy

Visible and near infrared (Vis-NIR) absorption spectroscopy was conducted by passing a beam of variable frequency light through a NP suspension and measuring the intensity of the beam *versus* frequency that transmits through the sample. Multiple instrument designs exist to perform such measurements, but one common method for obtaining an absorption spectrum is described in the following. Light from a broadband source passes through a monochromator. The monochromator uses a diffraction grating to filter the broadband light to a narrow spectrum of light that is then directed toward the sample. The narrow spectrum of light is associated with a single frequency value. Some of the light at the selected frequency will transmit through the sample, and some of the light will be absorbed via electron excitation within the sample. The intensity of the

transmitted light is detected (typically with a photomultiplier tube or photodiode). Then, by moving the diffraction grating, the monochromator selects a new frequency of light to direct through the sample, and a new transmission intensity value is measured. In this way, an absorption/transmission profile can be measured by plotting the intensity of measured light *versus* the frequency of the impinging light. Measurements must be made on a sample of interest and a reference sample to obtain the absorption data for the sample of interest. The absorption intensity of a sample depends on the outer electron wave functions and energy levels, as absorption as the measured frequences causes excitation of outer electrons. Additionally, the path length and sample concentration is linearly related to the absorption intensity by Beer's Law. The resulting absorption or transmission profile can be correlated with known properties of a material. By performing absorption spectroscopy with vis-NIR wavelengths of light, it is possible to distinguish between two phases of iron oxide (γ-Fe_2O_3 and Fe_3O_4) that could not be distinguished using the XRD data obtained [83].

Absorption measurements were obtained using a Cary 5000 Spectrophotometer at wavelengths of 400 – 1450 nm. Samples were prepared by dispersing the NPs in hexane inside a glass cuvette. Hexane was used as a reference sample.

4.1.4 Vibrating Sample Magnetometry

By vibrating a sample within a pickup coil, it is possible to measure the magnetic moment of said sample. The movement of the sample will cause a change in flux within the coil that induces a voltage across the coil proportional to the magnetic moment of the sample.

Hysteresis measurements of the sample were obtained by measuring the magnetic moment of the sample while controlling an external field around the sample. To perform hysteresis measurements, the sample moment was measured while the external field in increased until the sample became magnetically saturated, then decreased to saturate the sample in the other direction, and then increased again until the sample was saturated.

Field cooled (FC) and zero field cooled (ZFC) measurements can be obtained by measuring the moment of the sample in a constant external magnetic field while the temperature of the sample is controlled. FC measurements were obtained by cooling the sample in an applied magnetic field, then measuring the magnetic moment of the sample as the sample is heated within the same magnetic field in which it was cooled in. ZFC measurements were collected in nearly the same manner, with the only difference being that the sample was cooled under zero applied magnetic field yet heated in a magnetic field.

The hysteresis curve provides many quantitative and qualitative properties of the material; herein the saturation magnetization of the sample and information about the magnetic ordering of the sample were obtained from hysteresis measurements. Hysteresis measurements cannot be used to distinguish between superparamagnetic and paramagnetic ordering within a sample. FC and ZFC measurements were taken to determine magnetic ordering when paramagnetic-like behavior was detected.

VSM measurements were obtained using a Quantum Design Physical Properties Measurement System. Samples were prepared by filling a zero-background PPMS vial with a concentrated suspension of NPs (~90mg/mL) dispersed in hexane and then placing the sample under vacuum to evaporate the solvent. The filling and evaporation were

repeated several times to increase the mass of NPs in the vial (~2mg). The mass of the vials was measured before and after filling, and the mass of the sample was calculated from this. The sample mass will prove important for determining the magnetic moment of individual NPs.

4.2 Iron Oxide NP Synthesis and Characterization

Iron oxide NPs were synthesized by thermal decomposition of an iron oleate precursor in the presence of oleic acid, using procedures modified from Park et al. [84]. The iron oleate precursor was synthesized first by mixing $FeCl_3 \cdot 6H_2O$ (2.17 g, 8.03 mmol) and sodium oleate (7.30 g, 24.0 mmol) in 16 mL of ethanol, 28 mL of hexane, and 12 mL of deionized water. The mixture was heated to 70° C and maintained at this temperature for four hours. The iron oleate in the organic was separated from the biphasic mixture using a separatory funnel. The organic layer was then washed several times with deionized water.

Synthesis of the NPs was performed by mixing the iron oleate (1.6 mmol) with oleic acid (0.8 mmol) and 1-octadecene (10 mL). The solution was degassed under vacuum at 70° C for 30-60 min. The solution was heated at a rate of 3° C/min until the reflux at 320° C. The mixture was refluxed for 45 min and then the heating mantle was removed and the solution allowed to cool at room temperature. The resulting suspension was stored in a dessicator.

Iron oxide NPs were characterized using all the above discussed techniques; the characterizations are shown in Figure IV.1. The measured XRD peaks matched the reflections of a mixture of FeO (wüstite JCPDF #46-1312) and either γ-Fe_2O_3 (maghemite JCPDF #39-1346) or Fe_3O_4 (magnetite JCPDF #19-0629) (Figure IV.1a). In

order to determine which of the two spinel phases were present, absorption spectroscopy was performed the profile matched that of Fe_3O_4 (Figure IV.1b) [83, 85]. TEM images

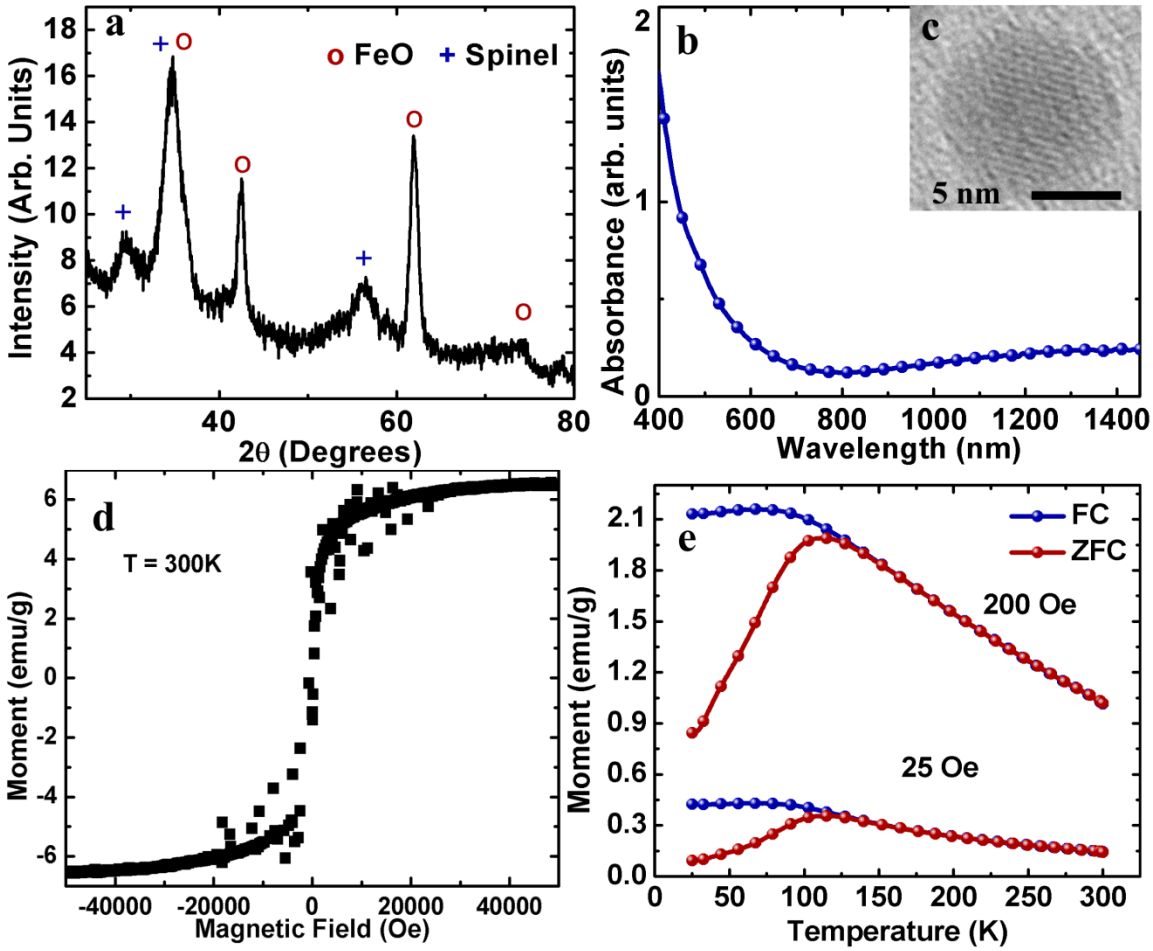

Figure IV.1: Characterization of iron oxide NPs. (a) Powder XRD measurements indicated the presence of FeO and spinel phase iron oxide crystals. (b) The absorption curve indicated the spinel phase was magnetite. (c) TEM images of the NPs indicated the NPs were monodisperse and single crystalline. (d) Magnetic hysteresis curves indicated paramagnetic behavior of the NPs. (e) FC and ZFC measurements confirmed that the NPs were superparamagnetic.

confirmed that the NPs were spherical, monodisperse, and 9.8 ± 0.9 nm in diameter for the sample shown in Figure IV.1c. Also, the lattice planes observed by TEM confirmed that the NPs were single crystalline. Magnetic hysteresis measurements showed

paramagnetic behavior of the NPs, and ZFC and FC measurements indicate that the NPs behave superparamagnetically at room temperature (Figure IV.11d-e). By using the measured saturation magnetization of the sample, the size and shape of the NPs, and the chemical and crystalline nature of the NPs, the magnetic moment of a single, spherical NP (μ_{NP}) can be calculated using

$$\mu_{NP} = \frac{4}{3}\pi r^3 M_s \rho, \qquad \text{(Equation IV.1)}$$

where r is the radius of the particle, ρ is the density of the material, and M_s is the measured saturation magnetization of a sample per unit mass. The magnetic moment of one iron oxide NP was calculated to be ~1800μ_B.

4.3 Cobalt Ferrite NP Synthesis and Characterization

Cobalt ferrite NPs were synthesized by Adriana Mendoza-Garcia using the procedures described by Sun et al and characterized using XRD, TEM, and VSM (Figure IV.2) [33]. XRD measurements confirmed that the cobalt ferrite was in the inverse spinel crystal structure and the lattice parameter was very similar to that of magnetite (8.392 Å). TEM images indicated the NPs were monodisperse, single crystalline, spherical, and 12.2 ± 0.8 nm in diameter. Magnetic hysteresis measurements indicated ferromagnetic behavior of the NPs (Figure IV.2). The magnetic moment per NP was calculated to be ~26000μ_B (Equation IV.1).

4.4 Suspension Preparation

As discussed in Chapter II, the charge state of the suspended NPs is very important when performing EPD. The charge state in nonpolar solvents is highly dependent upon surfactant concentration. Thus, to prepare suspensions for EPD, the

surfactant concentration was controlled by performing cleanings on the suspension. The cleaning also allows one to replace the solvent used for synthesis with the desired solvent for performing EPD.

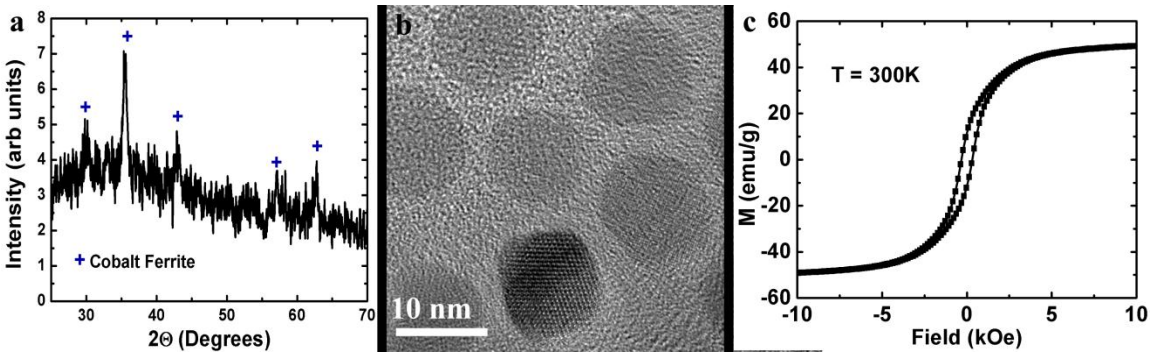

Figure IV.2: Characterization of cobalt ferrite NPs. (a) XRD pattern with peaks corresponding to cobalt ferrite (b) TEM of NPs showing monodisperse, single crystalline NPs. (c) Hysteresis curve of NPs showing ferromagnetic behavior.

Cleaning was performed by mixing a 0.6 mL of the synthesized NP suspension with two polar solvents, first 1 mL of 1-butanol followed by 3 mL of ethanol. Ethanol was not added until the 1-butanol was well mixed with the NP suspension (~1 min). The polar solvents caused the NPs to aggregate and then crash out of the suspension. The crashing out of the NPs was facilitated by centrifugation at ~3000 rcf for 90 minutes. The resulting supernatant from the centrifugation was removed, and the NPs were redispersed in 0.3 mL of hexane. Polar solvent addition, centrifugation, and removal of supernatant was repeated, then the resulting centrifugation pellet was dispersed in 20-60 mL of hexane. This procedure can be repeated multiple times until desired suspension characteristics are obtained. If too much surfactant is removed, the suspension will become unstable.

4.5 Techniques for Suspension Characterization

The charge state of the suspension as well as the dispersion of NPs in suspension are both important in determining how the suspension will behave when performing EPD and in predicting the quality of film that will result from the EPD. Suspension characterizations were performed using a Malvern Zetasizer Nano ZS. This tool has the ability to measure the size distribution of NPs as well as to measure the electrophoretic mobility of the particles in suspension [86].

4.4.1 Hydrodynamic Diameter – Dynamic Light Scattering (DLS)

DLS is a technique where by coherent light is scattered off of suspended materials, and the changes in scattering can be related to particle size. The scattered light is detected as a speckle pattern and is continuously measured. The correlation between two speckle patterns taken at different times is plotted as correlation intensity *versus* time between measurements; this is the correlation function. For smaller particles, the correlation function rapidly decays with time, and for larger particles the decay is slower. This is because smaller particles move more quickly than larger particles due to Brownian motion, thus the speckle pattern changes more quickly. The correlation function is then analyzed to determine the particle size distribution within the sample. The resulting size is a measure of the hydrodynamic diameter of the colloidal particles, which are larger than the NP diameter because the layer of surfactant on the NP surface and the layer of fluid that moves with the particle both contribute to the hydrodynamic size of the particle. Measuring the hydrodynamic diameter can indicate quality of NP dispersion within the suspension by indicating the presence of NP agglomerates and aggregates [87].

4.4.2 Electrophoretic Mobility

Mobility measurements are taken on the same instrument as DLS measurements; however a different technique is used. In Chapter II, the mobility was defined as the

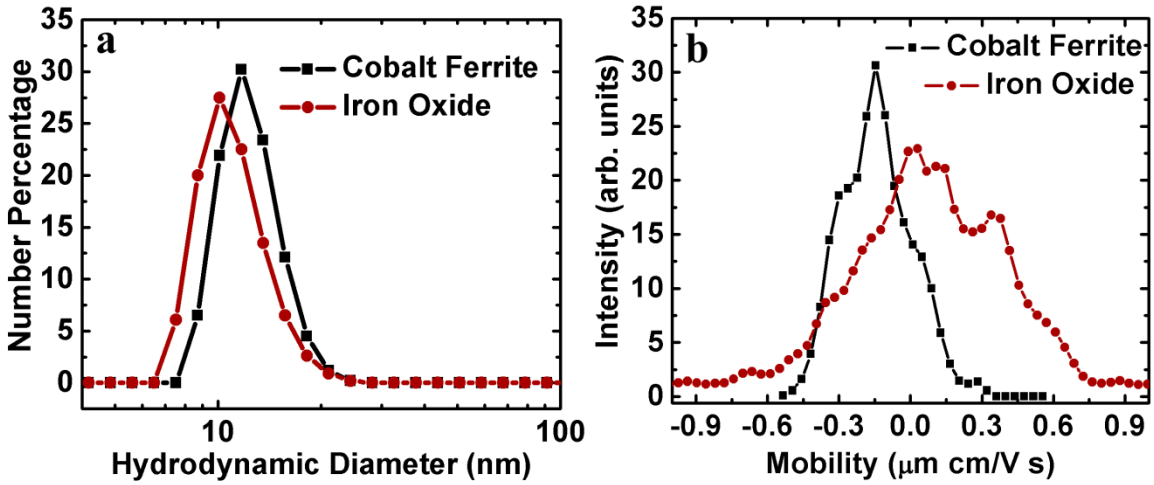

Figure IV.3: Characterization of NP suspensions. (a) DLS measurements of both iron oxide (circles) and cobalt ferrite (squares). The size of the particles measured by DLS is just larger (10.8 nm for iron oxide and 12.3 nm for cobalt ferrite) than the size of the NPs as measured under TEM (9.8 nm for iron oxide and 12.2 nm for cobalt ferrite). From this, it is inferred that the NPs are well dispersed in the suspension. (b) The mobility of iron oxide and cobalt ferrite NP suspensions in hexane. The measurement of iron oxide (circles) displayed a broad spectrum indicating NPs with both positive and negative charges, while the measurement of cobalt ferrite NPs indicated mostly negatively charged NPs.

velocity of a particle per unit electric field. The Zetasizer measures mobility by applying a known electric field and measuring the resulting velocity of particles using laser Doppler velocimetry (LDV). With LDV, the shift in the frequency of scattered light due to the Doppler Effect is used to calculate particle velocity. The mobility is calculated using the applied field and measured velocity.

4.6 Suspension Characterization

Iron oxide and cobalt ferrite suspensions were both characterized by DLS and mobility measurements before performing EPD. Typical results are shown in Figure IV.3. DLS measurements (Figure IV.3a) show the hydrodynamic size of the iron oxide and the cobalt ferrite NPs. Accounting for the surfactant and fluid layer around the NPs, the DLS measurements corresponded well with the size of the NPs as measured by TEM, indicating the NPs were well dispersed.

Mobility measurements for the iron oxide NPs indicated multiple charge states of the NPs existed within the suspension, some NPs held a net negative charge and others a net positive charge (Figure IV.3b). The peaks in Figure IV.3b correspond to individual electron charges on the NPs. The resulting films fabricated under EPD supported the existence of negatively and positively charged NPs, as films formed on both electrodes. The mobility measured for typical cobalt ferrite suspensions indicated that mostly negatively charged particles existed in the suspension. And again, the films fabricated by EPD reflected this mobility distribution.

Understanding the nature of the NPs and the nature of the suspensions is important in the execution of any EPD. In regard to the formation of monolayers, well dispersed suspensions are required in order to form smooth monolayers that can be studied on an individual NP level. Knowledge of the characteristics of the NPs and suspensions is necessary if one is to understand how the NPs behave during EPD and, thus, be able to predict how NP behavior and suspension conditions will affect the resulting film morphology [14].

CHAPTER V

NANOPARTICLES MONOLAYER FILMS

A nanoparticle monolayer (NPM) is simply a film of NPs that has grown in only two dimensions, thus, the film is one NP thick. NPMs are studied for two reasons: NPMs are useful for applications and NPMs can be used to study phenomena and processes occurring during the film fabrication process. Some potential applications of NPMs include surface enhanced Raman scattering coatings, magnetic storage media, and biosensors [1-4]. Some phenomena of the fabrication process that could be studied include NP-substrate interactions, the relationship between NP density and current density during EPD, NP-NP interactions, and other aspects of film growth [19].

NPMs can be fabricated using a variety of techniques. Langmuir-Blodgett is a technique that takes advantage of the affinity of NPs or molecules to collect at the interface between two fluids [17, 88, 89]. Another technique, evaporative self-assembly, has been highly successful in making monolayers of NPs with various lattice structures (e.g. hexagonal close pack, face center cubic, etc.) [9]. Moreover, more complex superlattices can be fabricated using two or more types of NPs and/or sizes of NPs [10-12]. Additionally, spin coating has been successfully used to make monolayers [16]. Lastly, as demonstrated herein, NPMs can be fabricated using EPD.

The history of NPMs formed through EPD using a DC applied field is rather sparse and only few examples exist to our knowledge. The first case appears in the literature in 1993, where well-ordered monolayers of citrate-stabilized gold NPs were

formed [21]. This work was later studied by Zhao et al., and the order was determined to be due to copper ions cross linking the citrate ligands on the NPs [90]. The next instance occurred in 1997 using platinum NPs, where disordered NPMs were created [22]. Beyond this, we have not discovered any literature on NPMs fabricated via EPD.

We have improved upon this dearth of literature on NPMs fabricated via EPD by the introduction of a versatile technique that implements EPD to fabricate NPMs [13, 14, 19, 20, 43]. In this chapter, techniques that can be used to fabricate NPMs in a general way will be discussed. Then, techniques that can be used to analyze NPMs will be introduced. Next, ways to control the monolayers will be demonstrated. Finally, interesting questions raised from analysis of the NPM films will be discussed.

5.1 Fabrication

Using EPD, it has been possible to fabricate NPMs of many different types of NPs, including iron oxide, cobalt ferrite, indium tin oxide (ITO), cadmium selenide, and titanium dioxide, spanning a wide range of magnetic (ferromagnetic, superparamagnetic, diamagnetic), electrical (insulating, conducting, semiconducting), and optical properties (transparent, photoluminescent) (Figure V.1). The key to fabricating all of these NPMs was in obtaining appropriate suspension and deposition conditions.

First, key properties of the suspension for monolayer formation will be discussed. All of the NPMs were fabricated using nonpolar solvents to suspend the NPs. As NPs were surfactant stabilized in nonpolar solvents as opposed to charge stabilized, nonpolar solvents were used to finely tune the concentration of charged NPs, and thus, finely control the film thickness on a submonolayer level.

Surfactant concentration in the suspension was important for fabricating NPMs. Surfactant concentration was reduced by NP cleaning via centrifugation or increased by adding surfactant into the suspension [10]. The suspensions contained a minimal number

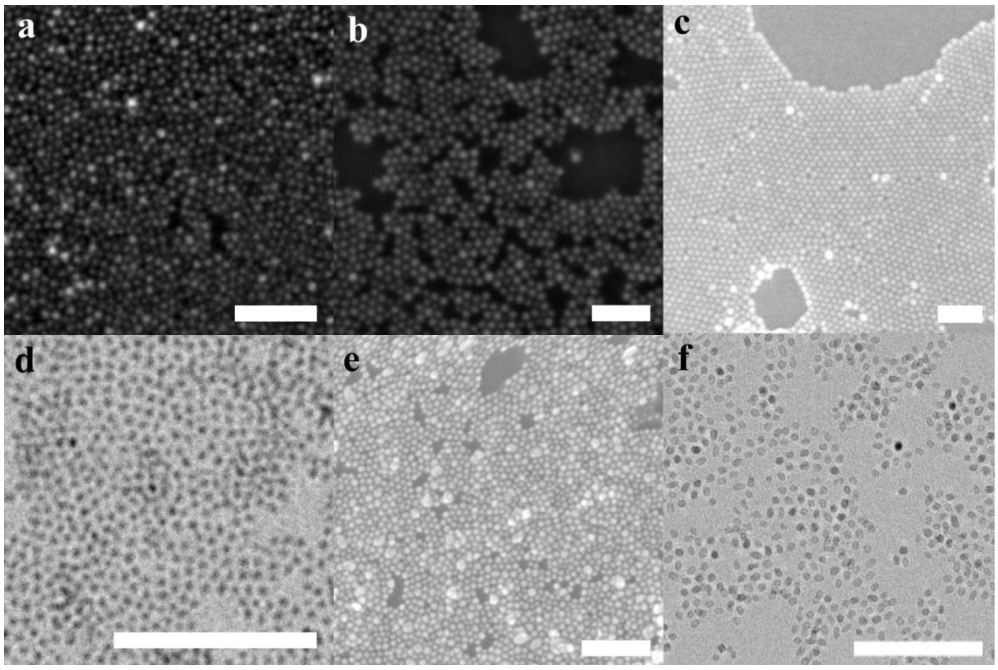

Figure V.1: This figures shows SEM images of (a) ~10 nm iron oxide NPs, (b) ~16 nm iron oxide NPs, (c) cobalt ferrite NPs, a TEM image of (d) CdSe NPs, and a SEM image of (e) ITO NPs, and a TEM image of (f) TiO_2 nanorods [43]. (Scale bars = 100 nm)

of surfactant molecules, as any free surfactant molecules (not attached to a NP) could deposit on the substrate during EPD, leading to undesirable films. Also, excess surfactant can make scanning electron imaging of the sample difficult as surfactants are typically insulators. Removal of too much surfactant will result in NP flocculation, making the suspension unstable or leading to films with high surface roughness. Additionally, as discussed in Chapter II, surfactants help to stabilize charge in nonpolar solvents, resulting in charged NPs. Thus, surfactant concentration can be used to control NP charge. A

balance must be found between too little and too much surfactant to obtain smooth, clean films. Direct measurements of the surfactant concentration were not acquired; instead optimization of surfactant concentration was done empirically by studying the films that resulted from the EPD after various suspension cleanings or addition of surfactant.

The substrate on which the NPs will be deposited is an important factor in NPM fabrication. The geometry of the substrate can affect the morphology of the resulting film. Use of a substrate with a high degree of surface roughness could prevent the formation of smooth NPMs. The roughness will cause inhomogeneous electric fields to emanate from the substrate, potentially causing uneven surface coverage. Surface geometry could also affect NP-substrate interactions, and potentially lead to spatially inhomogeneous interactions that could affect NPM morphology. For the sake of simplicity, atomically flat silicon substrates with a measured surface roughness of 0.16 nm were used herein. Future research could explore the effects of substrate geometry on the morphology of NPMs.

Additionally, the type of substrate used is important in determining if NPs will adhere to the substrate surface. The nature of the bond formed during EPD between a deposited NP and the substrate is still not well understood, but physical and/or chemical bonding can occur in different systems. If the NPs do not adhere, no NPM can be fabricated. Silicon substrates with native oxide has been used herein for detailed studies of NPM morphology, but we have demonstrated that NPMs of iron oxide NPs coated in oleic acid can be fabricated on gold coated silicon, ITO coated glass, and silicon with an oxide of ~300 nm thickness; however, we have observed that the iron oxide NPs will not adhere well to copper substrates.

In addition to determining if NPs will adhere, the substrate choice may also affect when NPs become immobilized on the surface. NPs contacting the substrate surface can be mobile if the NP-substrate interaction is weak. However, if the interaction is strong, the NPs may be immobilized immediately upon contact with the substrate. The NPs deposited on silicon with a native oxide remained mobile during the drying step of EPD.

A typical EPD was performed as follows. First, the suspension was prepared as described in Chapter IV. Two atomically flat silicon wafers with native oxide were cut to size, typically 2-4 cm long and 0.5-2 cm wide. The wafers were heavily doped (either p or n doping), having a sheet resistance of ~5 ohm cm. The electrodes were arranged in parallel plate configuration with a 5 mm gap. The electrodes were dipped into the suspension. A voltage was applied across the electrodes, typically 100-1000 V, for ~1-5 min. The electrodes were extracted slowly (~1 mm/s) from the suspension, and ~1 minute after electrode extraction, the voltage was turned off.

5.2 Analysis of Films

Many techniques exist by which NPMs could be studied; four techniques have been utilized: scanning electron microscopy (SEM), atomic force microscopy (AFM), grazing-incidence small-angle x-ray scattering (GISAXS), and grazing-incidence wide-angle scattering (GIWAXS). The four techniques were chosen as they allow one to study order within the films, measure the number of layers of NPs within films, and measure the orientation of NP crystal structures.

5.2.1 SEM

SEM images are collected by scanning a tightly focused electron beam that is accelerated at ~1-30 kV across the sample. Currently, SEM imaging can achieve

resolutions down to ~1 nm. The beam dwells on one spot causing secondary electrons and backscattered electrons to be emitted around the spot.

Secondary electron emission occurs as the incident beam enters the sample and inelastically scatters off electrons within the sample. Energy is imparted into the electrons within the sample, and some of these electrons will have sufficient kinetic energy normal to the substrate surface to escape the surface. Secondary electrons have less energy than the electrons from the incident beam, and typically electrons of <50 eV are detected. Backscattered electrons, typically thought of as coming from the incident beam, elastically scatter off the sample surface.

Backscattered electrons have high energy, of the same order of magnitude as the incident beam. Heavier atoms have a higher probability to cause electron backscatter, thus backscattered electrons can be used to detect chemical contrast in a sample. Increasing the incident beam voltage will increase the signal of backscattered electrons.

An electron detector, which is typically designed to collect either secondary or backscattered electrons, is used to measure the intensity of electrons emitted from the sample. This measurement corresponds to one pixel intensity value of an image. The beam scans in a rectangular array across the sample surface and dwells at regular intervals. The intensity of electron emission is measured at each dwell spot and a 2D array of intensity values that can be represented by a grayscale image is constructed.

Images of NPMs were taken at high enough magnification (~120,000X) to obtain an image resolution sufficient for discerning individual NPs. By obtaining single NP resolution, regions of a monolayer with and without deposition were easily distinguishable. Those monolayers deposited on conductive substrates could be imaged

directly after EPD. Typically, a 5-10 kV accelerating voltage was used, however higher voltages were used improve image quality when measuring backscatter electrons.

5.2.2 AFM

Layers within the NP films (e.g. monolayer, bilayers, etc.) were distinguishable, to some degree from the SEM imaging due to the difference in conductivity of the layers. However, AFM can provide a more reliable way to determine to which layer a NP belongs. AFM can provide atomic resolutions in all three spatial dimensions when performed under ultra-high vacuum; herein, measurements were acquired under ambient conditions, and resolutions of ~1 nm were obtained.

AFM was operated in tapping mode. In tapping mode, an oscillating cantilever is scanned across a sample surface and topographical information can be obtained about the surface. Tapping mode AFM measurements are acquired using cantilever that is oscillated at a frequency typically just under the resonance of the cantilever (~325 kHz) using a piezoelectric. At the end of the cantilever there exists a sharp tip that is brought close to the surface of the sample until it interacts with the sample. The sample-tip interaction decreases the oscillation amplitude (~100-200 nm) of the cantilever. The decrease in amplitude is detected by the difference in signal received on two photodiodes from a laser reflecting off the end of the cantilever. The amplitude of oscillation should remain fixed as the sample is translated relative to the cantilever using piezoelectric. To maintain the oscillation amplitude, a servo is used to adjust the vertical position of the cantilever above the substrate via piezoelectric actuations. By tracking the lateral and vertical motion of the sample relative to the cantilever, a topographical map of the

surface can be generated. Using this 3-D map, it is possible to discern between the layers of NPs.

AFM was performed using an Agilent 5400. Tips with a force constant of ~40 N/m and a probe radius ~10 nm were used to obtain satisfactory images of the sample.

5.2.3 GISAXS

AFM and SEM both provide high-resolution real-space images of the surface of a film. X-ray scattering can provide complementary information by probing the entire thickness of a material. In particular, GISAXS can provide scattering patterns selectively of either the film surface, or the entire depth of a film. GISAXS is an x-ray scattering technique performed with a grazing-incidence x-ray beam and detects x-rays scattered at small angles. This can be considered the nanoscale analogue of XRD, a well-known technique for determining the atomic structure of crystals from the Bragg reflection of the atomic planes. By detecting the scattered x-rays at small scattering angles (<10°), the length scale of ordering, relative to XRD, can be increased to the nanoscale (up to ~150 nm). By using an incident beam at grazing-incidence (~0.1°), surface sensitivity is possible. By accumulating a two-dimensional scattering pattern in GISAXS, one can probe both ordering in the direction out-of-plane to the substrate and in-plane to the substrate.

GISAXS complements AFM and SEM because it provides information on order between NPs in the direction out of plane of the sample that AFM and SEM cannot easily detect. Additionally, GISAXS provides information over a relatively large region of the sample, on the order of square millimeters while AFM and SEM are typically used to provide images of areas on the order of square microns. This provides statistical sampling

complementary to the local probing of real-space microscopy techniques.

GISAXS was performed at the National Synchrotron Light Source (NSLS) at the X9 beamline. Incidence angles from 0.05° – 0.3° were used, with an incidence agnle of 0.01° typically providing the best signal, and data collection times were from 2-60 seconds.

5.2.4 Grazing-Incidence Wide-Angle X-ray Scattering (GIWAXS)

GIWAXS is very similar to GISAXS, with the main difference being that x-rays scattering at wide-angle (~10°-35°) are measured—instead of small-angles—and the detector is placed much closer to the sample. GIWAXS provides similar surface sensitivity and statistical averaging to GISAXS, however GIWAXS is used to detect atomic scale ordering within the films. Using a 2-dimensional detector, it is possible to observe preferential alignment of nanocrystals by observing variations in x-ray intensity within a diffraction ring. GIWAXS was also performed at the National Synchrotron Light Source (NSLS) at the X9 beamline.

5.3 Monolayer Film Growth

In the following, how the density of monolayers can be controlled by varying deposition time, voltage, and suspension concentration is discussed. Then, how NPs arrange within the NPMs is inspected. From the arrangement of NPs, it was possible to infer some facts about the deposition process and to raise important questions about the ordering process.

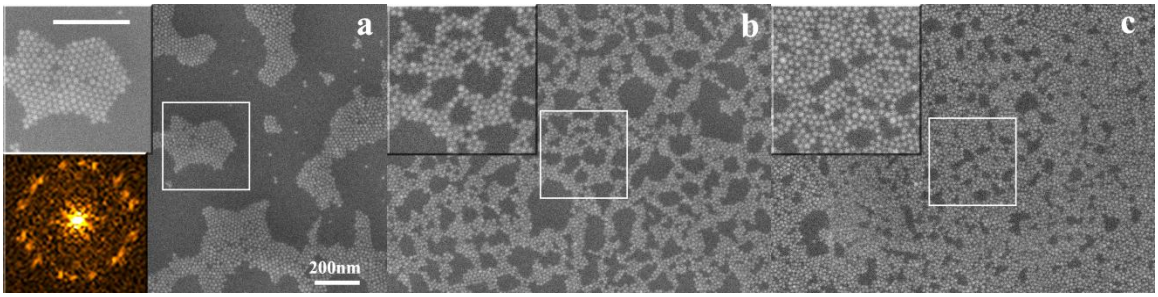

Figure V.2: Chronological growth of a single monolayer. (a) After 20 s of deposition, clusters form into hexagonally packed domains. The upper inset shows a magnified section of the image, and the lower inset shows a Fourier transform of the upper inset. From the lower inset, three hexagonally packed domains were identified by the ring composed of 18 dots. (b) After 97 s, the film grew into a network by merging of clusters. (c) After 180 s, particles deposited within voids of network to form a nearly complete monolayer; no three-dimensional growth was observed. (Inset scale bar: 200 nm – scale bars are the same in each image; suspension concentration = 1 mg/mL) (Reprinted with permission from Krejci et al [19]. Copyright 2011 American Chemical Society)

5.3.1 Controlling Monolayer Density

We define the monolayer density as a measure of the number of NPs per unit area on the substrate surface. Control of monolayer density using deposition time, particle concentration, and deposition voltage has been demonstrated. By controlling the monolayer density, it is possible to obtain information about the kinetics of film formation and, thus, obtain better control over the films.

First, monolayer density *versus* deposition time was studied by inserting long electrode into suspension, turning on a 500 V potential, then partially extracting electrodes by 3 mm at four different times during the deposition (~20 s, 50 s, 100 s, 140 s). Finally, at 180 s the electrodes were completely extracted. The potential remained on for 3 min after extraction to facilitate drying of the solvent. This stepwise extraction resulted in a film containing five distinct regions that differed only by the amount of time said region remained in the NP solution. The chronology of growth of the film is depicted

in Figure V.2, showing representative regions of the film at three stages of the monolayer formation. As expected, increasing deposition time increased monolayer density.

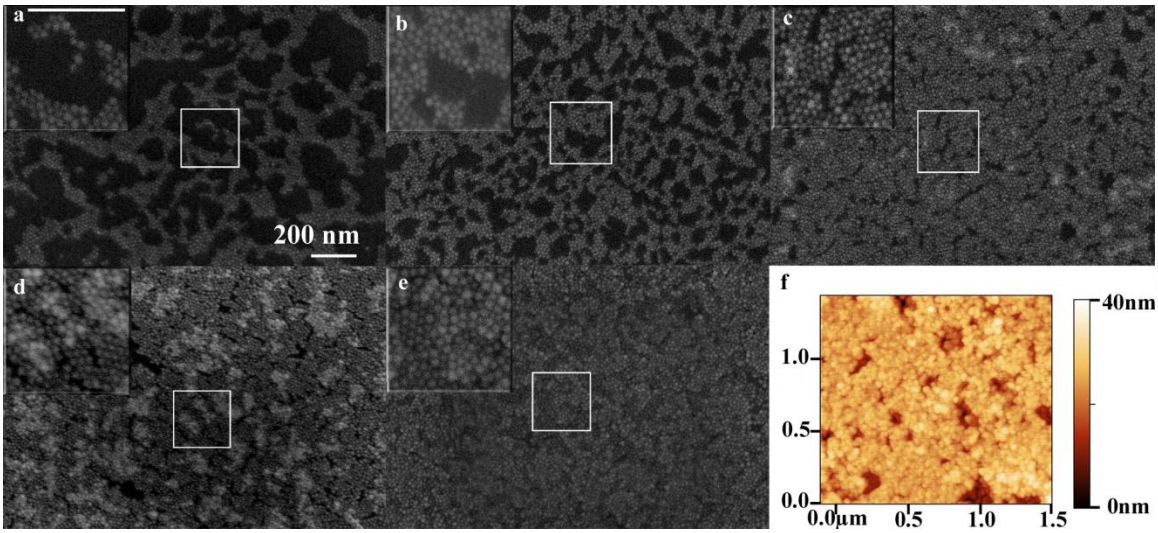

Figure V.3: Chronology showing growth of a multilayer film. (a) Initial growth of monolayer. (b) Clusters began to network within the monolayer. (c) Monolayer growth nearly completed and bilayer (brighter regions) growth had begun. (d) Bilayer particles packed hexagonally, voids in the underlying monolayer appear to have inhibited the network of the bilayer. (e) Bilayer growth appeared to have been suppressed until the filling in of larger voids in the monolayer was accomplished. (f) AFM image of the same region of film depicted in e. The bilayer appeared to be nearly complete. The first NPs of the trilayer had deposited onto the film. Collectively, these images support a monolayer-by-monolayer film formation process. (Scale bar and inset scale bar for images a-e = 200 nm; suspension concentration, ~1mg/mL) (Reprinted with permission from Krejci et al [19]. Copyright 2011 American Chemical Society)

Next, the effects of concentration of charged NPs were studied. Concentrations of charged NPs can be tuned by changing surfactant concentration and also by depletion of charged NPs by performance of EPD in a suspension. Figure V.2 and Figure V.3 show films deposited in the same suspension, but the film in Figure V.2 was formed after depleting the NP suspension. In Figure V.3, the film from the suspension before depletion is shown after 10 s, 32 s, 64 s, 100 s and 180 s of deposition. Increased deposition time

resulted in increased deposition density; however, the increased concentration resulted in a film growth rate that was substantially larger than in the lower concentration sample. Additionally, at the final two time steps a multilayered film was observed. Figure V.3f shows an AFM of this region of the film. Highlighted in this image are the exposed, underlying monolayer, a nearly complete bilayer, and the very beginning of a trilayer. Step height measurements between layers indicated a height of just less than one particle diameter as expected from a hexagonalclose pack or face centered cubic pack in three dimensions. Interestingly, the trilayer did not appear to form until the underlying bilayer had nearly completed. This indicated that the multilayer film grew in a monolayer-by-monolayer fashion.

Finally, control of film density is demonstrated via electric field strength (Figure V.4). Field strength was controlled by varying the applied voltage in a logarithmic fashion. Iron oxide NPs were deposited at long deposition times (10 min), so that film growth had essentially ceased before extracting the electrodes. To verify this, NPs were deposited for ~5 min and ~10 min at each voltage and a marginal change in monolayer density was observed at the two times. From Figure V.4, the lower voltages were observed to lead to less dense deposition. Potentials above 31.6 V appeared to have little effect on the film density. Voltage can be precisely controlled, making this method potentially very useful for finely controlling the film density.

5.3.2 Discussion of Film Growth

Figure V.2 shows that the monolayer density can be increased by increasing deposition time, but a closer inspection of the figure brings to light some interesting

questions about the deposition process. Figure V.2a shows that the NPs prefer to deposit in clusters. Within the clusters, hexagonal packing between NPs

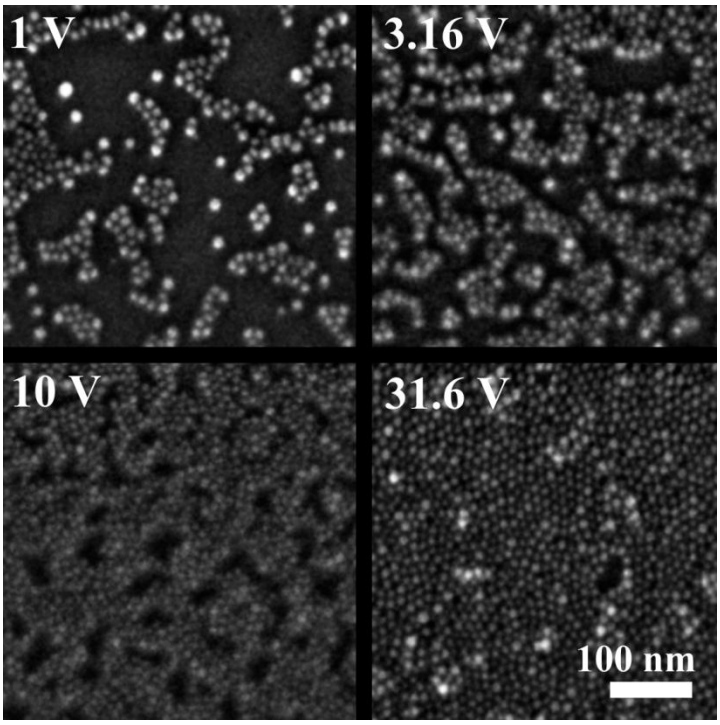

Figure V.4: Varying voltage can be used to vary the monolayer density. Increasing the voltage increases density of iron oxide NPMs. Above 31.6 V, film density is only slightly altered. Voltage can be precisely controlled making this a powerful tool for controlling film density.

was observed. The hexagonal arrangement was made conspicuous when a Fourier transform of the image was taken; the lower inset of Figure V.2a is a Fourier transform of the upper inset of Figure V.2a. The Fourier transform revealed the presence of three distinct domains of hexagonally packed particles represented by three sets of six, equally-spaced first order peaks in the transform. Moving on to the longer deposition time shown in Figure V.2b, it was observed that the once isolated clusters had become connected,

forming a continuous network of NPs. Finally, in Figure V.2c increase in the monolayer density was observed, yet no bilayer growth had occurred.

This detailed observation of Figure V.2 provokes a few questions about the monolayer growth. For example, why did the NPs not stack on one another until the monolayer had nearly completed? The deposition process used atomically flat substrates, thus the electric field that emanated from the substrate was locally uniform. If the particles then simply travelled along these parallel field lines, one would have observed a random distribution of NPs on the surface. Surely some particles would have stacked in this case, yet stacking was not observed. One possible explanation for this could be that NPs were attracted to the edge of the already deposited NP network because of field gradients produced at the film edges. Alternatively, the NPs that had deposited may have remained mobile, allowing incoming NPs to burrow into the underlying film.

Additionally, one may ask: what made the particles form clusters? Also, what made the particles order hexagonally? The existence of clusters and hexagonal ordering implies that some lateral force must have existed that pulled the NPs toward one another. When did this force act to draw the particles together? The rest of this dissertation will focus on understanding what causes NPs to order when deposited via EPD using the techniques herein.

CHAPTER VI

ORDERING IN MONOLAYERS

As discussed in the introduction, by controlling the order within an array of NPs it is possible to tune the properties of said array. Many research groups have investigated making ordered arrays, and some have quantitatively analyzed such order [91, 92]. Quantifying order is useful for many reasons. Quantifying order within a NP array allows one to measure how changes in order can affect other physical properties of the array. Additionally, quantifying order can aid in the determination of a mechanism that generates order within a NP array. It is our goal to determine the mechanisms that generated order, so that future investigations may focus on controlling order. In this chapter, possible mechanisms that may generate order within NPMs fabricated using EPD are discussed and then techniques that can be used to measure this order are introduced.

6.1 Mechanisms to Generate Ordering During EPD

Locally ordered arrays of NPs can be made quite easily and often occur without intention. For example, a common method of preparing NPs for imaging involves simply evaporating a suspension of these NPs on a surface. During the evaporation process, the NPs can cluster on the surface of the liquid and form ordered structures. The liquid surface shrinks as the solvent dries, compressing the NPs together. A technique called evaporative self-assembly utilizes this effect and can be used to form large, ordered arrays of NPs. In another technique, order arrays of NPs are generated by collecting NPs

onto the surface of a liquid and forcing the NPs together using a moveable barrier. The NPs can then be transferred to a substrate using a Langmuir-Blodgett trough.

In these techniques, the NPs are subjected to boundary constraints that force the particles together. To minimize the volume occupied, the NPs will often form ordered structures. For spheres, the densest packing structure is hexagonal packing, which is often observed in arrays of NPs. Other packing structures can be formed due to interactions between NPs such as magnetic dipolar interactions [34]. However, the application of boundary constraints to the NP system is the driving mechanism behind long range order.

When performing EPD, NPs are not subjected to such strong boundary conditions as in other techniques. During EPD, NPs are only constrained in one dimension and can freely move in two lateral dimensions parallel to the substrate. Moreover, when performing EPD on atomically flat substrates in nonpolar solvents, the applied electric field does not introduce lateral motion to the NPs near the electrode surface. The electric field emanates perpendicular to the electrodes, causing the NPs near the electrode surface to electrophorese in a direction perpendicular to the electrodes. In the absence of lateral motion, one would expect the location at which the NPs deposit to be random. Yet, the NPs did not form a random pattern on the substrate in the previously discussed experiments and were, in fact, hexagonally packed on a local scale. Such packing implies the existence of a lateral force that drew the particles together. By determining what lateral forces existed and discovering the mechanism that generated the observed order within the NPMs, one could begin to manipulate such order.

Four likely mechanisms that could generate order within NPMs fabricated via EPD have been identified:

1. Dipolar NP-NP Interactions
2. Van der Waals NP-NP Interactions
3. Ligand-Ligand Interactions
4. Capillary Forces During Drying

These four mechanisms were identified because each has been shown in previous literature to generate ordered NP arrays and all four potentially introduce lateral forces into the systems studied [93]. Many other mechanisms exist that could generate or influence order within the NPMs. For example, models of EPD that include Brownian motion have shown that the Brownian motion can affect the ordering within films; Brownian motion may play a contributing role to the degree of order observed in NPMs herein, but it is unlikely a mechanism that could generate order [94]. Particle-substrate effects are also very important for NP ordering and could be controlled to engender order [93].

Importantly, the mechanism that generates order will vary from one system to another due to differences in deposition conditions, such as types of NPs and solvent used, chemistry of the electrode surface, electrode geometry, etc. For example, magnetic interactions between NPs could generate order in one system, while capillary forces could be the mechanism in a system of nonmagnetic NPs. Or, if polar solvents are employed, order could be generated by electrohydrodynamic flows [53]. When selecting the four mechanisms above, it was important to consider the nature of the EPD system. From the nature of EPD performed in this work (notably, the use of nonpolar solvents and magnetic NPs) we believe one or more of the four mechanisms listed above generated order within the NPMs studied herein.

6.1.1 Dipolar Interactions

Dipolar interactions can be due to magnetic dipoles or electric dipoles. Here magnetic dipolar interactions are the focus. Electric dipolar interactions can be equally effective at generating order and can even result from dipoles induced by the fields applied during EPD.

Magnetic dipolar interactions have been shown to affect ordering within arrays of NPs [34]. The dipolar interaction energy is given by

$$E_{dipole} = \mu_0 \frac{\vec{m}_1 \bullet \vec{m}_2 - 3(\vec{m}_1 \bullet \hat{n})(\vec{m}_2 \bullet \hat{n})}{4\pi|x_1 - x_2|^3} \qquad \text{(Equation VI.1)}$$

where μ_0 is the magnetic permeability of free space, $\vec{m}_{1,2}$ are the magnetic moments of the NPs, $x_{1,2}$ are their locations, and $\hat{n}$ is a unit vector pointing along the direction that joins the two NPs [95]. This equation expresses that the separation distance between NPs, the moment of NPs, and the orientation of the moments can all alter the interaction energy between dipoles. Dipolar interactions will only be present in systems containing NPs with a dipole moment.

6.1.2 van der Waals Interactions

Van der Waals interactions (vdWI) between two NPs are calculated by

$$E_{vdW} = -\frac{A_{pop}}{12}\left\{\frac{d^2}{r^2} + \frac{d^2}{r^2 - d^2} + 2\ln\left(\frac{r^2 - d^2}{r^2}\right)\right\} \qquad \text{(Equation VI.2)}$$

where A_{pop}, d, and r are the Hamaker constant, particle diameter, and center-to-center spacing between particles, respectively [93, 96]. The Hamaker constant depends on the properties of the two interacting NPs as well as the medium separating them. For example, for interactions between two magnetite NPs in hexane, a Hamaker constant of 137 meV has been calculated [97]. vdWI are most important near the electrode during

EPD due to the increase in NP concentration that decreases the average distance between NPs. Evidence that vdWI play a role in NP assembly has been shown in work by Pileni, Talapin, and Morimoto [34, 98, 99]. In these studies, vdWI are shown to affect ordering, but only partially explain the generation of order. vdWI will be present in all systems. vdWI and dipolar interaction energies both strongly depend on the separation distance between NPs. When the separation distance is small, vdWI tend to dominate; when separation distance increases, the magnetic interactions will dominate.

6.1.3 Ligand-Ligand Interactions

In one of the few publications on NPMs formed via EPD, ordering was shown to occur due to the crosslinking of surface ligands with the help of free copper ions in suspension [21, 90]. Ligand-ligand interactions present a powerful way to control order within a system. Work has also been done on fabricating ordered NP arrays by incorporating DNA into the surfactant that coats the NPs. This techniques allows for very controlled crosslinking between NP ligands [8]. In the NP systems used herein, crosslinking between the carbon-carbon double bond present in both oleic acid or oleylamine surfactant molecules coating the NPs could generate order [100]. Such crosslinking can be facilitated by the presence of oxygen, light, and electrochemical processes. If cross-linking occurs, the NPs will be bound by an interaction stronger than van der Waals and magnetic dipolar interactions, however, some activation energy is required for such crosslinking to occur.

6.1.4 Capillary Forces during Drying

Finally, capillary forces during substrate drying could draw the particles together. For neighboring, spherical particles, capillary forces can be calculated by

$$F = 2\pi d\gamma\cos(\varphi) \qquad \text{(Equation VI.3)}$$

where d is the particle diameter, γ is the surface tension of the liquid, and φ is the contact angle of the solvent meniscus [101]. When the film is extracted from the suspension, some residual solvent remains. As this residual solvent dries, it may draw particles toward one another via capillary forces and generate order in the NPMs. Capillary forces tend to be stronger than magnetic and van der Waals forces.

6.2 Measuring Order

Having identified potential mechanisms that could generate order, the next step is to study them. In extreme instances where order is dramatically enhanced or reduced, the change in order may be obvious from visual inspection of images of the films that contain individual NP resolution. A quantitative analysis can permit one to precisely measure the degree of order within a film and thus determine the dependence of order on the various controllable conditions of the EPD process.

To quantify the order in these NPMs, four spatial statistical measures and one x-ray scattering technique are used. The four statistical measures require as input the locations of each NP within a region of the film. In some cases it is also important to locate voids within the films. These data can be extracted from SEM images of the films. For a detailed description on how to locate the NPs and on how to locate the voids within the film using the SEM images, see the Appendix.

6.2.1 Measures of Order Using Spatial Statistics

Four measures of order based on spatial statistics have been utilized to quantify order within NPMs. First, the Voronoi-cell edge-fraction distribution and entropy are

discussed. The distribution relates order to the number of nearest neighbors surrounding each NP. The discussion of this measure of order is prefaced by an introduction to Voronoi tessellations. Voronoi tessellations will be helpful in measuring order using three of the four measures introduced here. Next, two order measures are examined together: the local bond-orientational order parameter and the translational order parameter. Then the final statistical measure used herein, the anisotropy complex-order parameter, is considered. This parameter is used to detect preferential direction in bonding between nearest neighbor NPs, where the term "*bond*" simply refers to the radial vector that connects neighboring NPs.

6.2.1.1 Voronoi Tessellations and the Voronoi-Cell Edge-Fraction Distribution and Entropy

Voronoi tessellations have a long history of use in a variety of fields, including anthropology, astronomy, biology, chemistry, computational geometry, physics, and statistics, among others [102-105]. A Voronoi tessellation, as defined by Okabe, is an association, "given a set of two or more but a finite number of distinct points in the Euclidean plane [of] all locations in that space with the closest member(s) of the point set with respect to the Euclidean distance" [105]. The Voronoi tessellation has many uses:

(1) First, the Voronoi tessellation is itself a visual tool that can highlight geometric patterns.

(2) The fraction of Voronoi cells with n-sides can be measured, resulting in a 1D set of data we name the Voronoi-cell edge-fraction distribution. If order is present, the distribution will make apparent the symmetry of the

such order (in 2D, either 4-fold or 6-fold symmetry can exist as a space filling symmetry).

(3) Informational entropy can be calculated from the 1D Voronoi-cell edge-fraction distribution dataset, giving a 0D data.

(4) The tessellation provides one way to define the concept of nearest neighbors, that is, nearest neighbors have one Voronoi edge in common. This is the definition used in our calculations. Another common nearest neighbor definition is that of two particles that are within a distance of 1.2 times the radius of the particle. The latter definition fails when the two particles are of different size; however the Voronoi neighbor method remains rigorous [14, 102, 105, 106].

(5) The Voronoi tessellation is used to discover which particles are at a boundary of a void or a boundary of the image. These particles often create undesired effects in the measures of order, thus the tessellation provides a means by which these particles can be removed from the calculations.

(6) The average particle-particle spacing between nearest neighbors for well-packed particles can be calculated using the Voronoi tessellation [107].

(7) Bond angles can be measured by using Voronoi-cell edges.

(8) The Voronoi tessellation allows one to quantitatively define a hexagonally packed particle as discussed in Section 6.2.1.3.

The topology of the Voronoi tessellation can be easily found using the MATLAB function *voronoin.* When given a list of positions in two dimensions, this function outputs

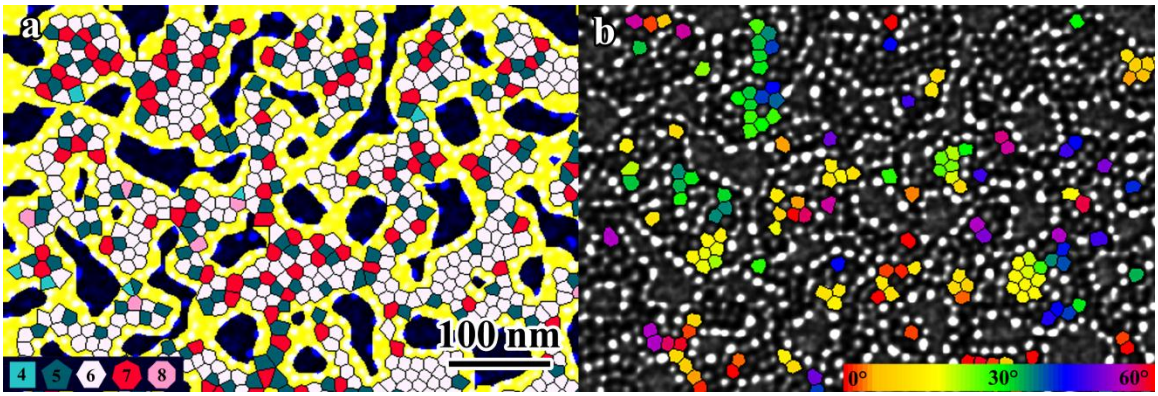

Figure VI.1: (a) shows a Voronoi tessellation representing a NP monolayer. The yellow (light) background represents regions where edge particles existed, the blue (dark) background represents regions of where voids existed. (b) Those Voronoi cells that satisfied the two selection criteria are shown. These cells will be used for calculation of the complex anisotropy order-parameter. The cells are color coded, with color depicting the average direction of the bond angle for all six bonds associated with the cell.

the associated location of Voronoi vertices and outputs for each cell all the vertices that belong to said cell. Using this data, a visualization of the Voronoi tessellation can be constructed (Figure VI.1). Before any statistical measurement were made herein, the Voronoi topology data was utilized in conjunction with segmented images to identify particles that lay on the edge of the film (either at the edge of the image or next to a void). NPs at the edge of the image could be identified either by having any Voronoi vertices at $\pm\infty$ or by having any Voronoi vertex that lay within a void.

Using the Voronoi diagram, a distribution of the fraction of Voronoi cells with n, for $n = 3-9$, edges was plotted. In order to determine the statistical significance of such a plot, the data were collected for multiple images selected from random regions of the film, and the average value and standard deviation of the edge-fractions was used. The distribution shown in Figure VI.2 was created by averaging over at least five images. From Figure VI.2, a peak at n=6 indicated the hexagonal nature of the NP packing,

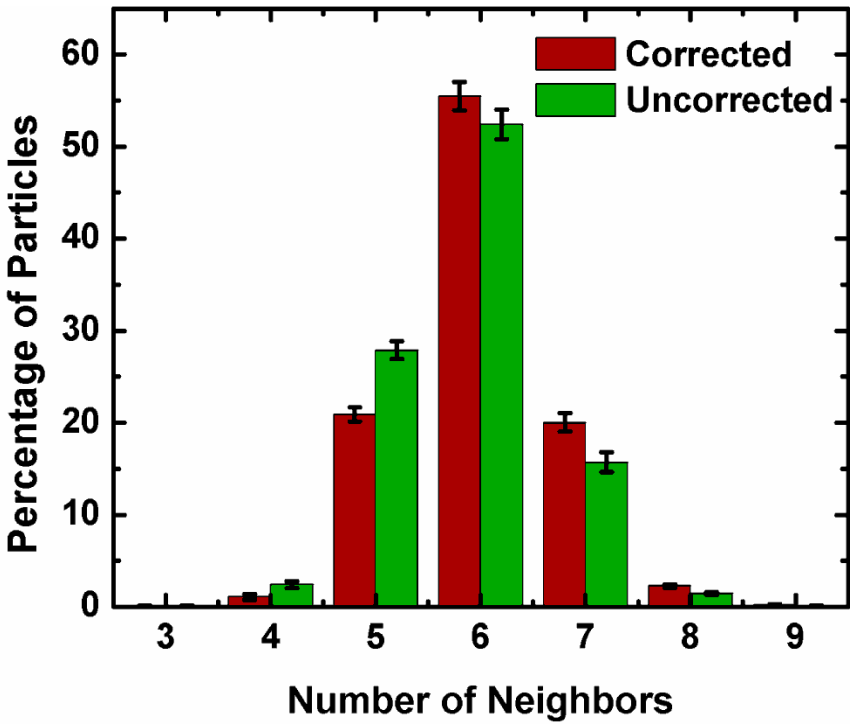

Figure VI.2: The Voronoi-cell edge-fraction distribution, which displays the percentage of NPs represented by a Voronoi cell with n edges. The green bars show the data obtained directly from a Voronoi tessellation. The red bars show the data corrected for edge effects.

agreeing with visual inspection of the SEM. A defect-free, hexagonally-packed film would have a 100% peak at n=6. Nonzero values for any other value for n represent defects within the film.

An interesting feature of Figure VI.2 is that the peak at n=5 is much higher than the peak at $n = 7$ for the uncorrected data. Two types of defects within the bulk of a two-dimensional film of hexagonally packed spheres generally exist: either one NP having five nearest neighbors and another having seven (5-7 pairing) or one NP with eight neighbors and two NPs with five neighbors (5-8-5 pairing). Both types of defects result in an average number of neighbors equal to six [108]. If one assumes that these pairings are the only source of defects, it makes sense then that the peak at $n = 5$ is greater than the

peak at $n = 7$. However, there is an excess of peaks at 5 as the average number of neighbors from the collected data is less than six. Possibly, NPs near the boundary caused the discrepancy. Such NPs introduce edge defects into the data.

Defects can occur near the boundary of the film that do not follow the 5-7 or 5-8-5 pairing discussed above. NPs near the film boundary may have defects due to the absence of NPs on the boundary of the film, resulting in preferentially decreased number of neighbors. While NPs at the edge of the film have been removed, not all NPs affected by the boundary have been removed. It is empirically observed that increasing the edge length of the film will result in more NPs with fewer than six nearest neighbors and less NPs with six or more neighbors, implying that edge effects were the source of defects (Figure VI.3).

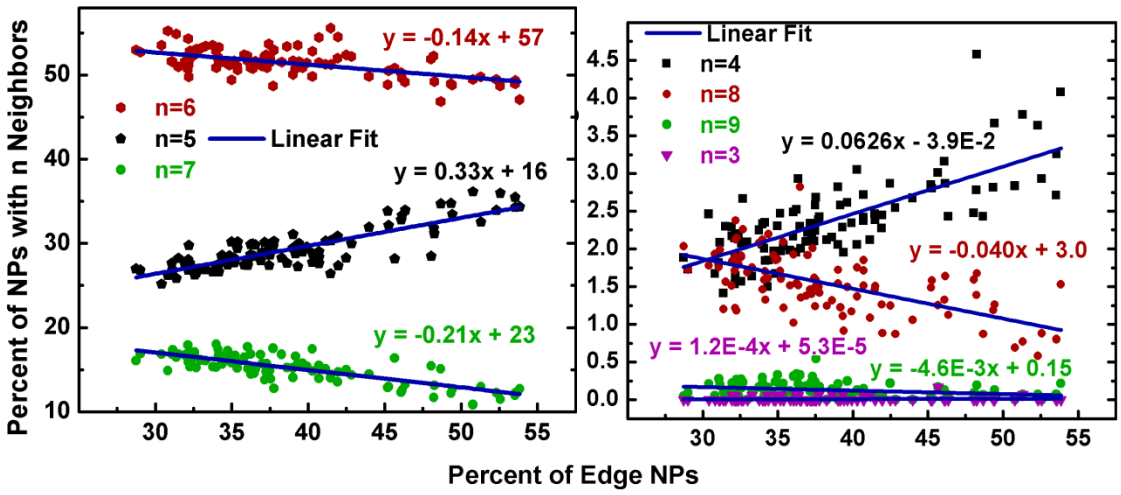

Figure VI.3: The graphs above show a linear relationship between the percent of NPs with n=3-9 neighbors *versus* the percent of NPs located on the edge of the film for data collected from 100+ SEM images of NP films. By extrapolating the data back to zero for the percent of edge NPs, edge effects can be removed and a more reliable measure of entropy from the Voronoi-cell edge-fraction distribution can be obtained.

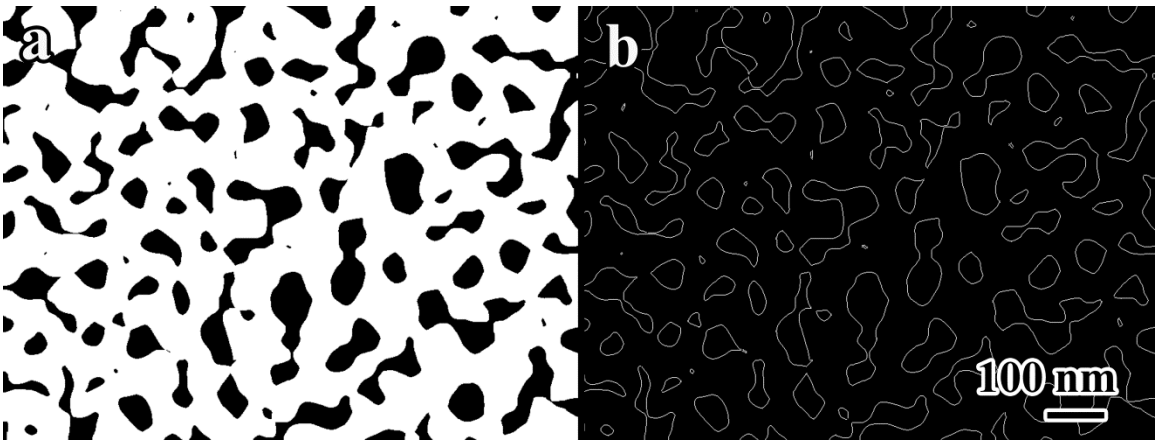

Figure VI.4: (a) shows the segmented image that identified voids within the film. (b) is the derivative of (a), calculated using the Prewitt operator. By counting the percentage of pixels in (b) that are white and dividing by the total number of pixels in the image, we calculated the percent of edge pixels. This value depend on the resolution of the image, so all images in such analysis should be collected in the same way.

The percent of edge pixels in 100+ segmented images that were used for locating voids (see Appendix for image segmentation) was acquired by taking the derivative based on the Prewitt operator and used as a metric for the length of the edge (Figure VI.4). As the segmented image was a binary image, the derivative was also a binary image with high values at the edge of the segmentation and low values everywhere else. Figure VI.3 shows that NPs with less than six neighbors had a positive correlation with the number of edge pixels, while those with six or more neighbors had a negative correlation. Thus, it was inferred that the increased number of NPs with neighbors less than six was an edge effect and separation of this edge effect from other naturally occurring defects was attempted. The correlation was removed by fitting the data to a line extrapolating the data back to the x=0 axis on the graph. Because the percent of NPs with n neighbors must add up to one hundred for each image, the extrapolation was done using one half of the slope from the linear fit. By correcting the data in this manner, the mean number of neighbors

per particle became remarkably close to six, thus the imbalance of particles with less than six neighbors was eliminated (Figure VI.2).

Finally, this 1-dimensional Voronoi distribution data set can be simplified into a 0-dimensional data set by calculating the informational entropy, S, of the distribution using:

$$S = -\sum_{i=3}^{9} p_i \ln p_i \,, \qquad \text{(Equation VI.4)}$$

where p_i is the probability of a Voronoi cell having i edges, and i ranges from three, which is the smallest number of edges a closed Voronoi cell can have, and nine, above which nearly zero Voronoi cells exist. [14, 109, 110]. This entropy measurement allows one to directly compare Voronoi-cell edge-fraction distributions between many samples. Additionally, the measured entropy value could be compared to, for example, the entropy obtained from a random distribution of points or a more sophisticated model that accounts for particle interactions.

6.2.1.2 Order-Parameters – Local Bond-Orientational Order-Parameter and Translational Order-Parameter

An order parameter is a measure of order varying between zero, indicating complete disorder, and one, indicating perfect order. Having a limited number scale for the parameter makes it simple to compare data from many different experiments. Works by Torquato, Truskett, and Kansal advocate the use of order-parameters and have created order-parameter spaces that act as phase diagrams for particle packing, showing fluid, glassy, and crystalline ordering regimes [111-114].

The Voronoi tessellation is utilized when calculating the bond-orientational order parameter. The Voronoi tessellation allows one to filter out all edge NPs. Then, the Voronoi edges are used to calculate the bond directions for each cell. The local bond-orientational order parameter, $\psi_{\xi,local}$, was calculated for each cell using

$$\psi_{\xi,local} = \frac{1}{N_n}\sum_{j=1}^{N_n} e^{i\xi\theta_{jn}}, \qquad \text{(Equation VI.5)}$$

where ξ=6 is the periodicity, which represents hexagonal, close packing, θ_{jn} is the angle of bond j for Voronoi cell n measured relative to an arbitrary, fixed axis, and N_n is the number of edges of cell n [115]. An example histogram was plotted of the $\psi_{6,local}$ values for each cell taken from a single SEM image (Figure VI.5a). The mean value of $\psi_{6,local}$, calculated by averaging the $\psi_{6,local}$ value for each bond between NPs, can be used to compare order between multiple samples.

The translational order parameter τ, is discussed in conjunction with the bond-orientational order-parameter because the combination of the two functions can be used to determine the order regime of the film.

$$\tau = \frac{1}{r_c}\int_0^{r_c} |g(r) - 1| dr, \qquad \text{(Equation VI.6)}$$

where $g(r)$ is the pair correlation function (or radial distribution function) in 2D and r_c is the maximum radius measured in the pair correlation function [112]. The calculation of the translational order parameter does not require inputting a known periodicity, ξ, for the packing. Additionally, the presence of voids does not affect the measure due to a normalization by the density of particles when calculating $g(r)$. An example plot of $g(r)$

is shown in Figure VI.5b. At high values of r, peaks become less intense and the curve settles near $g(r) = 1$ due to the normalization factor. The translational order parameter is, in essence, designed to calculate how much the pair correlation function deviates from unity.

6.2.1.3 Bond Anisotropy Complex-Order-Parameter

The *local* bond-orientational order-parameter has been discussed, but it is also useful to know something about the *global* direction of bonds in the film. The anisotropy complex order-parameter is specifically designed to detect if a preferential bond direction (anisotropy) exists within the entire film. This anisotropy can be visualized as the angular orientation of hexagonal Voronoi cells. Importantly, the anisotropy of interest is not anisotropy in the shape of the Voronoi cell, but anisotropy in the orientation of the cell. Such anisotropy could be introduced to a physical system through a variety of mechanisms (unidirectional magnetic fields, non-radial fluid flow, anisotropic geometries

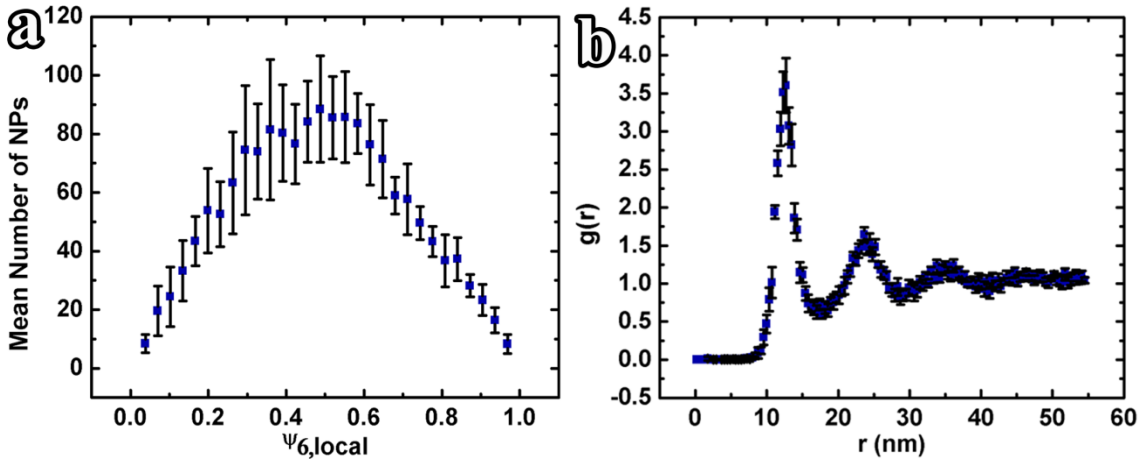

Figure VI.5: (a) shows a typical histogram of $\psi_{6,local}$ using data acquired from SEM images; (b) shows a typical $g(r)$ curve measured from the same data.

in the system, etc.). Creating NPs films in the presence of such anisotropy may cause the NP-NP bonds to prefer to orient in a specific direction.

The anisotropy complex-order-parameter, $\Psi_{an}e^{i\Theta_{an}}$, was calculated similarly to $\psi_{6,local}$,

$$\psi_{jn}^{\xi} = e^{i\xi\theta_{jn}}$$

$$\psi_{\xi,an} = \frac{1}{N_\xi}\sum_{j=1}^{N_\xi}\sum_{n=1}^{\xi}\frac{\psi_{jn}^{\xi}}{\xi} = \Psi_{an}e^{i\Theta_{an}}, \qquad \text{(Equation VI.7)}$$

$$\Psi_{an} = \left\|\psi_{6,an}\right\|, \qquad \text{(Equation VI.8)}$$

$$\Theta_{an} = \arctan\left[\frac{Im\left(\psi_{6,an}\right)}{Re\left(\psi_{6,an}\right)}\right], \qquad \text{(Equation VI.9)}$$

where Θ_{an} is used to detect the direction of anisotropy and Ψ_{an} measures the magnitude of anisotropy [113].

The equations as described above are equivalent to another order-parameter called the global bond-orientation order-parameter [116]. The global bond-orientation order-parameter and the anisotropy complex-order-parameter are distinguished by the data that is input into the equation. It is desirable to maximize the effect that bond direction plays on the order-parameter and minimize the effect of other types of disorder such as point defects. To do this, only the bond directions measured for NPs that are *well-ordered*, that is, *hexagonally packed*, were input when measuring anisotropy. NPs that were represented by Voronoi cells that fit two criteria were selected:

(1) The number of sides of the NPs' corresponding Voronoi cell matched the peak periodicity of ordering for the system (e.g. six for hexagonal close packing).

(2) All edge lengths of the corresponding Voronoi cell were within 60% of the median edge length of the cell. This filtered out all NPs represented by cells that have six neighbors but distorted from a perfect hexagon, thus are not well-ordered. Visual inspection was used to evaluate this criterion.

Figure VI.1a shows a Voronoi tessellation and Figure VI.1b shows the cells selected from the tessellation based on the two criteria. Additionally, each cell is colored-coded to indicate the mean direction of all the bonds that the cell represents. This color-coded figure makes it easy to identify anisotropy by visual inspection.

The magnitude of anisotropy, however, can be difficult to interpret. For example, if the sampled region of film is smaller than the correlation length of the system, one would expect most of the NPs to be well-packed within the same supercrystalline domain. In this case, a high degree of anisotropy would be measured simply because the measured sample size was too small. Thus, it is important to have a reference sample to compare to. However, the area analyzed from the reference sample must match the area analyzed for the sample of interest.

As the interpretation of the magnitude of anisotropy can be challenging, the direction of anisotropy, Θ_{an}, is introduced, which can also be used to detect anisotropy. By measuring the value of Θ_{an} for many large regions on a single sample, we can obtain a statistical mean value of Θ_{an} with an associated error. By comparing the magnitude of the error associated with a measurement Θ_{an} to the total range of Θ_{an}, the existence of anisotropy can be determined. As an example, in 2D samples where $\xi = 6$ (hexagonal

packing), Θ_{an} can only take values between 0° and 60°. Suppose one measures the value of Θ_{an} to be 30°±15°. In this scenario Θ_{an} has a ~66% chance of lying between 15° and 45°, or 50% of the available angular space. If all the bonds were oriented randomly, then there would be a 50% chance of that Θ_{an} lies between 15° and 45°. Because the probability of this value occurring randomly is so high, it is unlikely that anisotropy was present.

6.2.2 Ordering Measured by GISAXS

GISAXS offers a few advantages over the spatial statistics values calculated. First, obtaining knowledge of individual NP locations through real-space images can be hindered for many reasons such as the size of the NPs being too small to resolve using the applied technique or a surfactant coating on the film destroying the signal from the NPs. In many cases, GISAXS can be used to measure order even when the individual NPs cannot be identified via real space imaging techniques. Secondly, and most importantly for this dissertation, GISAXS can be used to perform scattering measurements on samples immersed in hexane. This ability of GISAXS will be used later to help determine when order is generated during EPD.

The scattering pattern measured on the GISAXS detector is mathematically equivalent to the square of the Fourier transform of the scattering density distribution of a sample. Because only the amplitude of the scattering is measured, direct inversion of scattering data is ill-posed and not possible. However, specific features in scattering patterns can be quantitatively interpreted. For example, as shown in Chapter V, the first-order peak of the Fourier transform of hexagonally packed NPs was visualized by six points evenly spaced around a ring. The first-order peak of the Fourier transform of

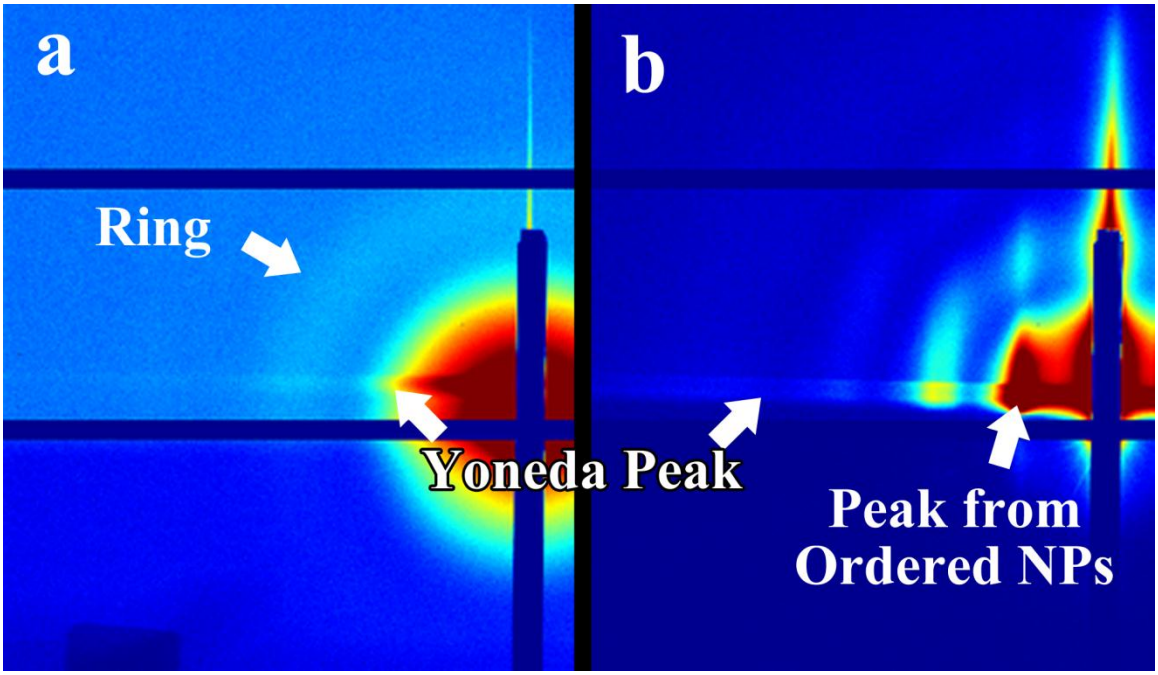

Figure VI.6: (a) GISAXS data from unordered particles deposited on a substrate. The ring is characteristic of unordered spheres. (b) GISAXS data from hexagonally packed NPs on a substrate. The first-order peak from the monolayer growth is indicated by the arrow. The Yoneda peak due to critical angle refraction on the substrate runs horizontally across both data sets.

unordered spherical particles, however, can be visualized as a ring from GISAXS data. Many quantitative details can be extracted from these patterns; in this work the patterns were utilized primarily to detect the existence or absence of order within a film. Figure VI.6 shows two GISAXS patterns, one of unordered and one of ordered NPs. The Yoneda peak in the figure appears as a horizontal streak in the two-dimensional scattering data; this feature arises from scattering that exits the sample at the critical angle. Refraction effects cause the data to appear distorted and compressed in GISAXS, especially at low angle (near the Yoneda peak). Figure VI.6a shows an unordered sample, represented as a ring in the data. Figure VI.6b shows a sample of NPs with some order, showing well-resolved peaks; the first-order peak is demarcated indicated. Increasing the

order within the system would result in sharper peaks allowing one to observe peaks of lower intensity and to more easily separate peaks located near one another.

CHAPTER VII

ORDERING IN MONOLAYERS OF IRON OXIDE NPS

With techniques for the fabrication of NPMs and tools for analysis of ordering within the NPMs in place, it is possible to study the mechanisms that generate order in the NPMs. As different types of NPs will behave differently during EPD, iron oxide NPs are discussed separately from cobalt ferrite NPs. First, NPMs composed of iron oxide NPs are studied using two experiments. In the first experiment, the effect on ordering due to magnetic interactions between two NPs is investigated. In the second experiment, *when* order occurs is determined, which allows one to make inferences about the mechanism that generates order.

7.1 Depositing Superparamagnetic Iron Oxide NPs in a 12 T Magnetic Field

As was observed within the iron oxide NPMs in previous chapters, local, hexagonal ordering existed within the films. Previous studies in the literature on films of magnetic NPs have shown that magnetic dipolar interactions between NPs during deposition may generate hexagonal ordering between the NPs [34, 117]. During EPD, the magnetic interactions between NPs can be controlled by depositing the NPs in a magnetic field. If a magnetic field is applied in the plane of the substrate (IP) during EPD, the dipole moments of the deposited NPs in the monolayer will align in multiple configurations including: head-to-tail, side-by-side, and configurations between these two states; however, if the magnetic field is applied perpendicular to the plane of the substrate

(out of plane, or OP) during EPD, the dipole moments of the deposited NPs in the monolayer can only align side-by-side. The head-to-tail alignment of the dipoles is a

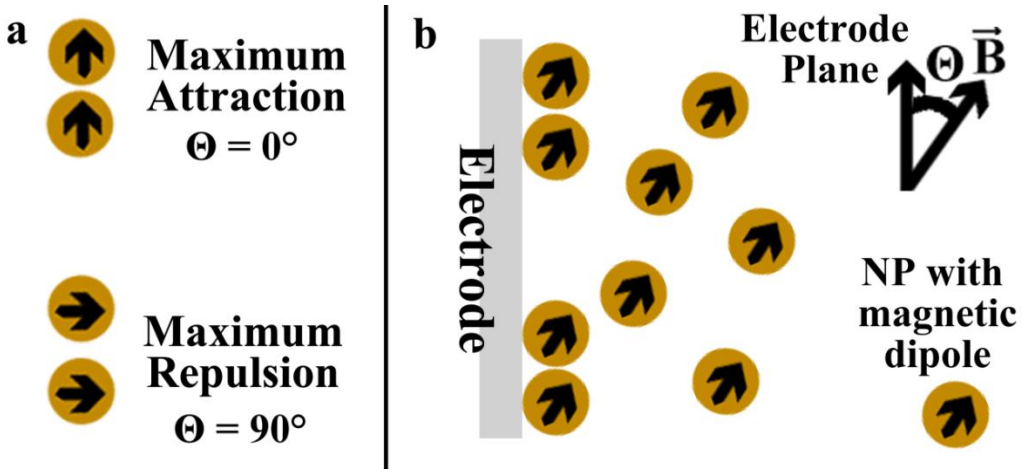

Figure VII.1: Schematic of magnetic NPs depositing during EPD in a magnetic field. (a) shows the arrangement of two single-domain, magnetic NPs. Maximal attraction between NPs can be induced by applying a magnetic field in the plane of the substrate, and maximal repulsion can be induced by applying a magnetic field out-of-plane of the substrate. (b) shows a schematic of one electrode during the EPD of NPMs in a magnetic field for an arbitrary Θ.

minimum energy configuration, and the side-by-side configuration is a maximum energy configuration (Figure VII.1). If magnetic interactions play a role in NP ordering, one would expect that the application of an external magnetic field at various angles relative to the substrate, which effectively controls the magnetic interactions between NPs, will cause the NP ordering within the film to vary [93]. Because the application of IP and OP external magnetic fields represent the two states with the greatest difference of energy between interacting magnetic dipoles, films deposited under these two conditions were studied. Then the order within the two films was measured and compared using the four measures of order that were presented in Chapter VI. If order is measured to be equivalent in both films, one could infer that magnetic interactions play no role in

ordering. However, if the measured order differs between the two films, then magnetic interactions likely do affect the ordering within the films.

7.1.1 Experimental

EPD was performed in a 12T magnetic field to orient the NPs, as shown in Figure VII.2. The saturation magnetization of the iron oxide samples was measured to be ~7T, meaning that 12T should be a sufficient field strength the saturate the sample. The deposition was performed in a specially designed, nonmagnetic deposition cell that allows one to orient the electrodes relative to the magnetic field (Figure VII.3). Voltage was transferred to the electrodes by the two nonmagnetic, aluminum screws that made electrical contact with a thin copper layer in contact with the electrodes. The screws were designed to also apply pressure to the electrodes to prevent the electrodes from moving. To perform EPD in the cell, two electrodes (1 cm x 1.5 cm) were placed into slots in the top seal of the cell. The slots were designed to keep the electrodes in parallel plate configuration with a 5 mm gap. After inserting the electrodes into the top seal, the aluminum screws were threaded through the top seal until sufficient pressure was applied to hold the electrodes snugly in place. The cell was then assembled by sliding a kapton tube over the top and bottom seal. The electrodes were then contained within the cell, and next the suspension was inserted into the cell through a filling hole in the top seal; air vented from the cell through the same filling hole. The cell was filled until no bubbles remain, and then the filling hole was sealed using a nylon screw. The cell was placed into the superconducting magnet at the chosen orientation of electrodes relative to the magnetic field (IP or OP) while the 12T field was on. Then, a 500 V potential was applied across the electrodes within the cell for 5 min. The cell was then removed from

the magnet, the suspension was extracted from the cell through the filling hole, and finally the electrodes were released from the cell by removing the bottom seal and

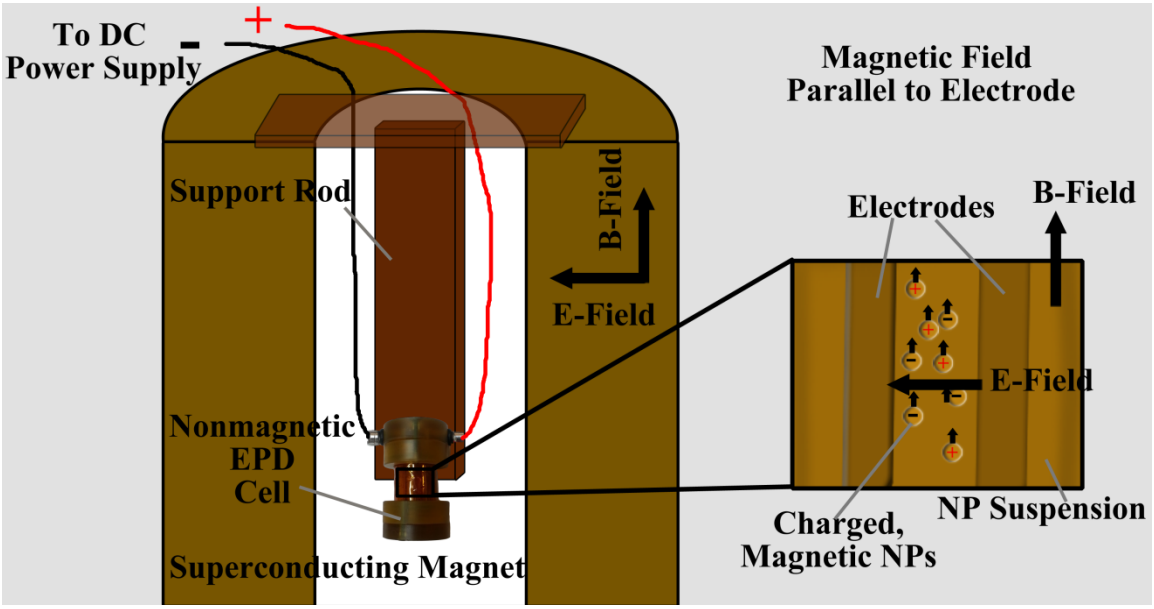

Figure VII.2: Schematic of experimental setup up used to perform EPD in a magnetic field. A nonmagnetic cell was inserted into a superconducting magnet. Two copper wires ran from the EPD cell to a power supply. The EPD cell could be oriented to control the angle between the substrate normal, which is parallel to the electric field, and the magnetic field (B-field). A magnified view inside the EPD cell shows how the electrodes orient within the cell. In the configuration shown, the magnetic field was parallel to the substrate.

aluminum screws. Two depositions were performed in this manner, once with IP and once with OP magnetic field orientations.

The resulting NP films were imaged using SEM with a 5 kV accelerating potential. Measurements of order were acquired from the images of monolayers that formed on the positive electrode using the techniques described in Chapter VI for both IP and OP orientations of the magnetic field. Statistical means and errors of order measurements were obtained by measuring order within multiple images (at least five) of

each electrode, and then taking the average and standard deviation of the values measured from each image, separately for each sample.

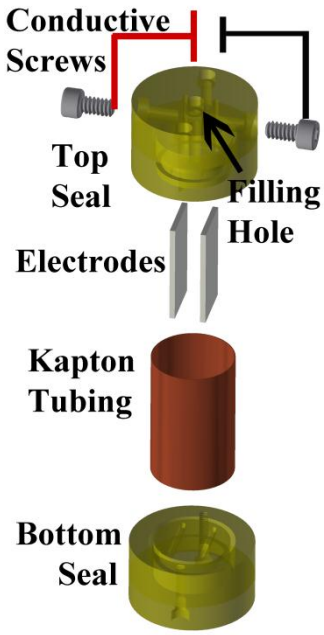

Figure VII.3: An exploded view of the EPD cell showing its construction. The substrates fit into a slot in the top seal and are held in place by conductive, aluminum, nonmagnetic screws. After inserting the electrodes in the top seal, the cell is assembled by sliding the kapton tube into the top and bottom seals. The cell is filled with NP suspension via the filling hole that also acts to vent the air during filling. The filling hole is sealed with a nylon screw. The cell can then be placed in a magnetic field where EPD is performed.

7.1.2 Results

Representative images of the monolayer films acquired from IP and OP orientations of the magnetic field are shown in Figure VII.4. Visual inspection of the films showed no distinct differences in order; however, the monolayer density appeared higher in the film deposited in a parallel magnetic field. Quantitative data acquired using the measures of order described in Chapter VI are given in Table VII-1. The local bond-orientational order-parameter, the translational order-parameter, the entropy from the

Voronoi-cell edge-fraction distribution, and the anisotropy direction in bonding were measured.

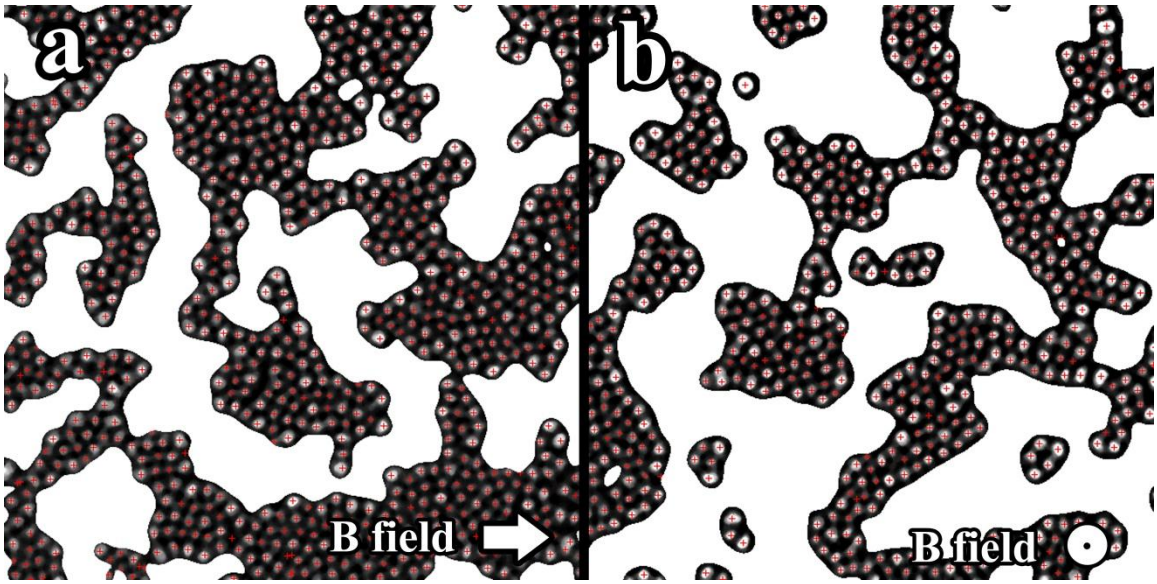

Figure VII.4: Analyzed SEM images of films deposited using magnetic fields oriented (a) IP and (b) OP. Voids within the film are colored white. NPs are identified with a red + marker.

If magnetic interactions between NPs during EPD are generating or affecting order, one would expect the all the measures of order to would be different for the IP and OP samples. However, the entropy and bond order-parameter were statistically equivalent for both films. A small difference was measured in the translational order, but this was attributed to the difference in monolayer density.

Finally, if magnetic ordering within the films were significant, then some anisotropy in bond direction would be expected to occur for particles deposited with an IP magnetic field while none would occur for NPs deposited in an OP field. Particle chains are often observed when creating monolayers of magnetic NPs in a magnetic field [93]. No chaining was observed, however, and statistical measurements of the direction

of anisotropy in bonding indicated that for both the IP and OP samples little to no anisotropy existed. In the first case, the anisotropy direction did not reflect the direction

Measurement	Out of Plane (OP)	In Plane (IP)
lBOOP	0.516±0.018	0.517±0.012
TOP	0.535±0.010	0.495±0.017
Entropy	1.067±0.010	1.09±0.04
Anisotropy Direction	16°±12°	27°±15°

Table VII-1: Measures of order were acquired from films deposited with magnetic fields parallel and perpendicular to the electrode surface. The local bond-orientation order parameter (lBOOP) and entropy were equivalent for the two samples. Differences in translational order parameter (TOP) were likely due to differences in monolayer density. The large errors in anisotropy direction indicated little to no anisotropy direction exists.

of the magnetic field in the IP sample. Additionally, the large errors in the directional measurement indicated that the observed direction is likely random. When taking into account the six-fold symmetry that limits the anisotropy direction from 0°-60°, the 12° and 15° errors can be interpreted to mean that little to no anisotropy existed.

7.1.3 Conclusions

As the two samples showed little to no difference in order, it was concluded that the magnetic interactions during EPD between the iron oxide NPs has little to no effect on the morphology of the film. As discussed previously, there are many mechanisms that may generate order within the NPMs. The investigations were initiated by studying magnetic interactions as this is a common cause of order within NP films and offers a

clear route to investigation (i.e. depositing in a magnetic field). Continuing by investigating each mechanism individually could prove tedious and unfruitful. Instead *when order occurs* during NPM fabrication rather than *a mechanism of order* can be investigated to indirectly determine or at least limit the possible mechanism that generated order.

7.2 Determining When Order Occurs Using GISAXS and DLS

In Chapter VI, many mechanisms were introduced by which monolayers can become ordered during EPD. Rather than testing each of these mechanisms one by one, the time at which order occurs during the deposition process can be determined. This would allow one to make inferences about the possible mechanisms that could produce this ordering. For example, if ordering occurred during deposition, then capillary forces could not be driving order. The EPD process can be divided into three distinct parts in time. Ordering, from the perspective of an individual NP, could occur *before* the NP deposits, *during* deposition, or *after* deposition.

More explicitly, the term *before deposition* means when the NP is still suspended and has not yet begun to interact with NPs already deposited on the substrate. Likely mechanisms that could generate order in the suspension before deposition are ligand-ligand interactions or dipole interactions that are induced or enhanced in the presence of the electric field [8, 118-120]. *During deposition* means when the NP nears the substrate and is interacting with NPs already deposited on the substrate. Order would likely occur here from magnetic or van der Waals interactions between NPs. *After deposition* means after the electrodes are removed from the suspension. If order occurs after deposition, capillary forces likely generate such order.

Two experiments were performed to study when order occurs. The first experiment was designed to determine if order occurred *before NPs deposit*. In this experiment, the hydrodynamic size of suspended objects was obtained by performing DLS measurements before and after EPD was performed. If ordering occurred before deposition, one would expect to find objects larger than a single NP in the suspension, which would represent agglomerated NPs.

The second experiment was designed to determine if NPs order *after deposition*. Order on an electrode was measured before extracting the electrodes from the suspension and after extracting and drying using GISAXS. If order between the NPs had been altered after extraction from the suspension, then ordering must have occurred after deposition. With both these experiments, one should be able to determine at which of the three stages of deposition order is generated.

7.2.1 Before Deposition

A simple experiment was performed to determine if order occurred before deposition. A suspension of iron oxide NPs was prepared for deposition via centrifugation techniques described in Chapter IV. TEM images of the NPs were collected to measure NP size. The suspension was characterized by measuring the hydrodynamic size and the mobility of the NPs (Figure VII.5, Figure VII.6). Mobility was collected simply to ensure that charged NPs existed in the suspension. Then, EPD was performed using the suspension. Large electrodes were used to perform EPD, two ~2.5 cm x 1 cm silicon electrodes for 10 mL of suspension, in order to maximize the suspension that experienced the electric field, and thus to maximize the amount of field-induced agglomeration that may occur between NPs. The deposition was performed at

500 V for 3 minutes. The electrodes were then extracted, and the potential remained on for one minute. After deposition, DLS and mobility measurements were again performed on the suspension. SEM was used to verify that deposition occurred.

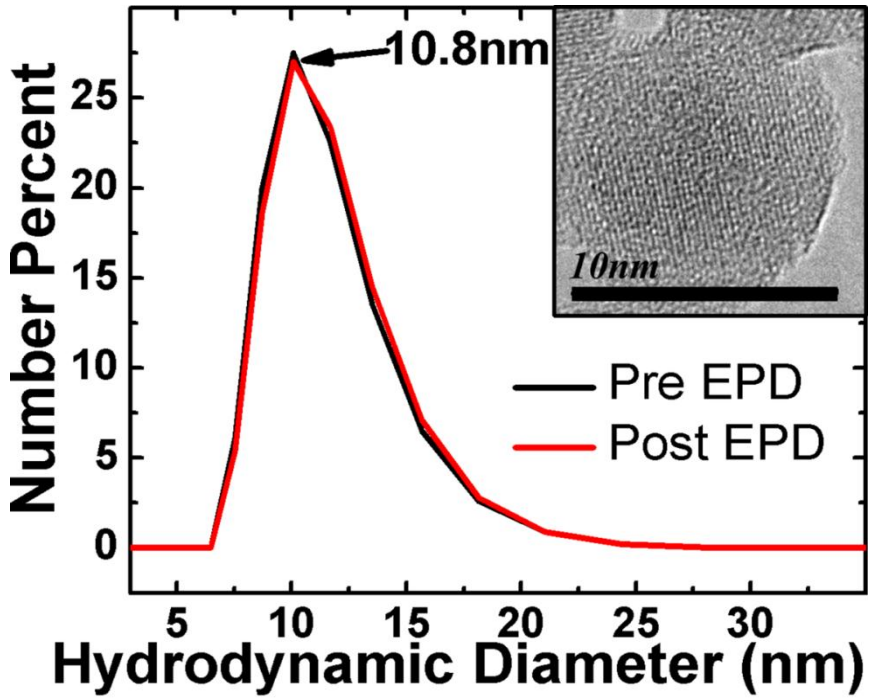

Figure VII.5: DLS data measured of a NP suspension before and after deposition. The TEM image (upper right) shows a single crystalline NP that is representative of the NPs that were deposited during the EPD. The size of the NPs under TEM was slightly smaller than the size of the NPs in suspension. This indicates that NPs were singly suspended. The NP size did not change before and after EPD, indicating that no agglomeration occurred before NPs deposited.

Figure VII.5 shows the TEM data and the results of the DLS measurements. The DLS measurements before and after deposition were very similar. The peak size measured from DLS was also just above the size measured by TEM. The increase in size can be explained by the surfactant and slipping plane around the NP. From this data, we inferred that particles are not sticking together before they deposit. Thus, ordering must

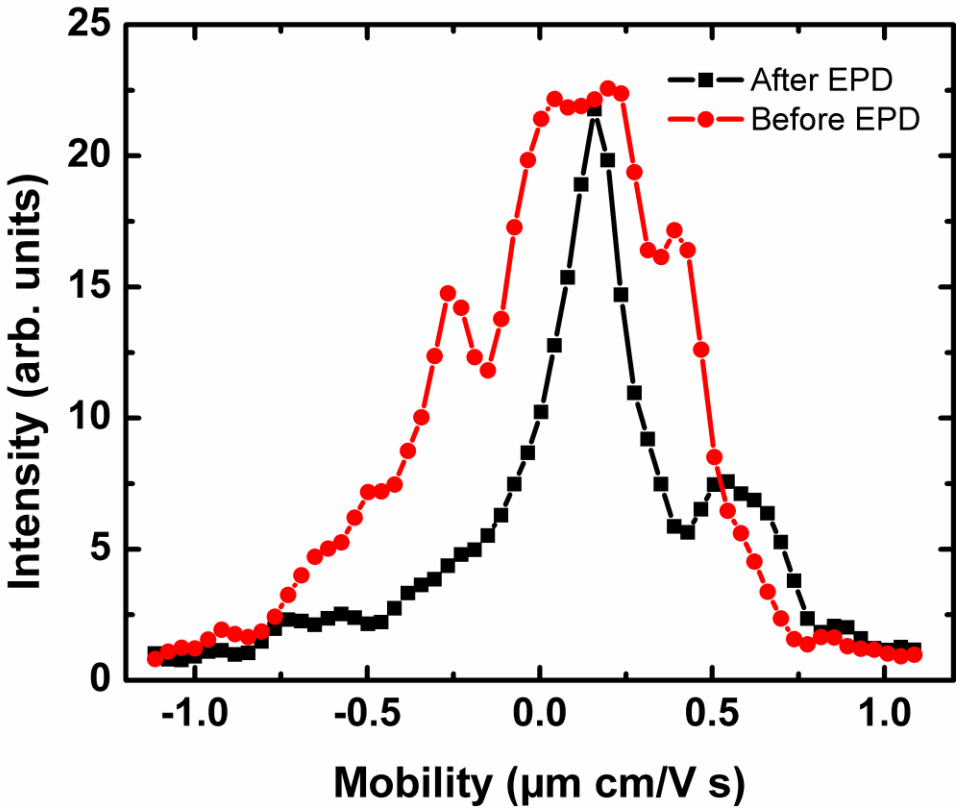

Figure VII.6: Mobility measurements before and after EPD. Before EPD, there are many charged NPs. After EPD, the number of charged NPs has reduced as some NPs have deposited on the substrate.

have occurred either during or after deposition. Figure VII.6 shows the mobility distribution of the suspension before and after. The figure shows that the charged particles were depleted after the deposition, indicating NPs were deposited with EPD.

7.2.2 After Deposition

GISAXS measurements of a NPM before and after extracting from a suspension were performed to determine if order occurs after deposition. To perform GISAXS before extracting the electrodes from the suspension, the same nonmagnetic cell described in Section 7.1 was used. X-rays can transmit through kapton easily and are only partially absorbed by the hexane in the cell (~50% absorption when passing through the hexane

within the cell, a distance of~1.5 cm), allowing one to measure the ordering of the NPs on a substrate immersed in hexane. With this cell, then, it was possible to perform EPD and then measure the order on the resulting films before extracting the films from the suspension.

One challenge however, was that the x-ray beam scattered off of NPs that remained suspended in the cell as well as those on the substrate. Given that the film only represented a small fraction of the total number of NPs in cell, the NPs that remained suspended scattered x-rays more strongly than the deposited NPs. To prevent scattering events from the suspended NPs, the brown-colored, suspended NPs were removed from the cell by purging the cell with hexane until the suspension appeared to be colorless.

7.2.2.1 Experimental

The experiment was performed by first assembling the EPD cell with silicon wafers as electrodes. The cell was then filled with iron oxide NP suspension. Deposition was performed at 1000 V for 10 min. GISAXS measurements were taken of both the suspension and the film before purging the cell with hexane. The filling hole on the cell was opened, and pure hexane was used to purge the suspension of NPs. The purging was done carefully to ensure the substrates were completely immersed in liquid during the whole process and that no bubble entered the cell. After purging, the filling hole was resealed, and the electrodes were measured again in the cell. After performing the measurement, the suspension was extracted from the cell, and the cell was disassembled. The electrodes were allowed ~10 min to dry before measuring again using GISAXS. All GISAXS measurements were performed at 0.05° incident angle relative to the substrate (this angle is not important for measurement through the suspension) for 15 seconds.

`

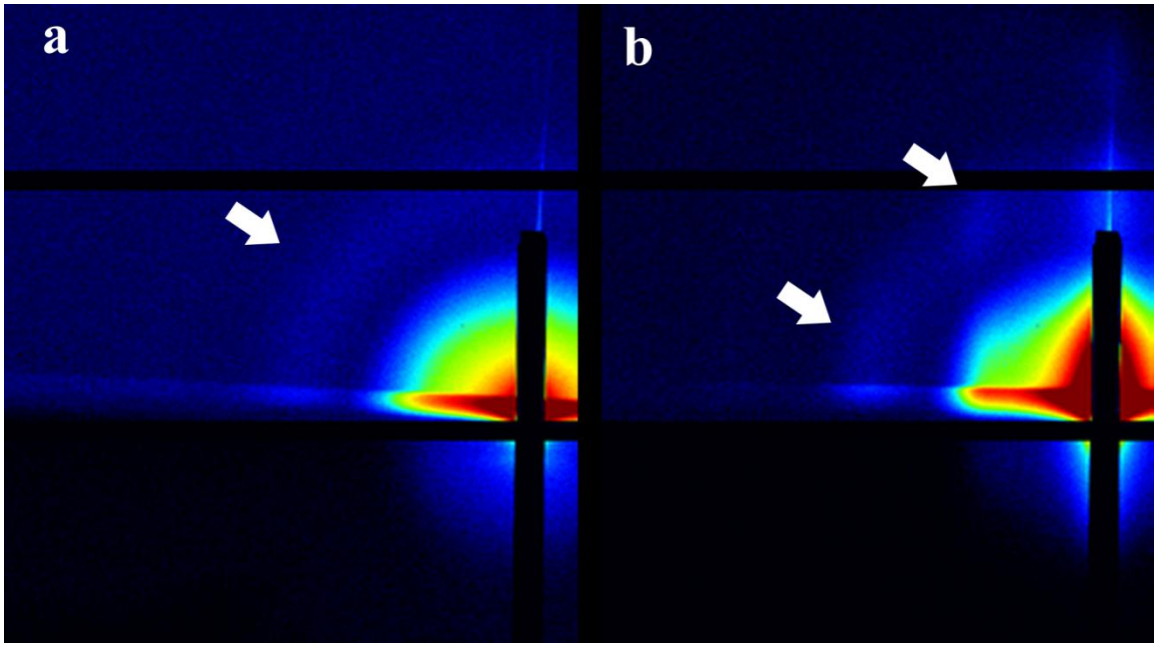

Figure VII.7: GISAXS data from (a) films before extracting from the EPD suspension and (b) after drying of the film. In (a), a bright ring indicates the presence of NPs that are not ordered. In (b), the ring has separated into two bright regions, indicating that hexagonally ordering has occurred.

7.2.2.2 Results & Discussion

GISAXS measurements of the suspension and the film performed before purging the cell with hexane gave very similar results, indicating the presence of spherical objects. The similarity of the results suggested that it may not be possible to measure order until the suspended NPs have been removed. For this reason, the cell was purged with hexane. After purging, GISAXS measurements of only the suspension produced a scattering pattern similar to the direct x-ray beam, indicating that little to no scattering was occurring. The patterns acquired from the negative film before and after extraction of the electrodes from the hexane are shown in Figure VII.7. The positive film gave similar results to the negative film. Figure VII.7a shows a faint ring (indicated by an arrow); this

pattern is characteristic of individual spheres that are unordered. Hence, from Figure VII.7a, it was inferred that the NPs had deposited but had yet to become ordered.

The GISAXS measurement after drying the substrate produced markedly different results. In Figure VII.7b, two peaks were observed in place of the ring previously observed. This scattering pattern is characteristic of hexagonally packed spheres. Thus, it was inferred that NPs had become ordered but only after the substrate had dried.

7.2.2.3 Conclusions

As discussed previously, the generation of ordering that occurred after drying was likely the result of capillary forces drawing the NPs together [121]. Thus, for these iron oxide NPs, we believe this was the driving mechanism behind ordering; however, further experiments could more definitively show that capillary forces were generating order and could be used to control order. As a starting point, the capillary force equation from Chapter VI indicates that the capillary force increases with increasing surface tension of the solvent. Thus, one possible experiment for determining the effect of capillary forces would be to deposit the NPs as described above and then replace the solvent before letting the NPM dry. Solvents of various surface tensions could be used, and the measures of order from Chapter VI could be applied to observe how order changes. If higher surface tension leads to increased order, this result would bolster the argument that capillary forces are driving order in this system.

An alternative experiment would be to dry the sample in a way that eliminates the effect of surface tension, and then to observe if order has still generated. Surface tension during drying could be eliminated by drying the sample at the critical point of the solvent (vapor, liquid, solid point) or using freeze drying techniques [122]. If capillary forces

were generating order, one would expect that no order would occur for samples dried using either of these techniques.

The role of surfactant in creating order is also open for debate. Since the iron oxide NPs were coated with oleic acid, it is possible that crosslinking between oleic acid molecules was affecting order during the drying process [123]. Possibly, the capillary forces acted to bring the particles near to one another, yet crosslinking between surfactant molecules forced them into hexagonally packed structures. Experimental verification of such a mechanism could be performed by comparing one film of iron oxide NPs coated with *stearic acid* and one film with NPs coated in *oleic acid*. Stearic acid is very similar to oleic acid; however no double bond exists so crosslinking is hindered. If order still occurred when using stearic acid as the surfactant, it would be possible to rule out cross-linking between ligands as the mechanism.

CHAPTER VIII

ORDERING IN COBALT FERRITE NPS

In the previous chapter, it was shown that magnetic interactions did not affect order and that capillary forces likely generated order in the system of superparamagnetic iron oxide NPs. As multiple mechanisms could generate order, by studying a different system it may be possible to observe a different ordering mechanism. Thus, this chapter describes a new system that incorporated a different type of NP, cobalt ferrite. By changing to cobalt ferrite NPs, a few properties of the system were changed, most notably the magnetic moment of the cobalt ferrite NPs increased by an order of magnitude and the magnetic easy axis has changed. Additionally, the cobalt ferrite NPs are slightly larger than iron oxide NPs and are stabilized using a combination of oleic acid and oleylamine. In this section, the role of magnetic interactions between cobalt ferrite NPs in generating order within NPMs will be investigated.

To begin the study of mechanisms that generate order in NPMs of cobalt ferrite NPs, order was compared between iron oxide and cobalt ferrite NPMs. Then GIWAXS results measured from cobalt ferrite NPMs were used to infer that NPs were interacting magnetically.

8.1 Cobalt Ferrite *versus* Iron Oxide NPMs

8.1.1 Ordering

When quantifying ordering within a representative NPM fabricated from the iron oxide NPs and a representative NPM of the cobalt ferrite NPs, a difference in order was

observed. Figure VIII.1 shows NPMs of cobalt ferrite and iron oxide, overlaid with a Voronoi tessellation. Comparing Figure VIII.1a with Figure VIII.1c, fewer defects existed in the cobalt ferrite film, as there were many more NPs with six sides. The void pattern was also very different in the films: in the iron oxide NP film, many small voids existed, while for cobalt ferrite NP film, the voids were much larger and few in number. Looking at only those NPs that were hexagonally well-packed (Figure VIII.1b,d) the cobalt ferrite NPM had large regions of NPs that were all packing in the same direction. This indicated that the correlation length in the cobalt ferrite NPMs was much larger than for the correlation length in iron oxide NPMs.

Next, the Voronoi-cell edge-fraction distributions for the two monolayers were compared (Figure VIII.2a). The cobalt ferrite peak at $n = 6$ was much higher (~85%) than that from iron oxide (~55%). Increased order was also observed in the local bond-orientation order parameter distribution as the curve for cobalt ferrite shows higher intensity on the right side of the graph (Figure VIII.2b). Finally, the radial distribution function showed enhanced order in the cobalt ferrite NPs as the peak height and area was enhanced (Figure VIII.2c). Such dramatic enhancement of order observed in cobalt ferrite NPMs strongly suggests that the mechanism behind ordering was different for the NPMs composed of cobalt ferrite and iron oxide.

8.1.2 Magnetic Interactions

The magnetic interaction between two NPs within a NPM can be calculated using the equation from magnetic dipole interactions from Chapter VI. To perform the calculation, one must know the magnetic moment of the NPs, the orientation of the NP moments, and the spacing between NPs within the monolayers. The spacing between NPs

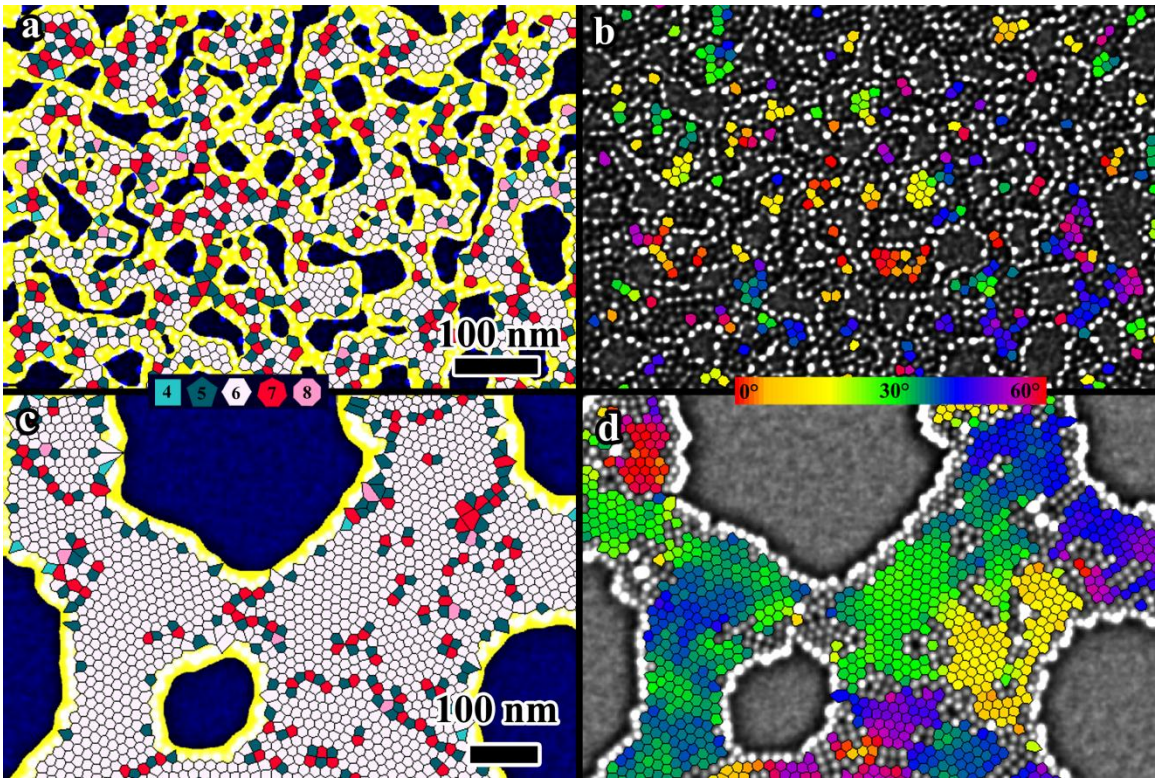

Figure VIII.1: (a) and (c) are a Voronoi diagrams overlaid on SEM images of iron oxide and cobalt ferrite NPMs, respectively. The colors of the cells represent the number of sides of the Voronoi cell. (b) and (d) display only Voronoi cells of hexagonally well-packed NPs. The color of a cell represents the average direction of all six bonds associated with said cell.

can be found by fitting the first peak of the radial distribution function to a Gaussian. The magnetic interaction energy between two NPs was calculated under the assumption that the NPs were oriented in a head-to-tail configuration, a maximally attractive orientation. For iron oxide, the spacing between nearest neighbor NPs was measured to be 13.4 nm and the moment is 1800μ_B, resulting in a maximal interaction energy of -0.005 k_BT. For cobalt ferrite, the NP-NP spacing was measured to be 15.2 nm and the moment is 26000μ_B, resulting in a maximal interaction energy of -0.8 k_BT. This interaction energy was still less than thermal energy, so possibly collective magnetic interactions between

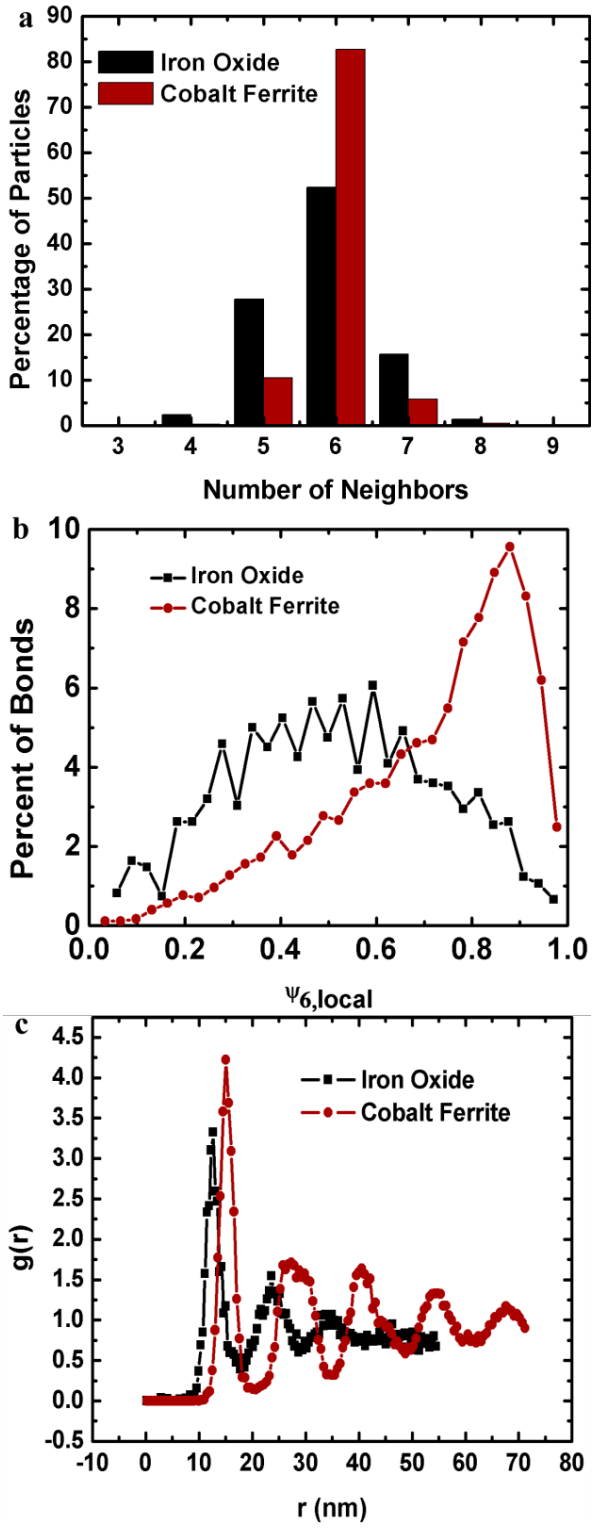

Figure VIII.2: (a) Voronoi-cell edge-fraction distribution, (b) local bond-orientation order parameter distribution, and (c) radial distribution function all show enhanced order in NPMs composed of cobalt ferrite NPs over NPMs composed of iron oxide NPs.

NPs generated order. This dramatic increase in ordering within cobalt ferrite NPs observed in tandem with the dramatic increase in magnetic interactions between NPs strongly suggested that magnetic interactions were generating order in the cobalt ferrite NPMs.

8.2 Observation of Crystalline Alignment in Cobalt Ferrite NPMs

If magnetic interactions between NPs were affecting order, one would expect that the magnetic easy axes of the NPs would align. If the magnetic interaction cause the moments to point out-of-plane relative to the substrate, the crystal would have only one rotational degree of freedom (around the easy axis). If the easy axes align in-plane relative to the substrate, the crystal will have two rotational degrees of freedom (around the easy axis and around the substrate normal). In both cases, x-ray scattering can be used to detect crystalline alignment in cubic crystals.

X-ray scattering measurements on NPMs of cobalt ferrite NPs were performed using GIWAXS. In the GIWAXS measurements shown in Figure VIII.3 a 2D scattering pattern composed of incomplete rings was observed [124]. The radial location of the peaks corresponds to peaks expected from the inverse spinel cobalt ferrite structure. The varying brightness around the rings indicated that crystalline alignment of NPs had occurred. The peaks, however, are diffuse indicating that complete crystalline alignment has not occurred. If magnetic interactions are causing the order, the crystals will have rotational freedom about the easy axis. If the easy axis points in plane, then the crystals will have a second rotational degree of freedom around the substrate normal.

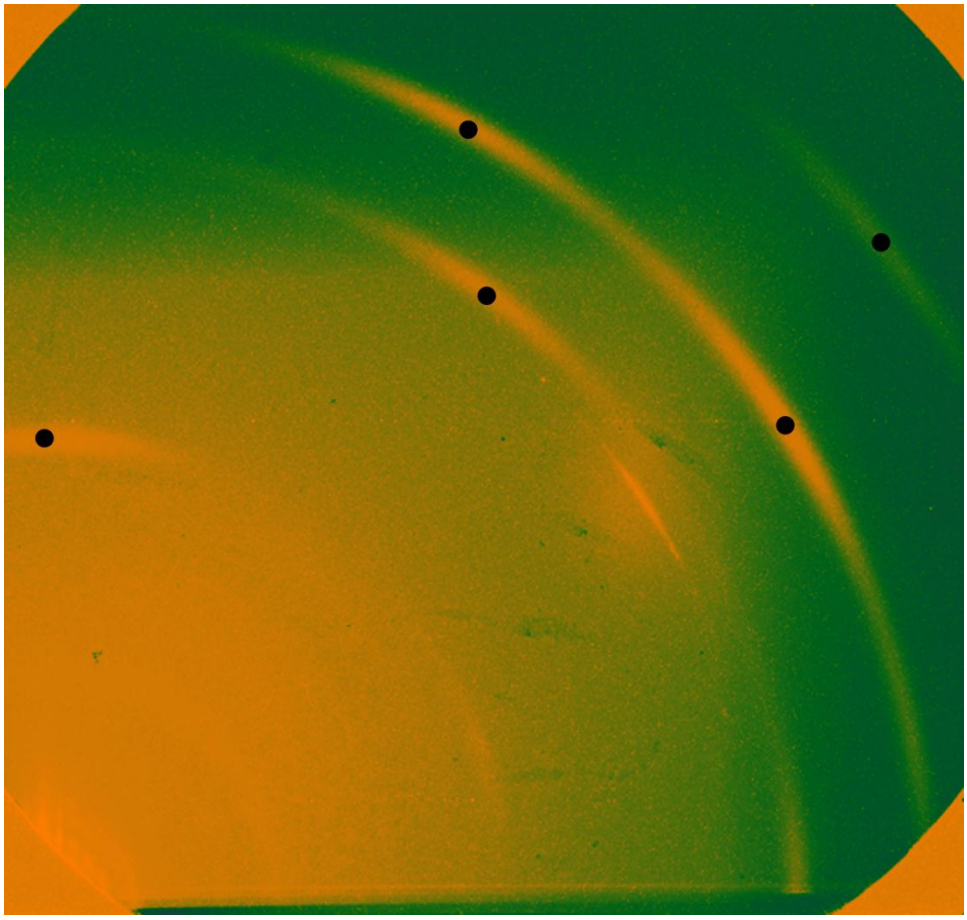

Figure VIII.3: GIWAXS measurement of cobalt ferrite NPM deposited using EPD. The incomplete rings indicate alignment of crystal axes of NPs. Black dots mark the center of the diffuse peaks that correspond to the cobalt ferrite crystal.

8.3 Conclusions

The results, thus far, strongly suggest that magnetic interactions play a role in NP ordering for cobalt ferrite NPs. By modeling the crystalline orientation of the NPs and matching it to the experimental data, it would be possible to determine the orientation of the crystals within the NPMs. If the magnetic easy axes are aligned, then very likely magnetic interactions are the source of order. Even stronger evidence that magnetic

interactions generated order could be obtained by repeating the experiment performed by depositing iron oxide NPs in a magnetic field but using the cobalt ferrite NPs.

The orientation of the magnetic moment of individual NPs would also provide definitive proof of magnetic interactions between NPs. If the moments point OP, the orientation of the moment of each NP could perhaps be measured using magnetic force microscopy (MFM) [60, 125]. MFM is sensitive to magnetic fields pointing normal to the surface. If the moments point OP, Lorentz microscopy and electron holography may also be useful in the measurement of the magnetic fields emanating from the NPs, however these techniques primarily are sensitive to magnetic fields in the plane of the substrate [88, 126, 127].

Finally, even if order was primarily generated by magnetic interactions, capillary forces and other interactions may have affected the order. While order was significantly enhanced in cobalt ferrite NPMs over the iron oxide NPMs, and magnetic interactions likely generated this increase in order, more investigation should be performed to completely understand the mechanism that generated order and how such order could be enhanced.

CHAPTER IX

CONCLUSION

The focus of this dissertation has been to demonstrate the use of EPD to fabricate NPMs in a general way and to study the mechanisms that generate order in these NPMs. In regards to generality, the important features of NP suspensions needed to reproducibly fabricate NPMs of many types of NPs via EPD have been demonstrated. In regards to studying order, many tools were introduced that can be used to measure order in NPMs. Using these tools, it was possible to determine likely mechanisms that generated order in two different NP systems. In iron oxide NP systems, magnetic interactions were determined to play little to no role in ordering. Additionally, it was found that ordering of the iron oxide NPs occurred after the films dried, implicating capillary forces as the likely mechanism of ordering. In contrast, a significant difference in the degree of order was observed between the cobalt ferrite and iron oxide NPMs. From GIWAXS data it was possible to infer that magnetic interactions between the cobalt ferrite NPs likely generated order.

The study of monolayers fabricated via EPD, however, has just begun with this work. The research at this point has opened up many new questions that remain to be studied. For example, after determining the mechanisms that generate order, one could naturally transition into controlling such order. In a system such as iron oxide, where capillary forces likely drive order, control of capillary forces should be investigated to create more and less ordered systems. Such investigation could be accomplished using

critical point drying or freeze drying to remove capillary forces or by drying in solvents with various surface tensions. Another possible route to control order is repeated drying of the sample.

For cobalt ferrite, the evidence implicated magnetic interactions between NPs in the generation of order within the NPMs. Yet, further experiments need be performed to more definitively prove the role of magnetism as well as to study other mechanisms that may play a role. For example, depositing the NPs in a magnetic field, as was done with iron oxide, should alter the morphology of the film if magnetic interactions affect morphology. Another route to study magnetic could be accomplished by coating the separate batches of cobalt ferrite NPs with surfactants of different lengths. The interactions between NPs could be tuned by controlling the spacing between the NPs, and the spacing can be controlled using various lengths of the surfactant coating the NP. Furthermore, capillary forces likely still affect the ordering in these films as they did in iron oxide. Thus, the effect of capillary forces should be investigated. Additionally, magnetic interactions could be studied by coating the NPs in surfactants with various lengths to control the spacing between NPs and thus control the magnetic interactions between the NPs.

Order plays a crucial role in determining the behavior of NP assemblies. The work at this point has studied what mechanisms generate order, but has done little to enhance the order that naturally occurs. Thus, we implore future researchers to investigate techniques for enhancing order in films fabricated via EPD. Because EPD is a very versatile and scalable process, the NPMs fabricated with EPD hold great potential in many applications.

Yet, two properties of EPD present major challenges to the creation ordered films via EPD. First, the substrate surface in EPD is typically symmetric in two-dimensions, allowing bonds between NPs to orient in any direction. Second, films formed during EPD will grow simultaneously in multiple regions on the substrate. Two neighboring nucleation centers will be initially uncorrelated until film regions grow large enough to merge. This merger will likely introduce many defects. Thus, if one wishes to create large, ordered regions of film using EPD, it will be important to break the symmetry of the substrate as well as introduce correlation between all NPs on the film.

One way to simultaneously address both issues is to deposit NPs on a substrate with a template [13, 18]. Such a template could be lithographically patterned on the substrate. With the appropriate template design, symmetry in the system can be broken and correlation between all NPs can be mediated by interactions with the template. If the ultimate goal of nanoscience is to create new materials with unique properties that can be studied to discover new fundamental science and implemented in applications, then we believe that ordered films fabricated via EPD have great potential to satisfy the goals of nanoscience. To achieve this goal, however, more investment in research must be made to better understand how the films are formed and to better control the films. I look forward to seeing where others will take this work.

APPENDIX

A.1 IMAGE PROCESSING

Before taking statistical measurements of order within the films, one must first be able to locate NPs as well as locate the boundary of the film. The boundary (or edge) of the film is taken to be the edge of the image as well as regions of the film where no NPs have deposited despite sufficient space for NP deposition (voids). This information is stored within SEM images of the films but must first be extracted and formatted to be useable. In the following section, extraction of this data will be discussed. This appendix will begin by locating voids within the films by segmenting the SEM images. Then a method to identify and locate NPs will be discussed.

A.1.1 Locating Voids using Image Segmentation

The locations of voids were detected by segmenting the original SEM image into a black and white image, where black indicated voids and pattern elements in the film and white indicated regions where NPs have deposited. When the film was imaged, the NPs generated an average intensity that was different from the average intensity of voids. This difference in intensity exhibited by the two regions of the film can be exploited to segment the images.

The image was run through a series of filters and other image adjustments to enhance the contrast between the two regions of film. The major image processing steps described below are shown in Figure A.1. First, a series of filters (median, Gaussian blur (low pass), and high pass) were applied. Median filters are non-linear filters which address a single pixel, and replace said pixel by the median value of pixels in an $N \times M$

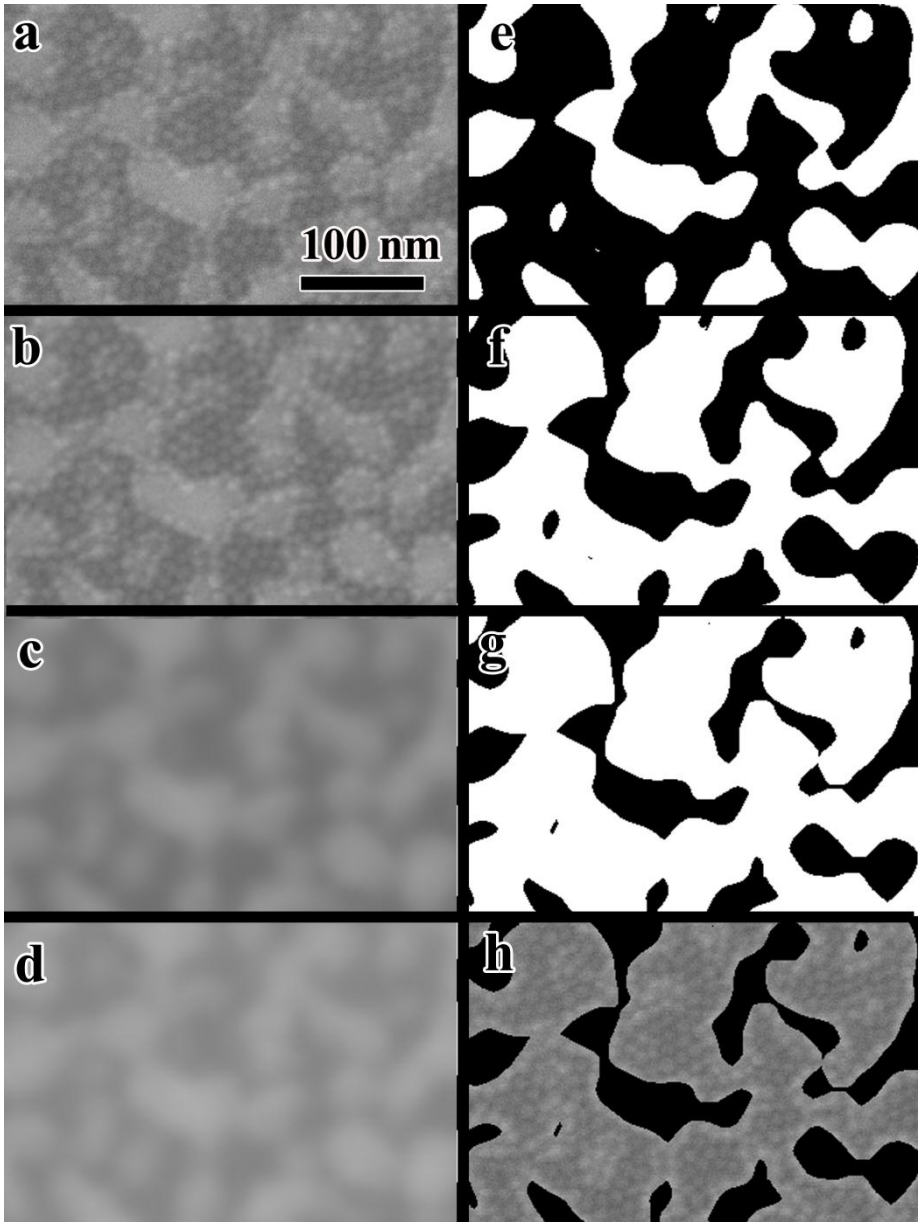

Figure A.1: Shows the series of processing steps that lead to segmentation of the original SEM image. (a) The original SEM image. (b) The image after the application of a median filter. (c) The image after a subsequent application of a 6 pixel Gaussian blur. (d) The image after the application of a 47.7 pixel high pass filter. (e) Contrast adjustments and image multiplications were used to convert image into a binary image. (f) The image was inverted. (g) A morphological operation (maximum) was used to shrink the identified void regions to the appropriate size. (h) Lastly, the data that comprised (a) and (g) were multiplied together. The resulting image was visually inspected to determine the quality of the image segmentation.

neighborhood (kernel) around said pixel. Median filters are very effective at removing impulse noise (isolated noise spikes) while preserving high frequency detail (edges). A Gaussian blur is a low pass filter that attenuates high frequency data while passing low-frequency data. For the purposes of segmentation, individual NPs were not important; rather, the region that was occupied by NPs was of interest. Thus, a Gaussian blur was applied such that the edge data for NPs were lost, making the NPs indistinguishable. High-pass filters act in the opposite manner to low pass filters, attenuating low frequencies and passing high frequencies within the data. In this way, very low frequency data that does not give information on the location of NPs can be removed. For the image segmentation, the desired effect of the high-pass filter was to make the average intensity uniform throughout the image (leveling).

Next, a series of contrast adjustments and image multiplications (multiplying the image by itself in this case) were applied, with the final contrast adjustment creating a black and white image. In some instances, the image needed to be inverted so that voids are black. Then, a maximum or minimum morphological operation was used to make minor adjustments to the size of the segmented regions (Figure A.1 shows an example sequence of images after applying each filter). One aspect of this technique worth noting is that the blur of the Gaussian filter limited the size of the void that could be detected. Thus, smaller voids would blend in with the NPs and be identified as regions with NPs. To verify the efficacy of this procedure, the resulting segmented image was multiplied by the original image; the resulting image was compared by visual inspection to the original SEM image.

A.1.2 Identifying and Locating NPs

To identify NPs in each image, a series of filters was again applied to the original SEM images but with a different focus in mind (Figure A.2). First, a median filter was used to remove impulse noise. A high pass filter was used to level the image while maintaining the definition of each NP. A Gaussian filter was applied to remove noise within an individual NP while again maintaining individual NP definition. The Gaussian filter also acted to enhance the intensity at the center of the NP, allowing one to locate the center of the NP by finding regional intensity maxima throughout the processed image. After this, a series of contrast adjustments and image multiplications were applied to enhance the contrast between the NPs and the background. The NPs were then identified by using MATLAB's *imregionalmax* function, which finds the regional maxima within an image. In some cases, the *imregionalmax* function may be unable to identify a single pixel as a regional maximum and instead supplies two or more connected pixels as a single identified maximum. This often occurs when a NP seen in the image was saturated either during imaging or during image processing steps, thus the NP was represented by multiple pixels that had reached the maximal bit depth available within the image. When this occured, the centroid of connected pixels (based on 8-connectivity) was used as the center of a NP. After having found the locations of the NPs, a marker (red plus) was drawn at each NP location. The images were then visually inspected to ensure that NPs were being identified correctly and the center of each NP was located. (Figure A.2 shows an example sequence of images after each filter).

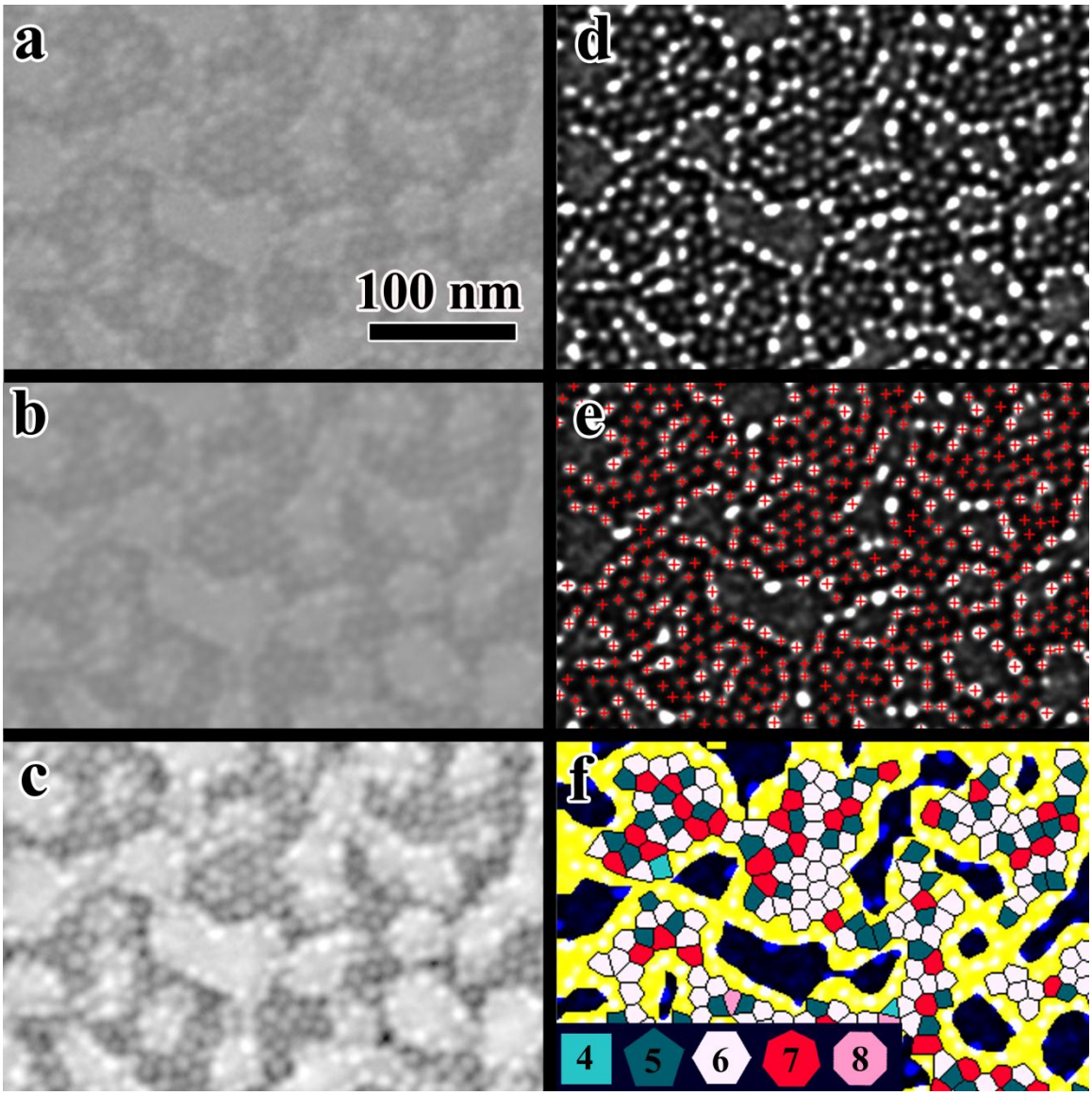

Figure A.2: The sequence of image processing steps that facilitated NP identification and location required for the statistical analyses applied to the images. The original image is the same as shown in Figure A.1. (a)The image after median filter and 15.8 pixel high pass filter. (b) The image after the application of a 1.5 pixel Gaussian blur. (c) The image after the application of a contrast adjustment. (d) The image obtained by squaring the image shown in (c). Regional maxima found within this image are identified as NPs. (e) Image with located NPs marked with a "+" symbol. (f) This image depicts the final Voronoi tessellation. The dark blue areas correspond to locations of voids as shown in Figure A.1; the yellow areas correspond to locations where boundary NPs did exist, as determined by the image segmentation process. The boundary NPs are identified as those NPs represented by a Voronoi cell with at least one vertex located in a void region.

REFERENCES

[1] R. G. Freeman, K. C. Grabar, K. J. Allison, R. M. Bright, J. A. Davis, A. P. Guthrie, M. B. Hommer, M. A. Jackson, P. C. Smith, D. G. Walter, and M. J. Natan, Science **267** (1995).

[2] T. Okamoto, I. Yamaguchi, and T. Kobayashi, Optics Letters **25** (2000).

[3] S. A. Maier, P. G. Kik, H. A. Atwater, S. Meltzer, E. Harel, B. E. Koel, and A. A. G. Requicha, Nature Materials **2** (2003).

[4] D. V. Talapin, J. S. Lee, M. V. Kovalenko, and E. V. Shevchenko, Chemical Reviews **110** (2010).

[5] N. Zaitseva, Zu Rong Dai, F. R. Leon, and D. Krol, Journal of the American Chemical Society **127** (2005).

[6] A. Taleb, F. Silly, A. O. Gusev, F. Charra, and M. P. Pileni, Advanced Materials **12** (2000).

[7] A. Courty, A. I. Henry, N. Goubet, and M. P. Pileni, Nature Materials **6** (2007).

[8] D. Nykypanchuk, M. M. Maye, D. van der Lelie, and O. Gang, Nature **451** (2008).

[9] C. B. Murray, S. Sun, W. Gaschler, H. DoyLe, T. A. Betley, and C. R. Kagan, IBM Journal of Research and Development **45** (2001).

[10] E. V. Shevchenko, D. V. Talapin, N. A. Kotov, S. O'Brien, and C. B. Murray, Nature **439** (2006).

[11] E. V. Shevchenko, J. Kortright, D. V. Talapin, S. Aloni, and A. P. Alivisatos, Advanced Materials **19** (2007).

[12] E. V. Shevchenko, M. Ringler, A. Schwemer, D. V. Talapin, T. A. Klar, A. L. Rogach, J. Feldmann, and A. P. Alivisatos, Journal of the American Chemical Society **130** (2008).

[13] A. J. Krejci, C. G. W. Thomas, and J. H. Dickerson, Physical Review E **87** (2013).

[14] A. J. Krejci, C. G. Thomas, J. Mandal, I. Gonzalo-Juan, W. He, R. L. Stillwell, J.-H. Park, D. Prasai, V. Volkov, and K. I. Bolotin, The Journal of Physical Chemistry B **117** (2012).

[15] M. Hilgendorff, B. Tesche, and M. Giersig, Australian Journal of Chemistry **54** (2002).

[16] A. C. Johnston-Peck, J. Wang, and J. B. Tracy, Langmuir **27** (2011).

[17] A. Swami, A. Kumar, P. Selvakannan, S. Mandal, and M. Sastry, Journal of Colloid and Interface Science **260** (2003).

[18] I. Bita, J. K. W. Yang, Y. S. Jung, C. A. Ross, E. L. Thomas, and K. K. Berggren, Science **321** (2008).

[19] A. J. Krejci, I. Gonzalo-Juan, and J. H. Dickerson, ACS Applied Materials & Interfaces (2011).

[20] A. J. Krejci, J. Mandal, and J. H. Dickerson, Applied Physics Letters **101** (2012).

[21] M. Giersig, and P. Mulvaney, Journal of Physical Chemistry **97** (1993).

[22] T. Teranishi, M. Hosoe, and M. Miyake, Advanced Materials **9** (1997).

[23] S. A. Hasan, D. W. Kavich, S. V. Mahajan, and J. H. Dickerson, Thin Solid Films **517** (2009).

[24] S. V. Mahajan, and J. H. Dickerson, Applied Physics Letters **96** (2010).

[25] S. A. Hasan, J. L. Rigueur, R. R. Harl, A. J. Krejci, I. Gonzalo-Juan, B. R. Rogers, and J. H. Dickerson, ACS Nano **4** (2010).

[26] J. L. Rigueur, S. A. Hasan, S. V. Mahajan, and J. H. Dickerson, Carbon **48** (2010).

[27] S. Somarajan, S. A. Hasan, C. T. Adkins, E. Harth, and J. H. Dickerson, The Journal of Physical Chemistry B **112** (2008).

[28] M. A. Islam, Y. Q. Xia, M. L. Steigerwald, M. Yin, Z. Liu, S. O'Brien, R. Levicky, and I. P. Herman, Nano Letters **3** (2003).

[29] M. A. Islam, and I. P. Herman, Applied Physics Letters **80** (2002).

[30] S. V. Mahajan, J. Cho, M. S. P. Shaffer, A. R. Boccaccini, and J. H. Dickerson, Journal of the European Ceramic Society **30** (2010).

[31] S. V. Mahajan, and J. H. Dickerson, Nanotechnology **21** (2010).

[32] I. Zhitomirsky, Advances in Colloid and Interface Science **97** (2002).

[33] S. Sun, C. Murray, D. Weller, L. Folks, and A. Moser, Science **287** (2000).

[34] D. V. Talapin, E. V. Shevchenko, C. B. Murray, A. V. Titov, and P. Kral, Nano Letters **7** (2007).

[35] S. A. Hasan, D. W. Kavich, and J. H. Dickerson, Chemical Communications **25** (2009).

[36] P. Sarkar, and P. S. Nicholson, Journal of the American Ceramic Society **79** (1996).

[37] E. M. Wong, and P. C. Searson, Chemistry of Materials **11** (1999).

[38] E. M. Wong, and P. C. Searson, Applied Physics Letters **74** (1999).

[39] E. J. W. Verwey, J. T. G. Overbeek, and K. Van Nes, *Theory of the stability of lyophobic colloids: the interaction of sol particles having an electric double layer* (Elsevier New York, 1948).

[40] B. Derjaguin, and L. Landau, Acta Physicochim. URSS **14** (1941).

[41] P. G. Smith, M. N. Patel, J. Kim, T. E. Milner, and K. P. Johnston, The Journal of Physical Chemistry C **111** (2007).

[42] M. Hsu, E. R. Dufresne, and D. Weitz, Langmuir **21** (2005).

[43] I. Gonzalo-Juan, A. J. Krejci, and J. H. Dickerson, Langmuir **28** (2012).

[44] S. Sun, H. Zeng, D. B. Robinson, S. Raoux, P. M. Rice, S. X. Wang, and G. Li, Journal of the American Chemical Society **126** (2004).

[45] C. Petit, A. Taleb, and M. Pileni, The Journal of Physical Chemistry B **103** (1999).

[46] D.-H. Chen, J.-J. Yeh, and T.-C. Huang, Journal of Colloid and Interface Science **215** (1999).

[47] P. G. Smith, M. N. Patel, J. Kim, K. P. Johnston, and T. E. Milner, The Journal of Physical Chemistry C **111** (2007).

[48] D. W. Kavich, *Nanoscale magnetism and exchange bias coupling at the antiferromagnetic/ferrimagnetic interface* (ProQuest, 2008).

[49] M. Vargas, A. Albors, A. Chiralt, and C. González-Martínez, Food Hydrocolloids **23** (2009).

[50] B. Neirinck, J. Fransaer, O. V. d. Biest, and J. Vleugels, Electrochemistry Communications **11** (2009).

[51] T. Uchikoshi, K. Ozawa, B. D. Hatton, and Y. Sakka, Journal of Materials Research **16** (2001).

[52] R. Hebner, E. Kelley, E. Forster, and G. FitzPatrick, IEEE Transactions on Electrical Insulation (1985).

[53] M. G. Song, K. J. M. Bishop, A. O. Pinchuk, B. Kowalczyk, and B. A. Grzybowski, Journal of Physical Chemistry C **114** (2010).

[54] B. Ferrari, and R. Moreno, Journal of the European Ceramic Society **30** (2010).

[55] J. J. Van Tassel, *Electrophoretic deposition: fundamentals, mechanisms and examples with an in depth examination of the ion depletion effect* (The Pennsylvania State University, 2004).

[56] J. H. Masliyah, and S. Bhattacharjee, *Electrokinetic and colloid transport phenomena* (Wiley-Interscience, 2006).

[57] H. Zeng, S. Sun, T. Vedantam, J. Liu, Z.-R. Dai, and Z.-L. Wang, Applied Physics Letters **80** (2002).

[58] A. Moser, K. Takano, D. T. Margulies, M. Albrecht, Y. Sonobe, Y. Ikeda, S. Sun, and E. E. Fullerton, Journal of Physics D: Applied Physics **35** (2002).

[59] S. H. Sun, H. Zeng, D. B. Robinson, S. Raoux, P. M. Rice, S. X. Wang, and G. X. Li, Journal of the American Chemical Society **126** (2004).

[60] V. F. Puntes, P. Gorostiza, D. M. Aruguete, N. G. Bastus, and A. P. Alivisatos, Nature Materials **3** (2004).

[61] R. T. Schumacher, and C. P. Slichter, Physical Review **101** (1956).

[62] E. Brunsman, J. Scott, S. Majetich, M. McHenry, and M. Q. Huang, Journal of Applied Physics **79** (1996).

[63] R. Nesbet, Physical Review **135** (1964).

[64] V. Romanov, and L. Checherskaya, Physica Status Solidi (b) **49** (1972).

[65] T. B. Garrett, and D. Zeroka, International Journal of Quantum Chemistry **6** (1972).

[66] M. Tokumoto, H. Ihara, T. Matsubara, M. Hirabayashi, N. Terada, H. Oyanagi, K. Murata, and Y. Kimura, Japanese Journal of Applied Physics **26** (1987).

[67] C. Kittel, Reviews of Modern Physics **21** (1949).

[68] E. C. Stoner, and E. Wohlfarth, Philosophical Transactions of the Royal Society of London. Series A. Mathematical and Physical Sciences (1948).

[69] F. Zhao, H. L. Sun, G. Su, and S. Gao, Small **2** (2006).

[70] R. J. McQueeney, M. Yethiraj, S. Chang, W. Montfrooij, T. Perring, J. M. Honig, and P. Metcalf, Physical Review Letters **99** (2007).

[71] S. Mann, R. B. Frankel, and R. P. Blakemore, Nature **310** (1984).

[72] G. Goya, T. Berquo, F. Fonseca, and M. Morales, Journal of Applied Physics **94** (2003).

[73] D. Huang, C. Chang, H.-T. Jeng, G. Guo, H.-J. Lin, W. Wu, H. Ku, A. Fujimori, Y. Takahashi, and C. Chen, Physical Review Letters **93** (2004).

[74] S. Lee, C. Lo, P. Matlage, S. Song, Y. Melikhov, J. Snyder, and D. Jiles, Journal of Applied Physics **102** (2007).

[75] M. Kriegisch, W. Ren, R. Sato-Turtelli, H. Muller, R. Grossinger, and Z. Zhang, Journal of Applied Physics **111** (2012).

[76] N. Somaiah, T. V. Jayaraman, P. Joy, and D. Das, Journal of Magnetism and Magnetic Materials (2012).

[77] I. Nlebedim, J. Snyder, A. Moses, and D. Jiles, Magnetics, IEEE Transactions on **48** (2012).

[78] G. Sawatzky, F. Van Der Woude, and A. Morrish, Journal of Applied Physics **39** (1968).

[79] M. Tachiki, Progress of Theoretical Physics **23** (1960).

[80] A. W. Burton, K. Ong, T. Rea, and I. Y. Chan, Microporous and Mesoporous Materials **117** (2009).

[81] W. Regan, N. Alem, B. Alemán, B. Geng, C. Girit, L. Maserati, F. Wang, M. Crommie, and A. Zettl, Applied Physics Letters **96** (2010).

[82] S. Calvin, S. Luo, C. Caragianis-Broadbridge, J. McGuinness, E. Anderson, A. Lehman, K. Wee, S. Morrison, and L. Kurihara, Applied Physics Letters **87** (2005).

[83] M. V. Kovalenko, M. I. Bodnarchuk, R. T. Lechner, G. Hesser, F. Schaffler, and W. Heiss, Journal of the American Chemical Society **129** (2007).

[84] J. Park, K. J. An, Y. S. Hwang, J. G. Park, H. J. Noh, J. Y. Kim, J. H. Park, N. M. Hwang, and T. Hyeon, Nature Materials **3** (2004).

[85] C.-H. Hsia, T.-Y. Chen, and D. H. Son, Nano Letters **8** (2008).

[86] B. J. Berne, and R. Pecora, *Dynamic light scattering: with applications to chemistry, biology, and physics* (Courier Dover Publications, 1976).

[87] W. Goldburg, American Journal of Physics **67** (1999).

[88] K. Yamamoto, C. R. Hogg, S. Yamamuro, T. Hirayama, and S. A. Majetich, Applied Physics Letters **98** (2011).

[89] Y. Lu, G. L. Liu, and L. P. Lee, Nano Letters **5** (2005).

[90] S.-Y. Zhao, S.-H. Chen, D.-G. Li, M. Zhou, and H.-Y. Ma, Electrochemical and Solid-State Letters **10** (2007).

[91] A. T. Heitsch, R. N. Patel, B. W. Goodfellow, D.-M. Smilgies, and B. A. Korgel, The Journal of Physical Chemistry C **114** (2010).

[92] Z. Sun, M. Wolkenhauer, G.-G. Bumbu, D. Kim, and J. Gutmann, Physica B: Condensed Matter **357** (2005).

[93] M.-P. Pileni, *Nanocrystals forming mesoscopic structures* (Wiley-VCH, 2006).

[94] J. S. Park, and D. Saintillan, Key Engineering Materials **507** (2012).

[95] J. D. Jackson, *Classical Electrodynamics* (John Wiley & Sons, New Delhi, 1999), 3 edn.

[96] J. Mahanty, and B. W. Ninham, *Dispersion forces* (IMA, 1976), Vol. 5.

[97] B. Faure, G. Salazar-Alvarez, and L. Bergstrom, Langmuir **27** (2011).

[98] Y. Lalatonne, J. Richardi, and M. Pileni, Nature Materials **3** (2004).

[99] H. Morimoto, and T. Maekawa, Journal of Physics a-Mathematical and General **33** (2000).

[100] Z. Petrović, Contemporary Materials **1** (2010).

[101] A. Adamson, and A. Gast, *Physical Chemistry of Surfaces* (John Wiley & Sons, 1997).

[102] F. Aurenhammer, Computing Surveys **23** (1991).

[103] P. Richard, J. P. Troadec, L. Oger, and A. Gervois, Physical Review E **63** (2001).

[104] R. E. Williams, Science **161** (1968).

[105] A. Okabe, B. Boots, K. Sugihara, and S. N. Chiu, *Spatial Tesselations: Concepts and Applications of Voronoi Diagrams* (John Wiley & Sons Ltd, West Sussex, 2000), 2 edn.

[106] H. Weber, and D. Marx, Europhysics Letters **27** (1994).

[107] A. J. Krejci, C. G. W. Thomas, J. Mandal, I. Gonzalo-Juan, W. He, R. L. Stillwell, J.-H. Park, D. Prasai, V. Volkov, K. I. Bolotin, and J. H. Dickerson, The Journal of Physical Chemistry B (2012).

[108] A. Libal, C. Reichhardt, and C. O. Reichhardt, Physical Review E **75** (2007).

[109] R. B. S. Oakeshott, and S. F. Edwards, Physica A **189** (1992).

[110] S. Kumar, and S. K. Kurtz, Materials Characterization **31** (1993).

[111] S. Torquato, T. M. Truskett, and P. G. Debenedetti, Physical Review Letters **84** (2000).

[112] T. M. Truskett, S. Torquato, and P. G. Debenedetti, Physical Review E **62** (2000).

[113] A. R. Kansal, S. Torquato, and F. H. Stillinger, Physical Review E **66** (2002).

[114] A. R. Kansal, T. M. Truskett, and S. Torquato, Journal of Chemical Physics **113** (2000).

[115] B. I. Halperin, and D. R. Nelson, Physical Review Letters **41** (1978).

[116] P. J. Steinhardt, D. R. Nelson, and M. Ronchetti, Physical Review B **28** (1983).

[117] K. J. Bishop, C. E. Wilmer, S. Soh, and B. A. Grzybowski, Small **5** (2009).

[118] S. Fraden, A. J. Hurd, and R. B. Meyer, Physical Review Letters **63** (1989).

[119] S. O. Lumsdon, E. W. Kaler, and O. D. Velev, Langmuir **20** (2004).

[120] W. Ristenpart, I. Aksay, and D. Saville, Physical Review Letters **90** (2003).

[121] M. Hosokawa, K. Nogi, M. Naito, and T. Yokoyama, *Nanoparticle technology handbook* (Elsevier, 2007).

[122] J. Moser, and A. Bachtold, Applied Physics Letters **95** (2009).

[123] J. Zahardis, B. W. LaFranchi, and G. A. Petrucci, Atmospheric Environment **40** (2006).

[124] H. Hlaing, X. Lu, T. Hofmann, K. G. Yager, C. T. Black, and B. M. Ocko, ACS Nano **5** (2011).

[125] U. Hartmann, Annual Review of Materials Science **29** (1999).

[126] A. Tonomura, T. Matsuda, J. Endo, T. Arii, and K. Mihama, Physical Review Letters **44** (1980).

[127] R. E. Dunin-Borkowski, M. R. McCartney, R. B. Frankel, D. A. Bazylinski, M. Pósfai, and P. R. Buseck, Science **282** (1998).